Muon Energy Calibration of the MINOS Detectors

Paul Shinichi Miyagawa
Somerville College, Oxford

Thesis submitted in partial fulfilment of the requirements for the degree of Doctor of Philosophy at the University of Oxford

Trinity Term, 2004

Muon Energy Calibration of the MINOS Detectors

Paul Shinichi Miyagawa
Somerville College, Oxford

Thesis submitted in partial fulfilment of the requirements for the degree of
Doctor of Philosophy at the University of Oxford

Trinity Term, 2004

Abstract

MINOS is a long-baseline neutrino oscillation experiment designed to search for conclusive evidence of neutrino oscillations and to measure the oscillation parameters precisely. MINOS comprises two iron tracking calorimeters located at Fermilab and Soudan. The Calibration Detector at CERN is a third MINOS detector used as part of the detector response calibration programme. A correct energy calibration between these detectors is crucial for the accurate measurement of oscillation parameters.

This thesis presents a calibration developed to produce a uniform response within a detector using cosmic muons. Reconstruction of tracks in cosmic ray data is discussed. This data is utilized to calculate calibration constants for each readout channel of the Calibration Detector. These constants have an average statistical error of 1.8%. The consistency of the constants is demonstrated both within a single run and between runs separated by a few days.

Results are presented from applying the calibration to test beam particles measured by the Calibration Detector. The responses are calibrated to within 1.8% systematic error.

The potential impact of the calibration on the measurement of oscillation parameters by MINOS is also investigated. Applying the calibration reduces the errors in the measured parameters by $\sim$10%, which is equivalent to increasing the amount of data by 20%.

To my parents and my grandparents
whom I told I would someday be a doctor . . .
albeit an M.D.

I was created long ago in a far away place where there was always light and no one slept. At first, all seemed in chaos. Slowly, patterns began to emerge. Soon there was structure where once there had been no form. Bit by bit, I was not alone, and there were other minds. There was sentience all about, and before me lay a universe to be discovered. I drank heartily on its offerings, hoping to learn all. But the more I learned, the more there was to learn. There was no end to it. Time passed and I realized that I would have to be content with just learning what I could.

Now I ride the arrow-time with my past dimming behind me and my future shrouded in fog. Day by day, I pass from place to place like a chameleon, living with the life around me, being a part of it all, ever drinking in the wonders of the universe.

Bruce Jolliffe

This is the tail end of a pile of junk.

Peter Skensved

Acknowledgements

An epic journey such as this can never be completed without the assistance of many others. Chief among these is my supervisor Dr. Alfons Weber. He could not have envisioned suffering a first student so exasperatingly high maintenance, yet his faith in me has never wavered as he has prodded, cajoled, coaxed and berated me on my way to submission (of my thesis). For that I can do aught but offer my most profuse thanks.

Two others were particularly crucial for improving the quality of my thesis out of all proportion. Dr. John Cobb was kind enough to look at the early chapters. His approach and comments taught me how meticulous the work needed to be. The quality of the later chapters was improved immensely as I attempted to anticipate the comments John would splash across the page. Sadly he was away at the time I felt the other chapters were finally worthy of the treatment, but into the breach stepped Dr. Giles Barr. He approached the later chapters from the point of view of an examiner. The perspective and comments as an outsider helped to tighten the focus of those chapters.

The rest of the Oxford MINOS group has been another source of great support. Drs. Antonella De Santo, Nathaniel Tagg, Katarzyna Grzelak and Professor Wade Allison have always been ready with perspicacious comments whenever I have given a presentation in the group meetings. Also, just listening to the banter in these meetings was a valuable learning experience.

There are, of course, many others who have been a boon to my research and thus deserving of my gratitude. Dr. Peter Litchfield first got me started on my work on cosmics and has always been a wellspring of encouragement. Dr. Patrick Achenbach kindly supplied the basis of the ray-tracing simulation. The other members of the MINOS UK group have been tremendously supportive. I would be remiss were I not to mention Professor Hay-Boon Mak and Dr. Hans Kraus, who were my supervisors during my pre-MINOS days and from whom I learned a great deal about research.

I am grateful to many others who have provided essential support. The MINOS software core group has always been helpful with my efforts to adapt to the ever-evolving offline software. In particular, in the early days Drs. Nick West, Robert Hatcher, George Irwin, and Mark Messier were targetted for quotidian quixotic queries, and latterly Dr. Brett Viren also got the treatment, but they all invariably responded with rapidity and equanimity. Pete Grönbech, Chris Hunter, Dr. Ian McArthur, John Harris, and Russell Allcock have guaranteed the smooth provision of computing facilities. Beverly Roger, Norma MacManaway, Sue Geddes, Johanna McNulty and Julia Caldecott have ensured that there have been no administrative reasons to terminate prematurely my time in Oxford.

I would also like to express my gratitude for financial support given by the Natural Sciences and Engineering Research Council (NSERC) of Canada, the Department of Particle

Physics at Oxford, the Rutherford-Appleton Laboratory, Somerville College, and the good ol' bank of Mom and Dad.

Innumerable people deserve plaudits for saving me from a mental meltdown. Robert Keeling was my partner in crime and fellow basement exile during my cryodetector days. Since moving upstairs into civilization, I've had the honour and pleasure of sharing an office with Matthew Barker, from room 665 (the last chance saloon next to *that* place) to the tin can at CERN to the palatial penthouse suite back in Oxford. Andrew Aus, Simon Robbins, Anatael Cabrera, Jeff Hartnell, Phillip Litchfield and Tobias Raufer have also had the grave misfortune to inhabit the same office as me, but they have borne my cantankerous neuroses with good grace. Paul Coe and Ankush Mitra have always been available with advice and good cheer. Alas, there is not enough room to list all of the people whom I have met through various societies and who have enriched my life.

Finally, I wish to recognize the immense contribution made by my family. Their unconditional love and confidence in me has sustained me through some trying times.

Table of Contents

List of Figures

List of Tables

— CHAPTER ONE —

Introduction

4 Dez. 1930

Liebe Radioaktive Damen und Herren,

Wie der Überbringer dieser Zeilen, den ich huldvollst anzuhören bitte, Ihnen des näheren auseinandersetzen wird, bin ich angesichts der "falschen" Statistik der N- und Li-6 Kerne, sowie des kontinuierlichen β-Spektrums auf einen verzweifelten Ausweg verfallen, um den "Wechselsatz" der Statistik und den Energiesatz zu retten. Nämlich die Möglichkeit, es könnten elektrisch neutrale Teilchen, die ich Neutronen nennen will, in den Kernen existieren, welche den Spin 1/2 haben und das Ausschließungsprinzip befolgen und sich von Lichtquanten außerdem noch dadurch unterscheiden, daß sie nicht mit Lichtgeschwindigkeit laufen. Die Masse der Neutronen müßte von derselben Größenordnung wie die Elektronenmasse sein und jedenfalls nicht grösser als 0,01 Protonenmasse. — Das kontinuierliche β-Spektrum wäre dann verständlich unter der Annahme, daß beim β-Zerfall mit dem Elektron jeweils noch ein Neutron und Elektron konstant ist. . . .

Ich gebe zu, daß mein Ausweg vielleicht von vornherein wenig wahrscheinlich erscheinen wird, weil man die Neutronen, wenn sie existieren, wohl schon längst gesehen hätte. Aber nur wer wagt, gewinnt, und der Ernst der Situation beim kontinuierlichen β-Spektrum wird durch einen Ausspruch meines verehrten Vorgängers in Amte, Herrn Debye, beleuchtet, der mir kürzlich in Brüssel gesagt hat: "Oh, daran soll man am besten gar nicht denken, sowie an die neuen Steuern." Darum soll man jeden Weg zur Rettung ernstlich diskutieren. — Also, liebe Radioaktive, prüfet, und richtet. — Leider kann ich nicht vom 6. und 7. Dez. in Zürich stattfinden Balles hier unabkömmlich bin. — Mit vielen Grüßen an Euch, sowie an Herrn Back, Euer untertänigster Diener

ges. W. Pauli

Excerpt from Wolfgang Pauli's letter, addressed to the participants of the Tübingen conference on radioactivity, about his neutrino hypothesis in β-decay. See Appendix A for an English translation.

With those words, the neutrino, as it was later dubbed by Enrico Fermi, came into humanity's consciousness. Pauli expressed his incredulity that the neutrino had not yet been discovered. Little did he know that the "little neutral one" would prove to be most elusive and that another 26 years would elapse before it would be convincingly detected [1]. Only now, 70+ years later, are we finally starting to unravel fully the mysteries of this particle and its properties.

Neutrinos, and neutrino oscillations in particular, are one of the current hot topics in particle physics. The absence of oscillations from the Standard Model of particle physics [2] is the one major shortcoming of an otherwise remarkably successful model which has survived much scrutiny, both experimental and theoretical, over the past thirty years. Although neutrino oscillations were first postulated in 1957 [3], only in the past few years has sufficient

tangible evidence accrued to convince the majority of the particle physics community of their existence. But although the focus is shifting from discovery to precision measurement, there are some who still seek the holy grail of the oscillatory dip.

The Main Injector Neutrino Oscillation Search (MINOS) [4] is an experiment capable of fulfilling both of these objectives. Its beam energy spectrum and baseline are tuned to investigate the region of oscillation parameter space suggested by results from Super-Kamiokande [5]. The measurement is made using the Near Detector at Fermilab near Chicago and the Far Detector at the Soudan mine in Northern Minnesota. A third detector, the Calibration Detector located at CERN, forms part of the detector calibration programme. A correct energy calibration between these detectors is crucial for a successful measurement.

This thesis presents a strip-to-strip calibration method developed to produce a uniform response over a detector. The method is used to calibrate the Calibration Detector, and the results from test beam particles are presented. The impact on the parameter measurement by MINOS is also investigated.

Chapter 2 sets the scene by introducing the theory of neutrino oscillations. It then summarizes the results of searches for oscillations. Chapter 3 describes the MINOS experiment and its three components, the neutrino beam and the Near and Far Detectors. It then details the oscillation analysis and outlines the detector calibration programme. Chapter 4 describes the Calibration Detector and its special systems for particle identification. The chapter then summarizes the data-taking at CERN.

Chapter 5 outlines the reconstruction software used in MINOS. It then details the track reconstruction algorithm developed for cosmic muons in the Calibration Detector. Chapter 6 focusses on a relative strip-to-strip calibration developed for the MINOS detectors which uses cosmic muons to define a uniform response within each detector. The chapter details the cosmic muon selection, the applied corrections, and the consistency checks. It also presents the results from using the calibration on a sample of test beam particles. Chapter 7 investigates the potential impact of the strip-to-strip calibration on the measurement of oscillation parameters by MINOS.

Finally, Chapter 8 summarizes the important findings of this thesis and discusses some of the issues of applying the calibration to the Near and Far Detectors.

— CHAPTER TWO —

Neutrino Physics

2.1 Neutrinos in the Standard Model

According to the Standard Model of particle physics [2], neutrinos are electrically neutral leptons. Three generations of neutrinos exist in weak isospin doublets with their charged counterparts. Neutrinos have zero mass, spin $\frac{1}{2}$ and left-handed helicity.

As noted in Chapter 1, the neutrino was first postulated by Wolfgang Pauli in 1930 as a remedy for the apparent lack of energy conservation in beta-decay. However, the existence of neutrinos was conclusively established only after 26 years by Reines and Cowan [1]. It was later determined that they had observed electron-neutrinos, for the muon-neutrino was discovered at Brookhaven in 1962 [6] and shown to be distinct from the electron-neutrino. With the discovery of the tau particle in 1976 [7], a third generation of neutrino was postulated, and the tau-neutrino was finally detected in 2001 by the DONUT experiment [8]. Studies of the Z-boson decay width at LEP [9] indicate that these three flavours are the only active light neutrinos.

The helicity of neutrinos was established experimentally by Goldhaber in 1958 [10].

Experimental limits on neutrino mass are obtained from direct kinematic searches [11–13]:

$$\begin{array}{ll} m_{\nu_e} < 2.2 \text{ eV} & (95\% \text{ C.L., from } {}^3\text{H} \rightarrow {}^3\text{He} + e^- + \overline{\nu}_e) \,, \\ m_{\nu_\mu} < 170 \text{ keV} & (90\% \text{ C.L., from } \pi^+ \rightarrow \mu^+ + \nu_\mu) \,, \\ m_{\nu_\tau} < 15.5 \text{ MeV} & (95\% \text{ C.L., from } \tau \rightarrow 5\pi + \nu_\tau) \,. \end{array} \tag{2.1}$$

2.2 Extensions Beyond the Standard Model

Although the Standard Model assumes that neutrinos have zero mass and experimental mass searches have placed small limits, there is no fundamental reason why neutrinos should be massless. Indeed, standard gauge theory expects particles to have zero mass only if they are associated with an exact gauge symmetry. As this is not true for the lepton quantum number, neutrinos should not be expected to be massless. In fact, it is straightforward to add a neutrino mass term to the Standard Model (e.g., [14]).

Although the experimental limits on the neutrino mass are quoted for the three flavours, the flavour eigenstates are not necessarily coincident with the mass eigenstates. A neutrino produced by a weak interaction as a flavour eigenstate can be expressed as a mixture of the

mass eigenstates:

$$|\nu_\alpha\rangle = \sum_i U^*_{\alpha i}|\nu_i\rangle \qquad (\alpha = e,\, \mu,\, \tau)\,, \tag{2.2}$$

where i runs over all possible mass eigenstates and U is a unitary lepton mixing matrix. Then, as the neutrino propagates through space, each mass component evolves according to Schrödinger's equation:

$$|\nu_\alpha(t>0)\rangle = \sum_i e^{-iE_i t}U^*_{\alpha i}|\nu_i\rangle = \sum_\beta \sum_i U_{\beta i}e^{-iE_i t}U^*_{\alpha i}|\nu_i\rangle\,. \tag{2.3}$$

Differences in energy can cause the components to become out of phase such that the probability of finding the neutrino in flavour eigenstate β at a given time t is thus

$$\mathrm{P}(\nu_\alpha \to \nu_\beta) = |\langle\nu_\beta|\nu_\alpha(t)\rangle|^2 = \left|\sum_i U_{\beta i}e^{-iE_i t}U^*_{\alpha i}\right|^2\,. \tag{2.4}$$

Using the unitarity condition of U, the ultra-relativistic expansion for the neutrino energy $E_i \simeq p + m_i^2/2E$, and the approximation that distance travelled $L \simeq t$, the probability becomes

$$\mathrm{P}(\nu_\alpha \to \nu_\beta) = \sum_i |U_{\beta i}|^2\,|U_{\alpha i}|^2 + 2\,\mathrm{Re}\sum_{j>i} U_{\beta i}U^*_{\beta j}U^*_{\alpha i}U_{\alpha j}\exp\left(-i\frac{\Delta m^2_{ij}L}{2E}\right)\,, \tag{2.5}$$

where $\Delta m^2_{ij} = m^2_i - m^2_j$. This form shows that, to have oscillatory flavour mixing, at least one neutrino must have a nondegenerate finite mass.

The mixing matrix, also known as the Maki-Nakagawa-Sakata (MNS) matrix[1], can be represented in a form analogous to the Cabibbo-Kobayashi-Maskawa (CKM) matrix of the quark mixing sector [15], which for Dirac neutrinos is

$$U_{MNS} = \begin{pmatrix} c_{12}c_{13} & s_{12}c_{13} & s_{13}e^{-i\delta} \\ -s_{12}c_{23} - c_{12}s_{23}s_{13}e^{i\delta} & c_{12}c_{23} - s_{12}s_{23}s_{13}e^{i\delta} & s_{23}c_{13} \\ s_{12}s_{23} - c_{12}c_{23}s_{13}e^{i\delta} & -c_{12}s_{23} - s_{12}c_{23}s_{13}e^{i\delta} & c_{23}c_{13} \end{pmatrix}\,, \tag{2.6}$$

where $c_{ij} = \cos\theta_{ij}$ and $s_{ij} = \sin\theta_{ij}$ ($i,\, j = 1,\, 2,\, 3$). The three mixing angles θ_{12}, θ_{13} and θ_{23} represent rotations between the flavour and mass bases, and δ represents a complex CP-violating phase. For Majorana neutrinos there are two additional phases. However, these phases cannot be observed in neutrino oscillations.

The MNS matrix can be factored into the product of three matrices [16]:

$$U_{MNS} = \begin{pmatrix} 1 & & \\ & c_{23} & s_{23} \\ & -s_{23} & c_{23} \end{pmatrix}\begin{pmatrix} c_{13} & & s_{13}e^{i\delta} \\ & 1 & \\ -s_{13}e^{i\delta} & & c_{13} \end{pmatrix}\begin{pmatrix} c_{12} & s_{12} & \\ -s_{12} & c_{12} & \\ & & 1 \end{pmatrix}\,. \tag{2.7}$$

As we shall see in Section 2.3.4, the first matrix can be associated with the atmospheric neutrino sector, and the third with the solar.

When only two neutrino flavours are considered, the MNS matrix simplifies to the two-dimensional form, represented by a rotation of a single mixing angle θ, analogous to the

[1] This matrix is sometimes referred to as the Pontecarvo-MNS matrix

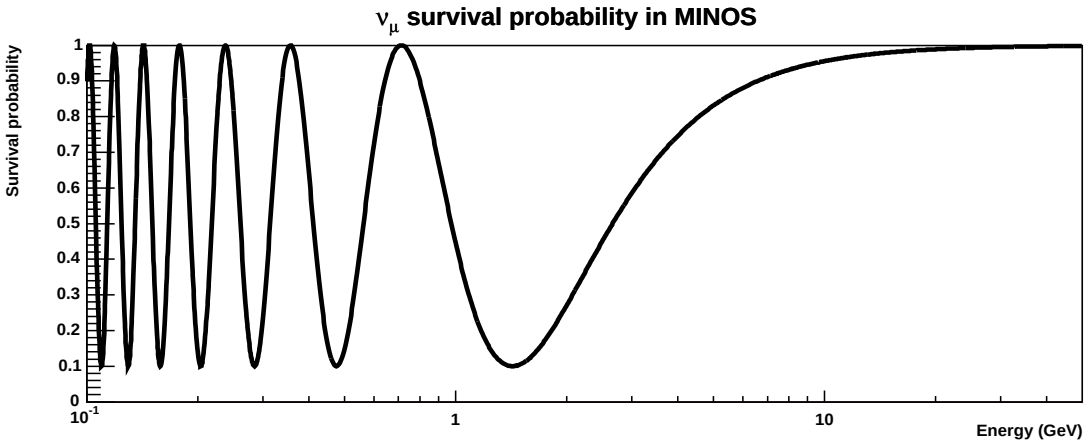

Figure 2.1: Survival probability of muon-neutrinos as a function of neutrino energy under experimental conditions similar to those seen in the MINOS experiment. Two-flavour oscillations are assumed with L set to the MINOS baseline of 735 km and the oscillation parameters ($\sin^2 2\theta = 0.9,\ \Delta m^2 = 2.4 \times 10^{-3}$ eV^2) set similar to the best fit parameters of the most recent Super-Kamiokande data [5]. The less-than-maximal mixing results in the survival probability not reaching zero.

Cabibbo angle for quark mixing:

$$U = \begin{pmatrix} \cos\theta & \sin\theta \\ -\sin\theta & \cos\theta \end{pmatrix} . \tag{2.8}$$

From this the two-flavour mixing probability can be derived:

$$\mathrm{P}(\nu_\alpha \to \nu_\beta) = \sin^2 2\theta \sin^2 \left(\frac{1.27 \Delta m^2 L}{E} \right) \qquad (\alpha \neq \beta) , \tag{2.9}$$

where Δm^2 is expressed in eV^2, the detector-to-source distance L in metres (km) and the neutrino energy E in MeV (GeV). In this form we can see that the mixing probability follows an oscillation with the amplitude limited by the factor $\sin^2 2\theta$, which describes the degree of mixing between the two flavours, and the period determined by $\Delta m^2 L/E$. The ratio E/L is determined by the experimental conditions, and it can be selected to maximize the probability of seeing the oscillatory dip. Figure 2.1 shows the survival probability as a function of neutrino energy with the parameters set similar to those seen in the Super-Kamiokande experiment [5] and to which the MINOS experiment will be sensitive. MINOS will attempt to observe the highest-energy dip seen near 1.5 GeV to provide conclusive evidence for neutrino oscillations.

When neutrinos propagate through matter, they can interact with the protons, neutrons and electrons of the medium, which is represented in Equation 2.3 as an addition of a potential V to the energy term, i.e., $E_i \to E_i + V$. These potentials modify the simple formulas derived earlier for the oscillation probabilities. All neutrino flavours can have neutral-current interactions with the medium. However, electron-neutrinos can also have charged-current interactions with electrons, leading to an additional term in the potential for the electron-neutrinos. This can change small vacuum mixing of ν_e into large mixing in matter. This consequence of the asymmetry between flavours is called the MSW effect [17].

Reaction	ν energy (MeV)
$p + p \rightarrow {}^2\mathrm{H} + e^+ + \nu_e$	≤ 0.420
$p + e^- + p \rightarrow {}^2\mathrm{H} + \nu_e$	1.442
${}^7\mathrm{Be} + e^- \rightarrow {}^7\mathrm{Li} + \nu_e$	(90%) 0.861
	(10%) 0.383
${}^8\mathrm{B} \rightarrow {}^8\mathrm{Be}^* + e^+ + \nu_e$	< 15
${}^3\mathrm{He} + p \rightarrow {}^4\mathrm{He} + e^+ + \nu_e$	≤ 18.77
${}^{13}\mathrm{N} \rightarrow {}^{13}\mathrm{C} + e^+ + \nu_e$	≤ 1.20
${}^{15}\mathrm{O} \rightarrow {}^{15}\mathrm{N} + e^+ + \nu_e$	≤ 1.73
${}^{17}\mathrm{F} \rightarrow {}^{17}\mathrm{O} + e^+ + \nu_e$	≤ 1.74

Table 2.1: Reactions in the Sun that produce neutrinos and the energies of the resulting neutrinos [21].

2.3 Experimental Evidence for Oscillations

Many experiments have reported results which could be interpreted as arising from neutrino oscillations. Historically, the first hint for oscillations came in 1968 from the Homestake chlorine experiment [18], which reported an apparent deficit of solar neutrinos. The first compelling evidence for oscillations came from the atmospheric neutrino data analysis of the Super-Kamiokande experiment [19]. The LSND accelerator experiment [20] has also claimed to have observed oscillations; however, its result has yet to be confirmed by any other experiment and is viewed with skepticism by the rest of the neutrino community. Neutrino oscillations are now accepted as the explanation for the anomalous results of both solar and atmospheric neutrino experiments.

2.3.1 Solar Neutrinos

2.3.1.1 Solar Models

The Sun produces energy in its interior through many chains of thermonuclear reactions, the overall result of which is the burning of hydrogen nuclei into helium, accompanied by the emission of electron-neutrinos:

$$4p + 2e^- \rightarrow {}^4\mathrm{He} + 2\nu_e + 26.73\ \mathrm{MeV}\ . \tag{2.10}$$

These chains are incorporated in solar models which follow the evolution of the Sun until it matches present solar parameters such as radius, mass, luminosity and He/H ratio. The most successful of these models, referred to as Standard Solar Models (SSMs), are subsequently used to make predictions about other observable quantities such as neutrino fluxes from the solar core and solar acoustic modes [21].

In solar neutrino circles, the most-quoted model is the Bahcall–Pinsonneault SSM [22], hereafter referred to as BP2000. Its predictions are believed to be accurate for several reasons, among which are that it satisfies the luminosity constraint, and that it agrees to high precision with the latest helioseismological data [23].

Solar neutrinos are produced by several reactions which are listed in Table 2.1 along with the energies of the resulting neutrinos. Figure 2.2 shows the BP2000 flux predictions for the reactions that produce observable fluxes.

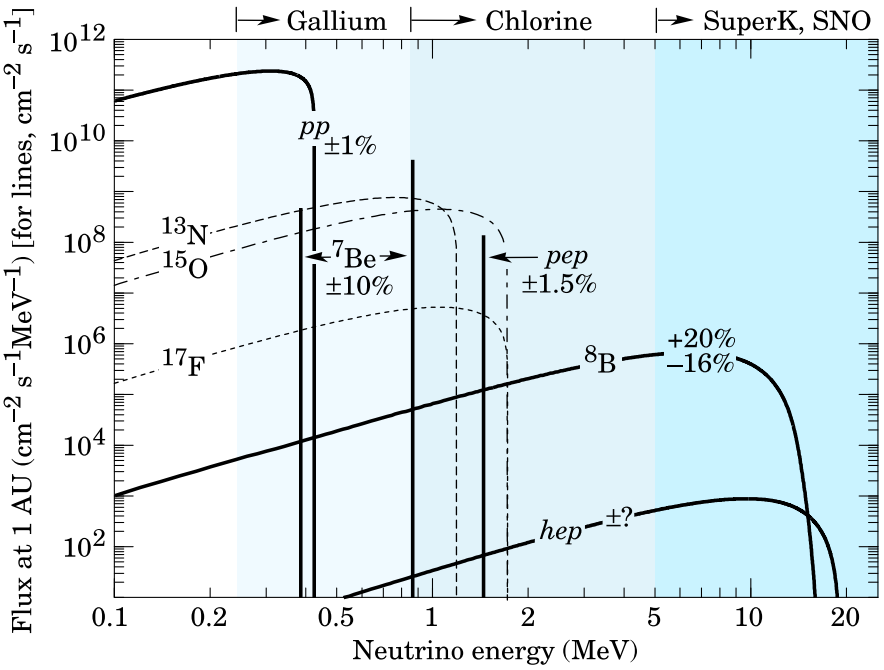

Figure 2.2: Energy spectra of solar neutrinos (figure from [9]). The fluxes are at a distance of one astronomical unit (1 AU $= 1.496 \times 10^{11}$ m) from the Sun. The fluxes for the pep and ^{7}Be neutrinos are in units of cm^{-2}s^{-1}. The rest are in units of cm^{-2}s^{-1}MeV^{-1}.

2.3.1.2 The Solar Neutrino Problem

Seven experiments have measured and continue to measure the solar neutrino flux. These can be divided into two categories according to detection technique: radiochemical experiments (Homestake, SAGE, GALLEX and GNO) and water-Čerenkov experiments (Kamiokande, Super-Kamiokande and SNO). SNO will be discussed in greater detail in Section 2.3.1.3.

In radiochemical experiments the neutrinos are captured on target nuclei to create radioisotopes. The detector is then periodically flushed and the radioisotopes counted to measure the integrated neutrino flux. This technique is sensitive exclusively to electron-neutrinos.

The Homestake chlorine experiment [18, 24] measured the solar neutrino flux via the reaction:

$$\nu_e + {}^{37}\mathrm{Cl} \rightarrow e^- + {}^{37}\mathrm{Ar}\,, \tag{2.11}$$

which has a threshold of 814 keV. The ^{37}Cl was in the form of 615 tonnes of tetrachlorethylene (C_2Cl_4).

The three gallium experiments, SAGE [25], GALLEX [26] and GNO [27], detect neutrinos via the reaction:

$$\nu_e + {}^{71}\mathrm{Ga} \rightarrow e^- + {}^{71}\mathrm{Ge}\,, \tag{2.12}$$

which has a threshold of 233.2 keV. SAGE uses 57 tonnes of metallic gallium, while GALLEX and its successor GNO use 100 tonnes of gallium chloride solution.

In the water-Čerenkov experiments the neutrino is elastically scattered off electrons; the scattered electron produces a Čerenkov ring that is detected:

$$\nu_x + e^- \rightarrow \nu_x + e^- \qquad (x = e, \mu, \tau)\,. \tag{2.13}$$

This allows real-time measurement of individual events, allowing studies of differential dis-

Experiment	Measured	BP2000	Measured/BP2000
Homestake	2.56 ± 0.23	$7.6\,^{+1.3}_{-1.1}$	0.34 ± 0.06
GALLEX + GNO	$74.1\,^{+6.7}_{-7.8}$	$128\,^{+9}_{-7}$	0.58 ± 0.07
SAGE	$74.1\,^{+7.8}_{-7.4}$	$128\,^{+9}_{-7}$	0.59 ± 0.07
Kamiokande	$2.80 \times (1.00 \pm 0.14)$	$5.05 \times (1.00^{+0.20}_{-0.16})$	0.55 ± 0.13
Super-Kamiokande	$2.40 \times (1.00^{+0.04}_{-0.03})$	$5.05 \times (1.00^{+0.20}_{-0.16})$	0.48 ± 0.09

Table 2.2: Results from solar neutrino experiments [24, 30–33]. This table, taken from [22], also lists the predicted event rates according to the BP2000 solar model. The different experiments have different threshold energies, leading to the different event rate predictions. The results for Homestake, GALLEX/GNO and SAGE are in Solar Neutrino Units (1 SNU $= 10^{-36}$ events atoms^{-1}s^{-1}). The results for Kamiokande and Super-Kamiokande are in 10^6 cm^{-2}s^{-1}.

tributions (e.g., energy spectrum, angular distribution). This technique has some sensitivity to all neutrino flavours through the neutral-current interaction, but its primary sensitivity is to electron-neutrinos via the charged-current interaction.

Kamiokande [28] used 4.5 ktonne of pure water. Its successor Super-Kamiokande [29] uses 50 ktonne of pure water. Both experiments have set a threshold of 5 MeV for the solar neutrino analysis.

Table 2.2 summarizes the results reported from these experiments [24, 30–33]. It also lists the predicted event rates from BP2000 for comparison. All experiments have observed a flux substantially less than predicted. This discrepancy between prediction and observation came to be known as the *solar neutrino problem*.

While many authors have proposed solutions to the solar neutrino problem (for a recent review, see [34]), the one that is now almost universally accepted is that the electron-neutrinos from the Sun are undergoing flavour oscillations en route to the Earth. Since the previous experiments have either zero (chlorine and gallium) or limited (water-Čerenkov) sensitivity to these other (muon or tau) neutrino flavours, oscillations could account for the discrepancy in neutrino fluxes. An experiment that is able to measure separately the flux of electron-neutrinos and the total flux of all neutrino flavours can test the hypothesis of solar neutrino oscillations. The Sudbury Neutrino Observatory (SNO) [35] has measured these two fluxes.

2.3.1.3 Results from SNO

SNO [35] is a heavy-water Čerenkov detector located at the 6800-foot level of Inco's Creighton mine near Sudbury, Ontario, Canada. The detector consists of 1 ktonne of ultra-pure D_2O housed within a spherical acrylic vessel 12 m in diameter shielded by 7.3 ktonne of ultra-pure H_2O in a barrel-shaped cavity 30 m high and 22 m diameter at the waist. Light produced in the water is detected by 9456 photomultiplier tubes (PMTs) mounted on a geodesic support structure suspended in the light water 2.5 m away from the acrylic vessel.

In common with Kamiokande and Super-Kamiokande, SNO can detect solar neutrinos using the elastic scattering (ES) reaction 2.13. However, the true power of SNO derives from the deuterium in the heavy water, with which the neutrino can interact by either the charged-current (CC) reaction:

$$\nu_e + d \rightarrow p + p + e^- \qquad (\text{threshold} = 1.44\ \text{MeV}) \tag{2.14}$$

or the neutral-current (NC) reaction:

$$\nu_x + d \rightarrow \nu_x + p + n \qquad (\text{threshold} = 2.2\ \text{MeV})\ . \tag{2.15}$$

At solar neutrino energies the CC reaction is sensitive solely to electron-neutrinos, providing a measure of the ν_e flux as well as the spectral shape of the flux. The NC reaction is equally sensitive to all flavours and thus measures the total flux of solar neutrinos irrespective of neutrino oscillations. Thus the CC/NC ratio is a powerful test of the oscillation hypothesis.

The neutron from the NC reaction is detected using different techniques during three phases of running. In the first phase, when pure heavy water was used, the neutrons were captured on the deuterium to produce 6.25-MeV photons. In the recently-completed second phase, when 2.5 tonnes of NaCl were added to the heavy water, the neutrons were captured with increased efficiency on Cl to produce 8.6-MeV photons. In the third and final phase, the salt will be removed and ^{3}He proportional counters installed to allow direct detection of the neutrons.

Analysis of data from the pure heavy-water phase [36], using a threshold of 5 MeV, gives the following fluxes (in units of 10^6 cm^{-2}s^{-1}):

$$\begin{aligned}
\phi_{\rm CC}^{\rm SNO} &= 1.76\,^{+0.06}_{-0.05}\,(\text{stat})\,^{+0.09}_{-0.09}\,(\text{syst})\ , \\
\phi_{\rm ES}^{\rm SNO} &= 2.39\,^{+0.24}_{-0.23}\,(\text{stat})\,^{+0.12}_{-0.12}\,(\text{syst})\ , \\
\phi_{\rm NC}^{\rm SNO} &= 5.09\,^{+0.44}_{-0.43}\,(\text{stat})\,^{+0.46}_{-0.43}\,(\text{syst})\ .
\end{aligned} \tag{2.16}$$

$\phi_{\rm NC}^{\rm SNO}$, which represents the total solar neutrino flux, is consistent with the predicted BP2000 value. A straightforward change of variables resolves the data into the electron (ϕ_e) and non-electron ($\phi_{\mu\tau}$) components:

$$\begin{aligned}
\phi_e &= 1.76\,^{+0.05}_{-0.05}\,(\text{stat})\,^{+0.09}_{-0.09}\,(\text{syst})\ , \\
\phi_{\mu\tau} &= 3.41\,^{+0.45}_{-0.45}\,(\text{stat})\,^{+0.48}_{-0.45}\,(\text{syst})\ .
\end{aligned} \tag{2.17}$$

Therefore the non-electron flux is 5.3σ above zero, providing compelling evidence that electron-neutrinos have transformed into other flavours in a manner consistent with neutrino oscillations.

Figure 2.3 is an especially elegant representation of the data. It shows the flux of non-electron neutrinos versus the flux of electron-neutrinos for each of the three reactions. The solid bands represent the 1σ flux combinations for each reaction, and the diagonal dashed lines indicate the BP2000 prediction of the total neutrino flux $\phi_{\rm SSM}$. It is evident that the total measured flux $\phi_{\rm NC}^{\rm SNO}$ is consistent with $\phi_{\rm SSM}$, and that the combined fluxes from the three reactions converge at the fit values for ϕ_e and $\phi_{\mu\tau}$.

Results from the salted phase [37] yield fluxes which agree with those from the first phase:

$$\begin{aligned}
\phi_{\rm CC}^{\rm SNO} &= 1.59\,^{+0.08}_{-0.07}\,(\text{stat})\,^{+0.06}_{-0.08}\,(\text{syst})\ , \\
\phi_{\rm ES}^{\rm SNO} &= 2.21\,^{+0.31}_{-0.26}\,(\text{stat}) \pm 0.10\,(\text{syst})\ , \\
\phi_{\rm NC}^{\rm SNO} &= 5.21 \pm 0.27\,(\text{stat}) \pm 0.38\,(\text{syst})\ .
\end{aligned} \tag{2.18}$$

A global oscillation analysis of all solar neutrino data (e.g., [38]) yields a best fit $\Delta m^2 \sim 5 \times 10^{-5}$ eV^2, although another solution at $\Delta m^2 \sim 10^{-7}$ eV^2 is not excluded. The next step

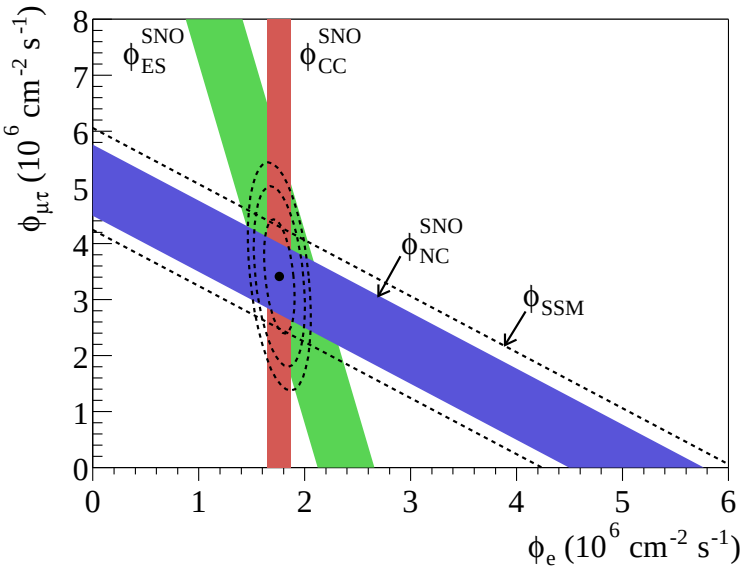

Figure 2.3: Results from the pure heavy-water phase of SNO (figure from [36]). The red band represents the 1σ flux combinations from the CC reaction, which is purely ν_e and therefore vertical. The blue represents NC, which is the total neutrino flux and therefore has a slope of -1. The green represents ES, which has limited sensitivity to ν_μ and ν_τ and is therefore much closer to vertical than the NC band. The dashed ellipses represent the 68%, 95% and 99% errors on the best fit values of ϕ_e and $\phi_{\mu\tau}$. The diagonal dashed lines indicate the predicted total neutrino flux from BP2000 [22].

is to distinguish between the two solutions and better determine the oscillation parameters. The most promising experiment for this purpose is the KamLAND experiment [39].

2.3.1.4 Results from KamLAND

KamLAND [39] is a reactor neutrino experiment located in the Kamioka mine near Tsukuba, Gifu, Japan, that looks for reactor $\overline{\nu}_e$ disappearance. Sixteen nuclear reactors in Japan deliver a well-understood flux of $\overline{\nu}_e$ to the KamLAND detector. The antineutrinos have an average energy of 4 MeV and travel an average distance of 180 km. This allows KamLAND to probe the $\Delta m^2 \sim 5 \times 10^{-5}$ eV^2 solution for solar neutrino oscillations using an artificial source of neutrinos that is independent of the solar model.

KamLAND detects $\overline{\nu}_e$ by inverse beta-decay:

$$\overline{\nu}_e + p \rightarrow e^+ + n \; . \tag{2.19}$$

The target consists of 1000 tonnes of liquid scintillator which is contained within a transparent 13-m diameter balloon and is shielded by 2.5 m of mineral oil. The scintillation light is detected by 2000 PMTs mounted on an 18-m diameter stainless-steel sphere.

The latest results from KamLAND [40] report a ratio of the number of observed events to the number of expected events without oscillations as $0.582 \pm 0.069\,(\text{stat}) \pm 0.039\,(\text{syst})$ for $\overline{\nu}_e$ energies > 3.4 MeV. This is inconsistent with the no-disappearance hypothesis. The deficit of events can also be seen clearly in the measured energy spectrum shown in Figure 2.4. Moreover, the shape of the measured spectrum is distorted in a manner consistent with neutrino oscillations. Therefore, the KamLAND results give strong evidence that neu-

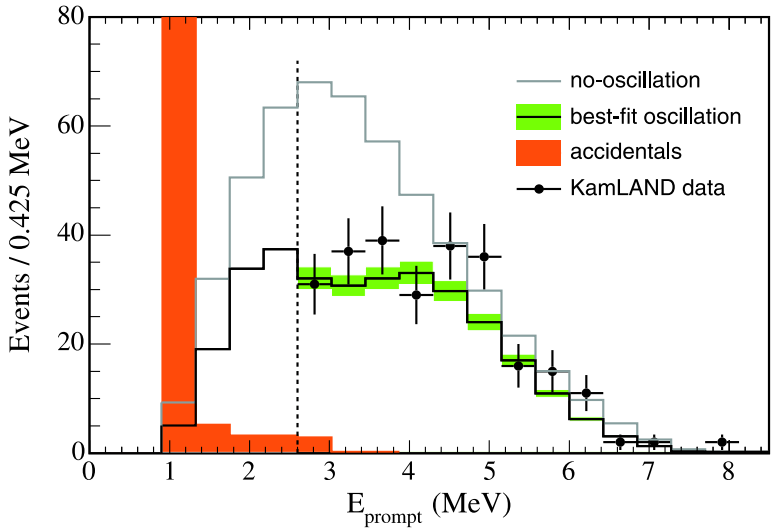

Figure 2.4: Prompt energy spectrum of reactor neutrinos observed in KamLAND (figure from [40]). The plot shows the prompt e^+ energy spectrum observed at KamLAND as solid circles with error bars, along with a histogram in grey of the expected no-oscillation spectrum and a histogram in black of the best-fit oscillation spectrum. The shaded green band indicates the systematic error in the best-fit spectrum. The vertical dashed line marks the 2.6-MeV threshold used in the analysis to exclude background contributions (shaded orange) from geo-neutrinos and other "accidental" sources.

trino oscillations are occurring in the solar sector at $\Delta m^2 = 8.3 \times 10^{-5}$ eV^2, $\tan^2\theta = 0.41$.

2.3.1.5 Summary of Solar Results

The latest reviews perform a combined analysis of solar and KamLAND data (e.g., [41]). They indicate that solar neutrinos are undergoing MSW oscillations while emerging from the Sun and vacuum oscillations while propagating to the Earth. Figure 2.5 shows the allowed regions in the oscillation parameter space. The best fit point is:

$$\tan^2\theta_{\text{vacuum}} = 0.40\,, \qquad \Delta m^2 = 8.2 \times 10^{-5}\ \text{eV}^2\,. \tag{2.20}$$

2.3.2 Atmospheric Neutrinos

2.3.2.1 Atmospheric Neutrino Flux and Oscillations

Atmospheric neutrinos are produced from the hadronic showers created by cosmic rays impinging on the Earth's atmosphere. The cosmic rays, mainly protons ($\sim$80%) and α-particles ($\sim$15%), interact with nuclei in the atmosphere to produce a cascade of particles including pions and kaons. These pions and kaons then decay to produce muons, electrons and neutrinos:

$$\begin{aligned} p + N &\rightarrow \text{n}\pi^{\pm} + X\,, \\ \pi^{\pm} &\rightarrow \mu^{\pm} + \nu_{\mu}(\overline{\nu}_{\mu})\,, \\ \mu^{\pm} &\rightarrow e^{\pm} + \nu_e(\overline{\nu}_e) + \overline{\nu}_{\mu}(\nu_{\mu})\,, \end{aligned} \tag{2.21}$$

and similarly for kaons. If the secondaries are of sufficiently low energy ($\lesssim$ 2 GeV) that they decay before reaching the Earth, the ratio R of muon-like neutrinos to electron-like neutrinos

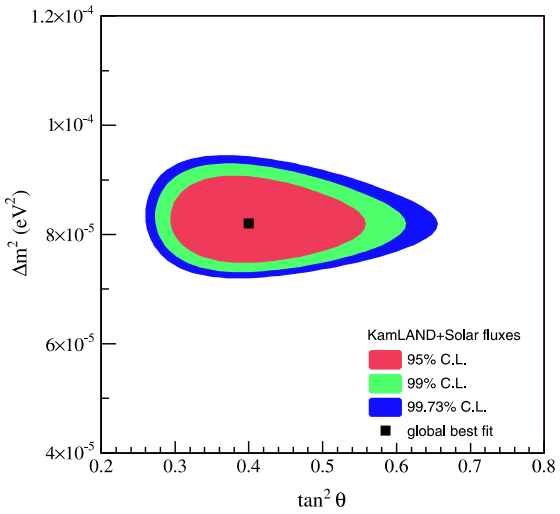

Figure 2.5: Allowed regions for solar neutrino oscillation parameters including KamLAND data (figure from [40]). The contours shown are 95%, 99% and 99.73% (3σ) confidence limits. The square marks the best-fit point of $\tan^2\theta = 0.40$, $\Delta m^2 = 8.2 \times 10^{-5}$ eV^2.

is expected to be

$$R = \frac{N_{\nu_\mu} + N_{\overline{\nu}_\mu}}{N_{\nu_e} + N_{\overline{\nu}_e}} \sim 2\,, \tag{2.22}$$

where N_{ν_μ} (N_{ν_e}) and $N_{\overline{\nu}_\mu}$ ($N_{\overline{\nu}_e}$) are the number of muon (electron) neutrinos and antineutrinos respectively. While the absolute fluxes are known only to ∼20–30%, the uncertainties largely cancel such that the ratio itself is known to ∼5% (see [42] for a recent review of atmospheric neutrino flux calculations). Furthermore, experiments conventionally report results as a ratio of ratios:

$$R' \equiv \frac{R_{\mathrm{DATA}}}{R_{\mathrm{MC}}}\,, \tag{2.23}$$

where R_{DATA} is the ratio of muon-like events over electron-like events measured by the experiment and R_{MC} is the same ratio obtained from a Monte Carlo simulation. Assuming that the neutrinos do not change flavour en route to the detector, R' is expected to be 1. Any deviation from unity could be an indication of some flavour-changing process, including neutrino oscillations.

A more sensitive test for neutrino oscillations studies the zenith angle distribution of the incident atmospheric neutrino. The baseline can span three orders of magnitude from 10–20 km, for downward-going neutrinos produced directly above the detector, up to 12 000 km, for upward-going neutrinos produced on the opposite side of the Earth. This gives ample scope to observe a modulation in the flux due to neutrino oscillations.

From considerations of geometry alone and assuming a homogeneous cosmic ray flux, the neutrino flux per unit area is identical at any location on Earth. Comparing the flux of downward-going neutrinos at zenith angle Θ to the flux of upward-going neutrinos at zenith angle $\pi - \Theta$, symmetry considerations dictate that the two quantities must be the same (see Figure 2.6). Therefore any deviation from up-down symmetry could be interpreted as being caused by neutrino oscillations.

In reality, the geomagnetic field can alter significantly the trajectories of low-energy cosmic rays and thereby induce a non-isotropy in the neutrino flux even in the absence of neutrino oscillations. In particular, cosmic rays of intermediate energy (10–20 GeV) exhibit a

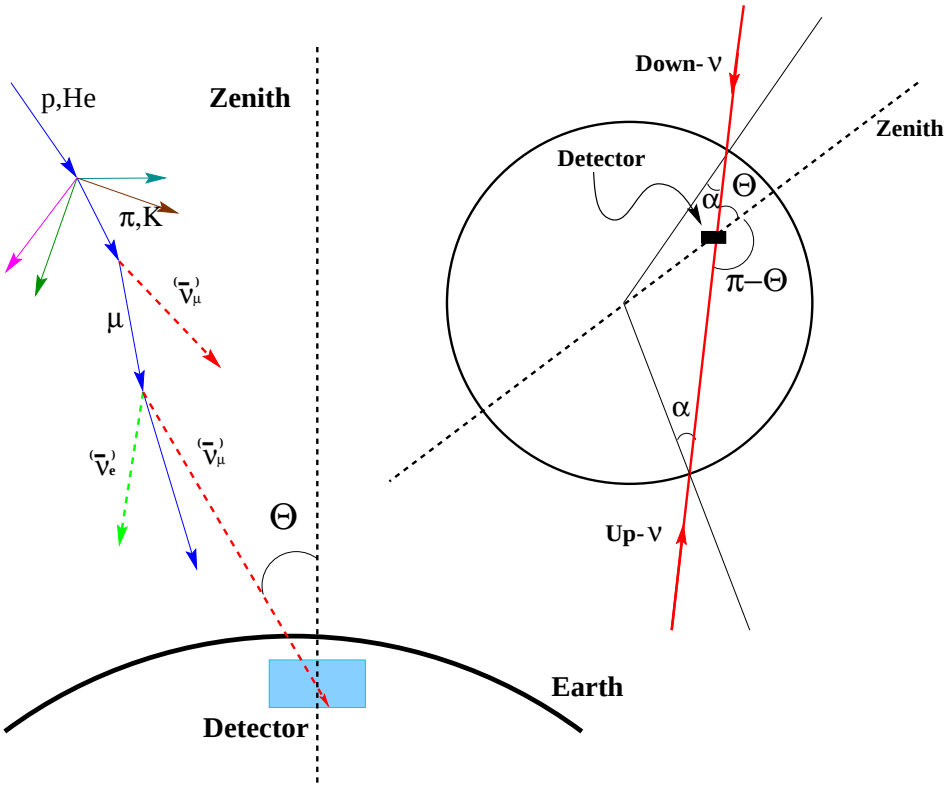

Figure 2.6: Sketch of the geometry of atmospheric neutrino detection (figure from [43]).

strong east-west asymmetry. However, as long as the geomagnetic effects are well understood they can be accounted for in calculations.

2.3.2.2 The Atmospheric Neutrino Anomaly

The first measurements of the atmospheric neutrino flux were made by proton-decay experiments, for which atmospheric neutrinos constituted a source of background. IMB [44, 45], a 3.3-ktonne water-Čerenkov detector, first reported in 1986 an R' value of $0.54 \pm 0.05\,(\text{stat}) \pm 0.07\,(\text{syst})$. This result was confirmed two years later by Kamiokande [46, 47], which obtained $R' = 0.60 \pm 0.06$. However, NUSEX [48] and Fréjus [49–51], both fine-grained iron calorimeters massing 150 and 900 tonnes, measured R' values of $0.96\,^{+0.32}_{-0.28}$ and $0.99 \pm 0.13\,(\text{stat}) \pm 0.08\,(\text{syst})$ respectively, which apparently conflicted with the results from the water-Čerenkov experiments. This discrepancy was thought for some time to be due to systematic differences between the two experimental methods. This belief persisted until Soudan-2 [52, 53], a 963-tonne fine-grained iron calorimeter, reported $R' = 0.68 \pm 0.11\,(\text{stat}) \pm 0.06\,(\text{syst})$ in agreement with the IMB and Kamiokande results. The original discrepancy is now believed to be due to fluctuations in the NUSEX and Fréjus data. The measurements from these five experiments plus those from Super-Kamiokande [54] are summarized in Figure 2.7. This deviation in R' from unity has come to be known as the *atmospheric neutrino anomaly*.

A number of experiments (IMB [45], Kamiokande [47], Baksan [56], MACRO [57] and Soudan-2 [53]) have investigated, with varying degrees of success, neutrino oscillations as the solution to the atmospheric neutrino anomaly by measuring the zenith angle distribution.

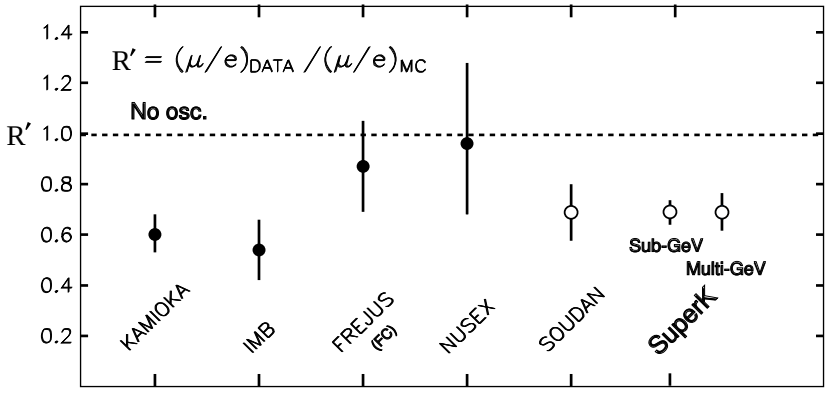

Figure 2.7: Measurements of the atmospheric neutrino flavour ratio of ratios (figure from [55]). The Fréjus number of 0.87 ± 0.18 is taken from the analysis of fully contained events in an earlier paper [49] (the number in the main text is from an analysis of all events in the later paper [51]). The other results are as given in the main text and are taken from [45, 46, 48, 52, 54].

By far, the most sensitive measurements have come from Super-Kamiokande [19], which during the summer of 1998 announced the most compelling evidence to date for neutrino oscillations in the atmospheric neutrino sector.

2.3.2.3 Results from Super-Kamiokande

As mentioned in Section 2.3.1.2, Super-Kamiokande [29] is a water-Čerenkov detector situated 1000 m underground in the Kamioka mine near Tsukuba, Gifu, Japan. The detector consists of a cylindrical stainless-steel tank 42 m high and 39 m diameter containing 50 ktonnes of pure water. An inner detector of 32 ktonnes is demarcated by an optical barrier 2.5 m inside the tank wall on all sides, and the inner surface is lined with 11 146 PMTs to detect light produced in the inner detector. The outer surface of the optical barrier is covered with 1885 outward-looking PMTs.

The latest results based on 1489 live days of data [58] give $R' = 0.649 \pm 0.016 \pm 0.051$ for the sub-GeV sample and $0.675\,^{+0.032}_{-0.030} \pm 0.083$ for the multi-GeV sample[2]. These values are consistent with the results discussed in Section 2.3.2.2 and differ from unity by about 7σ.

The zenith angle distributions for 1289 live days of data were also studied [54]. Figure 2.8 shows the distribution of the cosine of the zenith angle for electron-like and muon-like events. The electron-like events are in good agreement with predictions for the no-oscillation scenario. However, the muon-like events are depleted markedly from the no-oscillation prediction, but correspond well with an oscillation-induced modulation. Moreover, the degree of depletion decreases as $\cos\theta$ increases, i.e., as the baseline decreases, and in the multi-GeV sample there is very little depletion for downward-going neutrinos. Recalling the oscillatory term in Equation 2.9, the zenith angle contributions would be consistent with $\nu_\mu \rightarrow \nu_\tau$ oscillations with Δm^2 matched to low-energy (sub-GeV) neutrinos, while high-energy (multi-GeV) neutrinos require longer baselines for the oscillation effects to become noticeable.

An attempt was also made to observe the oscillation effects by studying the dependence of the flux with L/E similarly to Figure 2.1. Figure 2.9(a) shows the ratio of observed to expected events for the muon-like sample as a function of L/E for 1489 live days of data [5]. The muon-like events exhibit a dependence on L/E which is compatible with the oscillation

[2] In actuality, the sub-GeV and multi-GeV samples correspond to events with energies below and above 1.33 GeV respectively

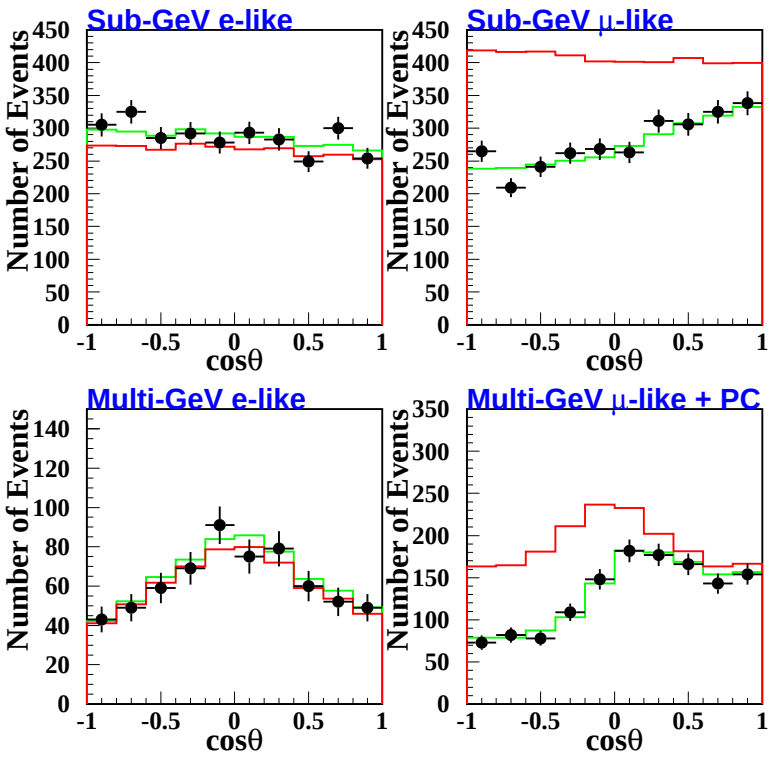

Figure 2.8: Zenith angle distributions obtained by Super-Kamiokande from 1289 live days data (figure from [59]). The red line is the distribution expected for no oscillations. The green line is the distribution expected for $\nu_\mu \to \nu_\tau$ oscillations with maximal mixing and $\Delta m^2 = 2.5 \times 10^{-3}$ eV^2.

hypothesis (black solid line), and a dip is visible in the distribution. Moreover, this dip is not compatible with the alternative solutions of neutrino decay (blue dashed line) or neutrino decoherence (red dotted line). However, the oscillatory pattern is washed out somewhat by the angular and energy resolution, resulting in the dip not reaching zero and the subsequent rise not reaching unity. Moreover, the large errors near the dip reflect the low statistics due to a geometrical effect[3] so the shape of the dip is not well-defined in the region of interest. This points out that the evidence for oscillations, while compelling, is not completely convincing.

In the absence of a complementary excess of electron-like events, Super-Kamiokande has interpreted the deficit of muon-like events as the consequence of $\nu_\mu \to \nu_\tau$ oscillations in a two-flavour mixing scheme and has extracted an allowed region for the oscillation parameters. The latest results based on the L/E analysis of 1489 days of data [5] are shown in Figure 2.9(b). The best fit point is

$$\sin^2 2\theta = 1.00\,, \qquad \Delta m^2 = 2.4 \times 10^{-3}\ \text{eV}^2\,. \tag{2.24}$$

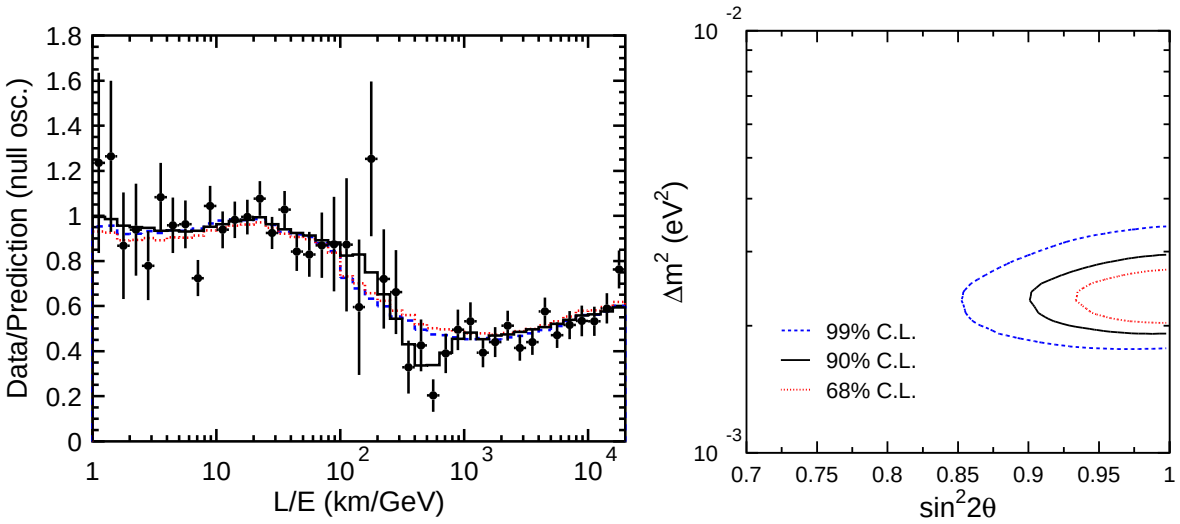

(a) Dependence of neutrino flux with L/E. The black solid line shows the distribution expected for the best-fit parameters. The blue dashed line and the red dotted line show the best-fit expectations for neutrino decay and neutrino decoherence respectively. These solutions have χ^2_{min} which are 3.4σ and 3.8σ larger than that for neutrino oscillations.

(b) Allowed regions for atmospheric neutrino oscillation parameters. The contours shown are for 68%, 90% and 99% confidence limits.

Figure 2.9: Results from 1489 live days of Super-Kamiokande data (figures from [5]). The best fit parameters are for $\nu_\mu \to \nu_\tau$ oscillations with maximal mixing and $\Delta m^2 = 2.4 \times 10^{-3}$ eV^2.

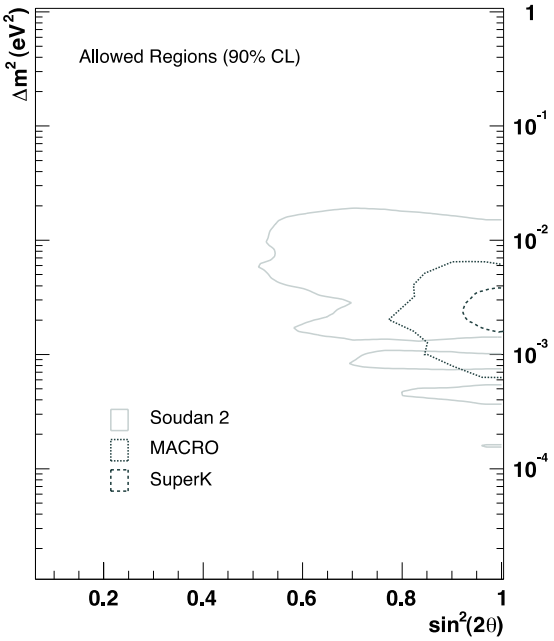

Figure 2.10: Allowed regions for atmospheric neutrino oscillation parameters from Super-Kamiokande (1289 days) [60], Soudan 2 [53] and MACRO [57] (figure from [53]).

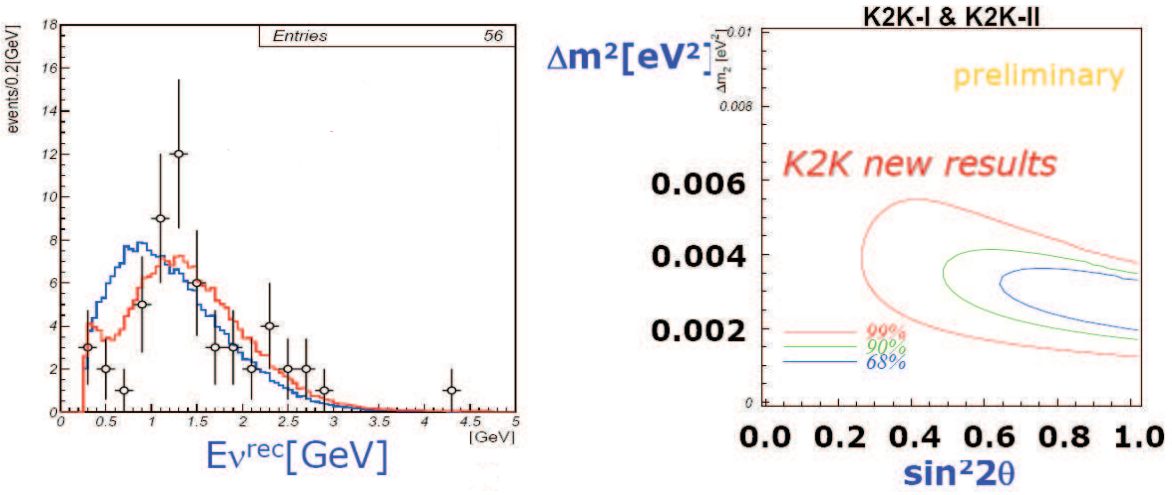

(a) Distortion of E_ν spectrum. The black open circles are the data points. The blue line is the distribution expected for no oscillations. The red line is the distribution expected for the best-fit parameters.

(b) Allowed regions for neutrino oscillation parameters. The contours shown are for 68%, 90% and 99% confidence limits.

Figure 2.11: Results from K2K with 8.9×10^{19} protons on target (figures from [61]). The best fit parameters are for $\nu_\mu \to \nu_\tau$ oscillations with maximal mixing and $\Delta m^2 = 2.73 \times 10^{-3}$ eV^2.

2.3.2.4 Summary of Atmospheric Results

Several experiments have measured an anomalous deficit of atmospheric muon neutrinos. Super-Kamiokande has provided a tantalizing hint that these neutrinos are oscillating to tau-neutrinos with near-to-maximal mixing and $\Delta m^2 \sim 2.4 \times 10^{-3}$ eV^2. The allowed region is confirmed, albeit with lower precision, by Soudan-2 [53] and MACRO [57] using different target materials (see Figure 2.10). However, Super-Kamiokande has not succeeded in observing a fully resolved oscillatory dip that would constitute a conclusive proof of oscillations. Moreover, the uncertainties in atmospheric neutrino flux predictions limit the precision to which atmospheric neutrino experiments can measure the oscillation parameters. Therefore, the next step is to use artifically produced neutrinos (e.g., by an accelerator beam) in a systematic investigation of the atmospheric neutrino anomaly.

The K2K (KEK to Kamioka) experiment is the first long-baseline experiment to have made a measurement of the oscillation parameters [61]. A ν_μ beam (average energy 1.3 GeV) is created at the KEK Accelerator Laboratory in Tsukuba, Japan, and directed the beam towards Super-Kamiokande, giving a baseline of 250 km. To date K2K has observed 108 neutrino events, a deficit on the expected value of $150.9\,^{+11.6}_{-10.0}$. Moreover, it has observed a distortion in the neutrino energy spectrum (see Figure 2.11(a)) which K2K has interpreted as arising from neutrino oscillations. The best fit point for the oscillation parameters

$$\sin^2 2\theta = 1.00\,, \qquad \Delta m^2 = 2.73 \times 10^{-3}\,\text{eV}^2 \tag{2.25}$$

[3] This geometrical effect reflects the facts that the Earth is spherical and the neutrinos originate throughout the Earth's atmosphere. Near the horizon the distance to the atmosphere changes very rapidly, so the solid angle subtended by those values of L is small and therefore the number neutrinos with baseline L will be small as well.

agrees with the values from Super-Kamiokande; however, K2K requires much more statistics before its allowed regions (see Figure 2.11(b)) become comparable to those of Super-Kamiokande.

The MINOS experiment [4], which will be described in Chapter 3, is another long-baseline experiment which has its beam energy spectrum and baseline tuned to study the region of oscillation parameter space suggested by the Super-Kamiokande results.

2.3.3 Short-Baseline Experiments

A number of short-baseline (≤ 1 km) accelerator experiments (CDHSW [62], BNL E776 [63], CHORUS [64], NOMAD [65] and KARMEN 2 [66]) have looked for neutrino oscillations with high Δm^2 (> 0.1 eV^2), but have not observed any such evidence. In contrast, the LSND experiment [20] has reported the appearance of $\overline{\nu}_e$ in a $\overline{\nu}_\mu$ beam and attributed it to $\overline{\nu}_\mu \rightarrow \overline{\nu}_e$ oscillations. However, the results of KARMEN 2 and the Bugey reactor experiment [67] exclude much of the LSND allowed region (see Figure 2.12); moreover, the LSND result cannot be reconciled with the solar and atmospheric results without introducing a fourth, "sterile" (inactive) flavour of neutrino. Accordingly, the neutrino community has chosen to exclude the LSND effect from most neutrino oscillation models until it is confirmed by other experiments. The first definitive test of the LSND effect is expected from the MiniBooNE experiment [68], which is currently taking data and anticipates a first result by 2005.

2.3.4 The Overall Picture

Neutrino oscillations are believed to occur in the solar and atmospheric neutrino sectors. Figure 2.12 summarizes the current situation for measurements of neutrino oscillation parameters. Recalling the factorized form of the U_{MNS} matrix (Equation 2.7) and ignoring the CP-violating phase δ and the LSND effect, it is natural to associate

$$\begin{aligned} \Delta m^2_{\text{solar}} &\equiv \Delta m^2_{21} \ , \\ \Delta m^2_{\text{atm}} &\equiv \Delta m^2_{32} \ , \\ \theta_{\text{solar}} &\equiv \theta_{12} \ , \\ \theta_{\text{atm}} &\equiv \theta_{23} \ , \end{aligned} \tag{2.26}$$

while a limit on θ_{13} is set by the CHOOZ reactor experiment [70], and Δm^2_{31} is constrained by $\Delta m^2_{31} = \Delta m^2_{32} + \Delta m^2_{21}$. The limit on θ_{13} set by a global analysis of solar, atmospheric and reactor data [71] is

$$\tan^2 \theta_{13} < 0.055 \ , \tag{2.27}$$

i.e., θ_{13} is small, and in the limit $\theta_{13} = 0$ the solar and atmospheric neutrino oscillations can be treated as two independent two-flavour mixing scenarios.

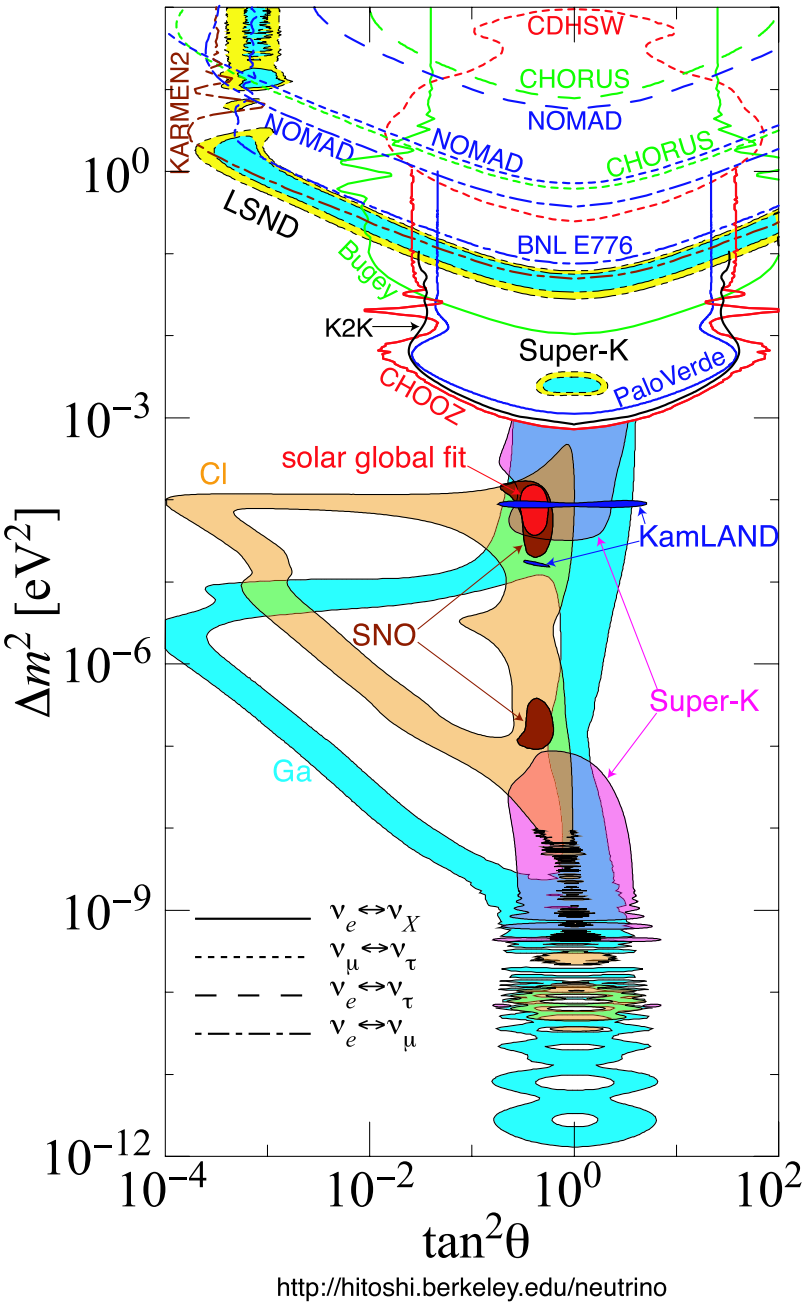

Figure 2.12: Summary of current knowledge of neutrino oscillation parameters (figure from [69], which is an update of a similar figure in [9]). The coloured regions are allowed regions for the oscillation parameters. The solar results (Cl, Ga, Super-K, SNO, KamLAND) are at 95% confidence limit; the atmospheric Super-K and LSND results are at 90% and 99% confidence limit respectively for the turquoise and yellow areas. White regions demarcated by a line are excluded regions and are at 90% confidence limit. The line pattern identifies the oscillation channel.

— CHAPTER THREE —

The MINOS Experiment

The Main Injector Neutrino Oscillation Search (MINOS) [4] is a long-baseline neutrino oscillation experiment. Figure 3.1 shows the layout of the experiment. The beam of primarily μ-neutrinos will be produced at Fermilab near Chicago and directed towards the Soudan mine in Northern Minnesota (see Figure 3.2), giving a baseline of 735 km. The energy spectrum of the beam will be measured at both locations by iron-scintillator tracking calorimeters. The spectrum measured by the Near Detector at Fermilab, which should contain negligible oscillations due to the short baseline from the beam production point, will be used to extrapolate the unoscillated spectrum at Soudan. Comparison with the spectrum measured by the Far Detector at Soudan will serve as a key tool in the MINOS oscillation analysis.

3.1 Neutrino Beam

The neutrino beam [72, 73] is created using 120 GeV protons extracted from the Main Injector accelerator at Fermilab. The spill time is roughly 10 μs every 2 seconds. The protons are directed downwards at 3.3° so as to point towards the Soudan mine, and then they impinge on a graphite production target. The objective is to achieve at least 2.0×10^{20} protons on target per year. Secondary pions and kaons are momentum-selected and focussed using two magnetic horns. The secondaries are then allowed to decay by the form $\pi^+(K^+) \rightarrow \mu^+\nu_\mu$ in an evacuated decay pipe that is 675 m long. Undecayed primaries and secondaries are removed by an aluminum and copper hadron absorber at the end of the decay pipe, and the remaining muons are absorbed by 240 m of dolomite. The layout of these components is

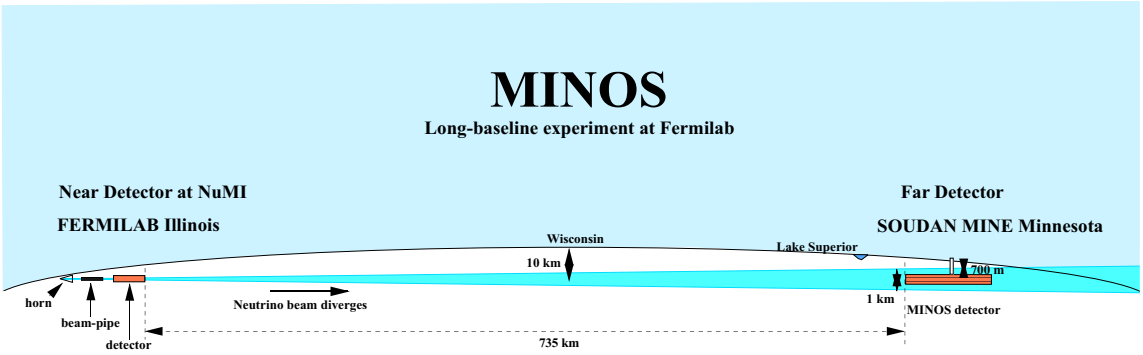

Figure 3.1: Schematic of the MINOS experiment (not to scale).

Figure 3.2: Map of neutrino beam used by MINOS.

shown in Figure 3.3. This produces a beam primarily composed of ν_μ with contamination of 0.8% from ν_e and $\overline{\nu}_e$ [74].

The energy spectrum of the neutrino beam is determined by the positions of the two magnetic horns used to focus the secondaries (see Figure 3.4). Three energy configurations have been considered. Initially MINOS will run with the low energy configuration, which yields neutrinos of average energy $\sim$3 GeV. This was selected to optimize coverage of the oscillation parameter region favoured by Super-Kamiokande. The production target and second horn are mounted on motorized tracks, so it will be relatively easy to reconfigure the beam for higher energies should they be required for, say, studies of systematics.

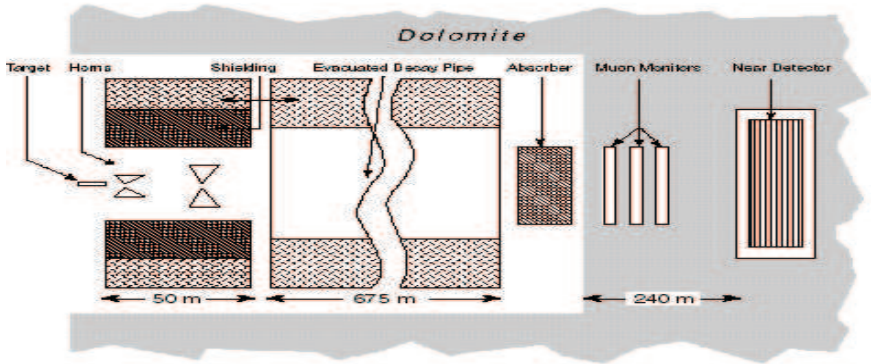

Figure 3.3: Layout of components of neutrino beam (figure from [72]).

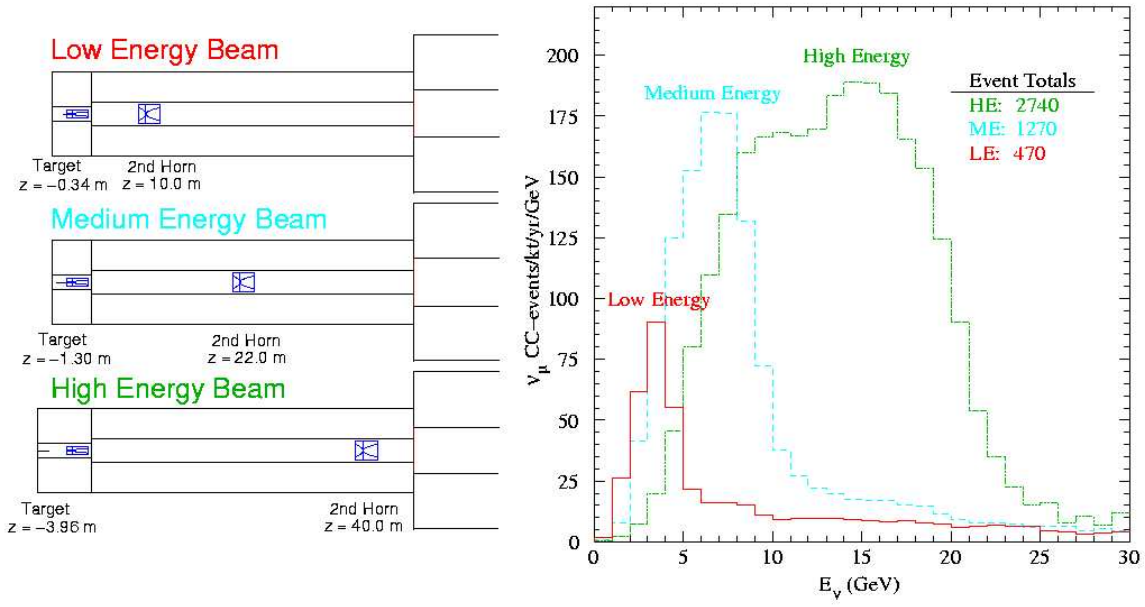

Figure 3.4: Magnetic horn configurations for the three energy configurations and the energy spectra of the beam neutrinos [74]. The spectra assume 4×10^{20} protons on target per year. The first horn is located at $z = 0$ m.

Figure 3.5: Photograph of the Far Detector. The extra planes of scintillator on top act as a veto shield for cosmic muons.

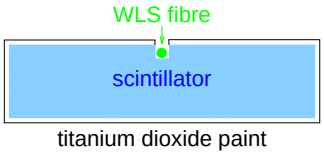

Figure 3.6: Cross-section of scintillator strip.

3.2 Far Detector

The Far Detector (photo in Figure 3.5), located at the 2000-foot level (equivalent to a water overburden of 2000 m) of the Soudan mine, is a 5.4-kilotonne iron-scintillator detector which acts as a combined hadron calorimeter and muon spectrometer. It consists of steel as the target material interleaved with extruded polystyrene scintillator as the active detector. The detector is magnetized by a coil running through the centre of the planes, providing a toroidal field averaging 1.3 T. Extra scintillator modules, described below, are laid on top of the detector to help identify cosmic muons.

The steel is divided into 486 octagonal plates 8 metres in diameter and 1 inch thick. Mounted on the rear of the steel plates are planes of plastic scintillator 1 cm thick. Within each plane the scintillator is divided into 192 strips each 4.1 cm wide and spanning the width of the steel. Consecutive planes of scintillator are oriented at right angles to each other to provide two projections for tracking. The planes of scintillator are also rotated 45° with respect to the horizontal and vertical to allow easier access to the ends of the scintillator modules once the detector is constructed.

Figure 3.6 illustrates a cross-section of a scintillator strip. The strips are co-extruded with a thin coating of TiO_2 to provide a reflective layer to contain the scintillation light. Each strip has a groove along the central axis of one of its 4.1-cm wide faces. The groove is 2 mm deep and 1.3 mm wide. Glued into this groove is a 1.2-mm diameter Kuraray Y11(175) wavelength-shifting (WLS) fibre [77]. The WLS fibre is needed because the blue scintillation light has an absorption length of about 20 cm in the scintillator. The fibre traps the blue light (average $\lambda = 460$ nm), transforms it to green (average $\lambda = 530$ nm) and transmits it to the sides of the detector. From there clear fibres transport the green light to the readout system. Figure 3.7 shows the attenuation in light yield due to absorption in the WLS fibre. Figure 3.8 shows the emission spectra for scintillator and WLS fibre.

The strips within a single plane are assembled into eight scintillator modules (see photograph in Figure 3.9), each of which contains 20 or 28 strips enclosed in a light-tight aluminum case. The ends of the modules hold plastic manifolds which route the WLS fibres to optical connectors. The two ends of each fibre are routed to opposite manifolds. The connectors then interface with the readout system shown in Figure 3.10.

Clear fibre ribbon cables optically connect the scintillator modules to multiplex (MUX) boxes which each contain three multi-anode photomultiplier tubes (PMTs). The PMTs used in the Far Detector are Hamamatsu M16 tubes, which have 16 pixels each. The PMTs are operated at a mean pixel gain of 0.8×10^6. The MUX box distributes the fibres such that eight fibres couple to each PMT pixel, leading to an eightfold multiplexing[1]. The multiplexing pattern [78] has maximal spacing between strips read out by the same pixel. The pattern also minimizes confusion from cross-talk by mapping adjacent strips to nonadjacent pixels. The order of fibres on one side of the detector is permuted with respect to the other, allowing the

[1] Strictly speaking, this is optical summing rather than multiplexing.

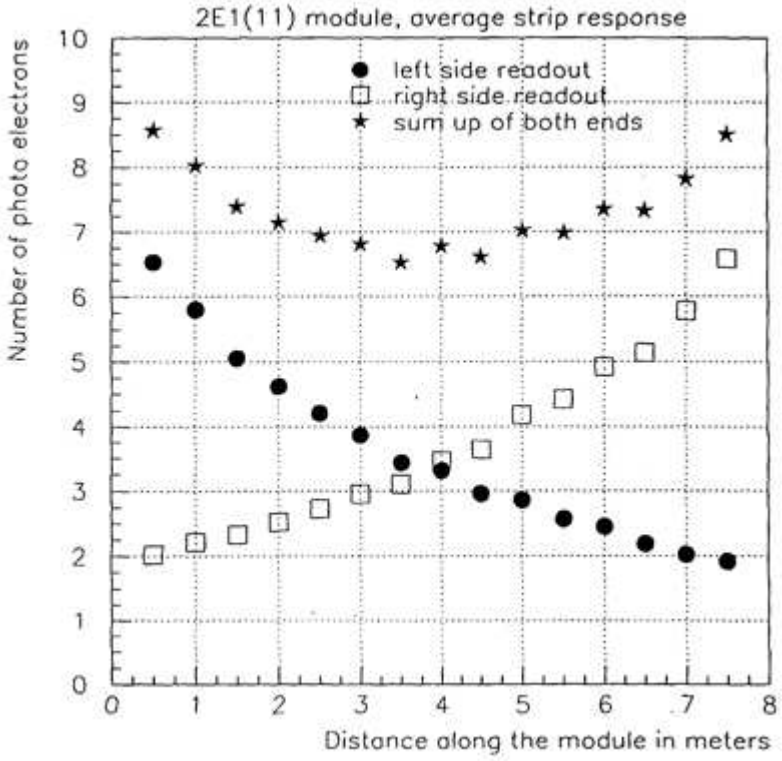

Figure 3.7: Light yields from a prototype scintillator module (figure from [75]). The light detected, measured in photoelectrons, is plotted against the distance from the left-side readout at which a cosmic muon passed through the scintillator strip. The left-side readout (circles) and right-side readout (squares) show attenuation due largely to absorption in the WLS fibre. The sum of the two readouts (stars) gives a roughly constant light yield near the centre of the strip, with a rise towards the ends.

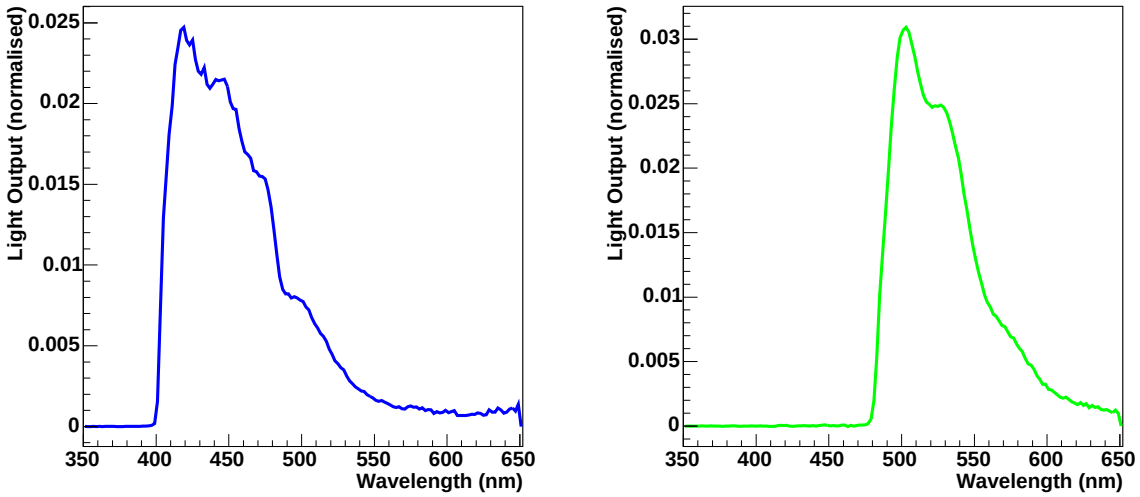

(a) Emission spectrum of scintillator when excited by a UV laser.

(b) Emission spectrum of WLS fibre when illuminated by scintillator.

Figure 3.8: Emission spectra of scintillator and WLS fibre [76].

Figure 3.9: Photograph of a scintillator module before the aluminum case has been sealed. The module is 20 strips wide. In the foreground is the manifold that guides the WLS fibres to the optical connector. The extra lengths of fibre within the manifolds are often referred to as "pigtails". The fibres have not yet been trimmed to the connector. There is another manifold at the other end of the module to enable readout from both ends.

signal to be demultiplexed later.

The layout of the online readout systems for the Far Detector is shown in Figure 3.11. It is divided into three main systems: the front-end readout electronics, shown in mauve; the timing system, shown in yellow; and the data acquisition (DAQ) system, shown in green.

The front-end readout electronics is responsible for digitizing the signals from the PMTs. The readout electronics for the Far Detector [80] is based on the Viking Architecture (VA) chip series from Ideas ASA. The version of the VA chip used in MINOS has 32 channels, each with a charge-sensitive preamplifier, a shaper (shaping time 500 ns) and a sample-and-hold. The 32 channel signals are then fed into a single output multiplexer. Each VA chip is used to read out the 16 anode signals for a single PMT plus signals from the PIN diodes used by the light injection system, which will be described in Section 3.5.1. There is a deadtime of 5 μs while the VA chip is being read out.

The readout architecture (see Figure 3.12) is organized into VA Front-end Boards (VFBs), which are attached to the MUX boxes, and VA Readout Controllers (VARCs), which are located in remote VME crates.

The VFB interfaces directly with the three PMTs inside the MUX box to provide the anode signals plus a readout trigger signal to the VARC. The VFB houses three VA chips and their support circuitry. It also holds an ASD-lite (Amplifier/Shaper/Discriminator) chip which is connected to the last dynodes of the three PMTs. The signal from the ASD-lite is used to trigger the readout of the anodes and to timestamp the event.

The VARC coordinates the readout process of the VA chips and is responsible for signal digitization and trigger time-stamping. It houses up to six pairs of Event Timestamp Controllers (ETCs) and VARC Mezzanine Modules (VMMs). Each ETC/VMM pair services two VFBs. Once it receives a dynode trigger from a VFB, the ETC creates a timestamp (1.6-ns resolution) based on that trigger (meaning that all readouts from a single PMT receive the

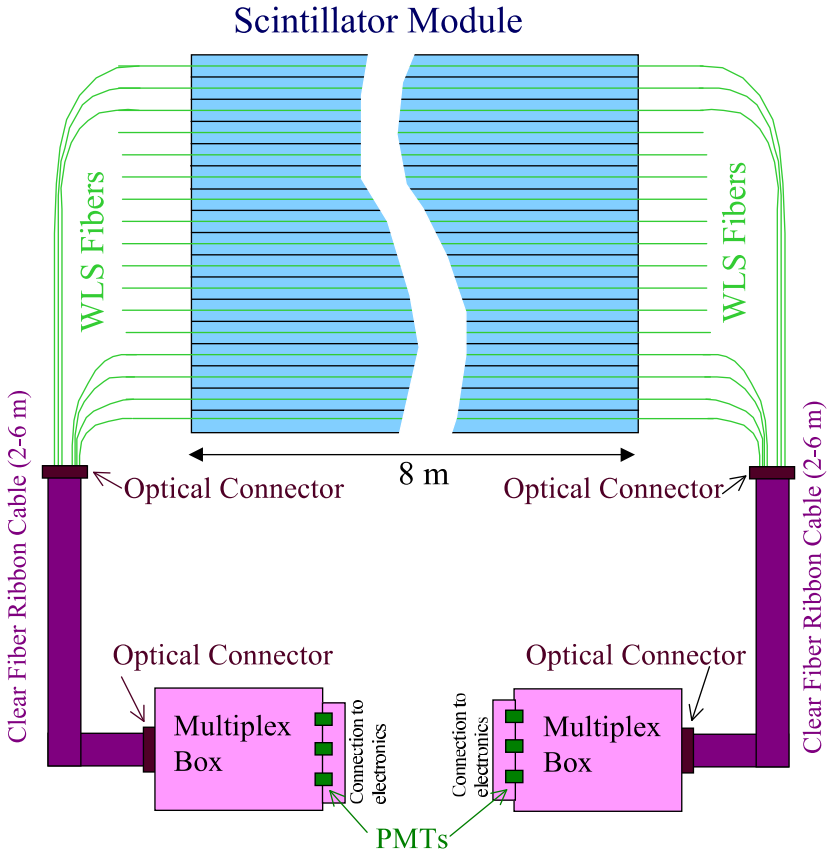

Figure 3.10: Schematic of the scintillator readout system for the Far Detector (figure from [4]). WLS fibres in a scintillator module are routed to optical connectors at both ends of the module. Clear fibre ribbon cables then transport the scintillation light to the MUX box where the light is distributed to the appropriate PMT pixel. Note that each MUX box is connected to several scintillator modules.

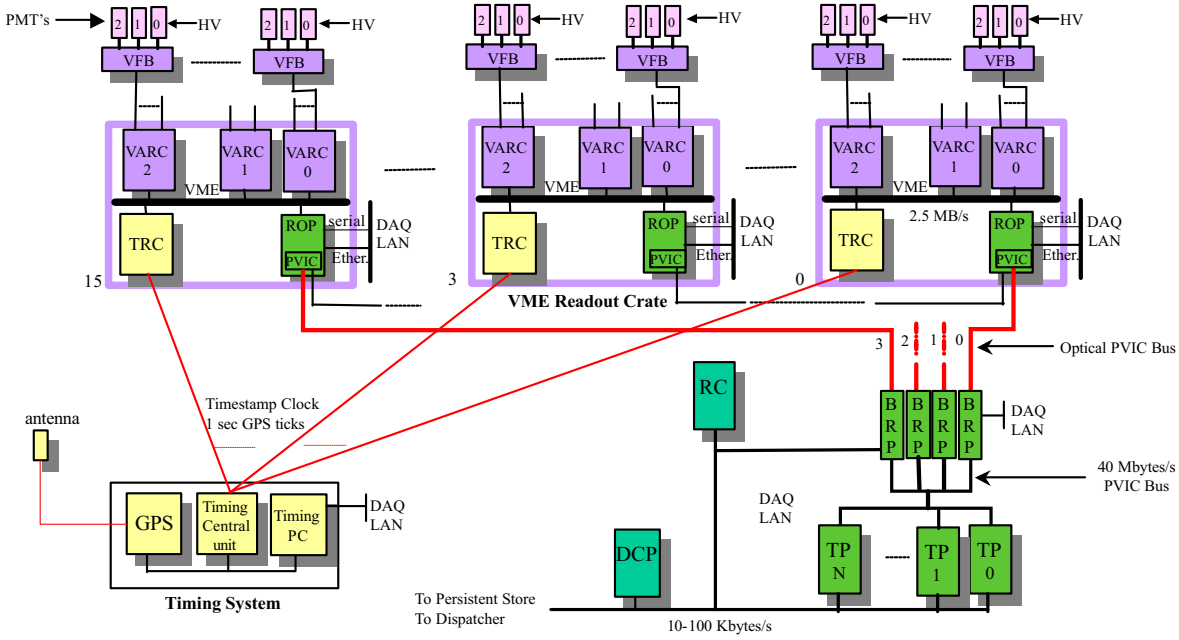

Figure 3.11: MINOS online systems architecture for the Far Detector (figure from [79]). The front-end electronics are shown in mauve, the timing system is shown in yellow, and the data acquisition system is shown in green.

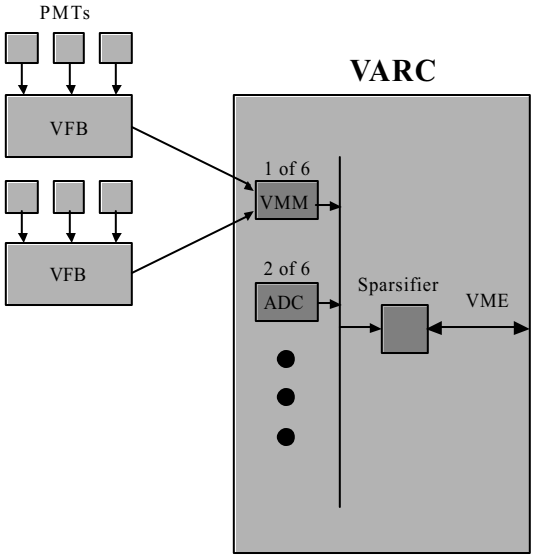

Figure 3.12: Readout architecture for Far Detector front-end electronics (figure from [80]). A VFB holds three VA chips, each of which interfaces with a PMT, to provide the PMT anode signals to the VARC. A VARC holds six VMMs, each of which has an ADC to service two VFBs. The VARC coordinates the readout process of the VA chips, digitizes the anode signals and outputs them to the VME crate.

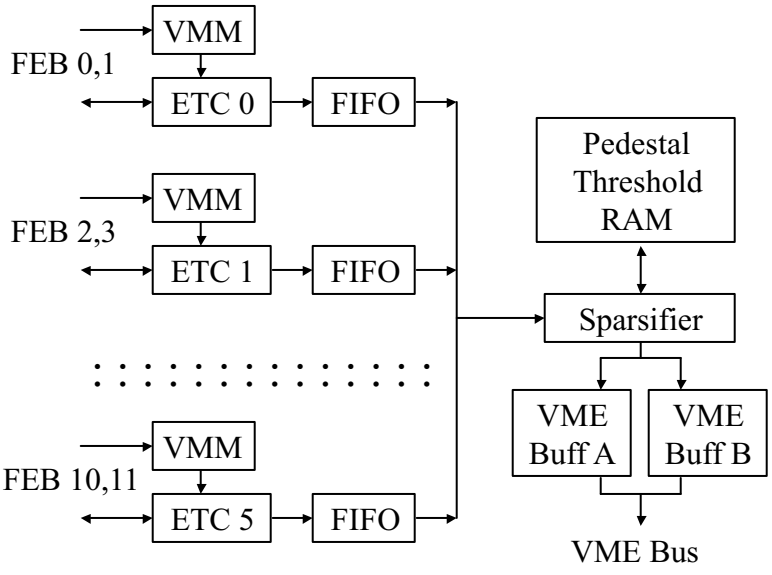

Figure 3.13: VARC data flow diagram (figure from [80]). This diagram shows the flow of data in the VARC. The ETCs receive trigger signals from the front-end boards (FEB, or VFBs in the text). The ETCs then create timestamps and coordinate the readouts of the FEBs. The FEBs send data to the VMMs for digitization, and the VMMs pass the digitized data to the ETCs. The ETCs then bundle the timestamps and digitizations together and buffer them in the FIFOs. The sparsifier then reads data from each FIFO in turn and, after subtracting pedestals if requested, outputs to one of the VME buffers. The buffer being filled changes every 50 ms so that the inactive buffer can be read out by the VME crate.

Rate	Far Detector	Near Detector
beam ν	135 ν_μ CC/kt/10^{20} pot	0.8/spill/10^{20} pot in target region
cosmic μ	1 Hz	270 Hz
noise	6 MHz	0.6 MHz
trigger	5 kHz	1 kHz (cosmic ray mode)

Table 3.1: Expected event rates in the MINOS detectors. All numbers are taken from [82]. The neutrino event rates are for no oscillations. pot = protons on target

same timestamp) and coordinates the readout of the VA chips on that VFB. The VMM digitizes the anode signals from the VA chips using a 14-bit analogue-to-digital converter (ADC) and passes the data to the ETC. The data from the ETC is buffered in a FIFO before it is sparsified and output to one of the two VME buffers. The buffer accumulating data swaps every 50 ms to allow the inactive buffer to be read out by the DAQ system. Figure 3.13 diagrams the data flow in the VARC.

The purpose of the timing system [81] is to enable the absolute time measurement of each digitization in the detector and to synchronize the operation of the readout electronics. This allows the identification of events associated with neutrino beam spills and the measurement of the relative time between digitizations within an event. The Global Positioning System (GPS) antenna and receiver provide a clock signal that is synchronized with Coordinated Universal Time (UTC). The Timing Central Unit (TCU) distributes the clock signal to the Timing Receiver Cards (TRCs) which are situated in the VME crates. The TRC synchronizes the VARCs within that crate. At the same time, the timing computer (TPC) distributes the clock signal to the DAQ system.

The DAQ system controls the operation of the readout electronics, the division of data into events, and data collection. Run Control (RC) allows the detector operator to set the operating mode. The mode is passed to the Read-Out Processor (ROP) in each VME crate. The ROP then controls the VARCs in that crate and passes data down the DAQ chain. The Branch Read-out Processors (BRPs) assemble the data from all of the ROPs into time frames and pass them to the trigger farm. There the Trigger Processors (TPs) divide the data into 160-ns time slices called *snarls*, each of which corresponds to a particle event in the detector, and determine whether the snarls are of sufficient interest for offline analysis. Those events that are deemed worthy are passed to the Data Collection Process (DCP) which formats and writes them out to persistent store.

Table 3.1 summarizes the event rates that are expected in the two detectors.

3.3 Near Detector

The Near Detector, located at Fermilab, is designed to be similar to the Far Detector so as to reduce systematic errors in the Near-Far comparison. It uses the same target and active detector material, the steel is the same thickness, the scintillator is the same granularity, and the magnetic field strength is the same. However, there are some differences in the experimental environment that cannot be eliminated, most notably the higher event rate at the Near Detector, and these have dictated some of the differences in design.

The Near Detector is much smaller than the Far Detector, massing only 980 tonnes. Since the beam spot is small, it can be easily contained by the detector. Therefore, to reduce the

Figure 3.14: Photograph of partially constructed Near Detector. The plane at the front is partially instrumented. Photograph courtesy of K. Grzelak.

amount of wasted material, the planes are squashed octagons of 4.8 m width and 3.8 m height with the magnetic coil offset from the centre (see Figure 3.14).

The Near Detector is divided longitudinally into four functionally distinct sections (see Figure 3.15):

1. **Veto section** (20 planes of steel). Neutrino events in this part are not used because of possible end effects in the detector and possible background from neutrons produced by neutrino interactions in the rock upstream of the detector.

2. **Target section** (40 planes of steel). Neutrino events in this part are used for the near/far comparison.

3. **Hadron shower section** (60 planes of steel). Hadron showers from neutrino interactions in the target section should be contained in this part.

4. **Muon spectrometer section** (161 planes of steel). This part is used to measure the energy of muons, either by ranging them out or by measuring the track curvature.

In the first three sections, only every fifth plane is fully instrumented across the entire plane. The remaining planes are instrumented over only a partial section (illustrated in Figure 3.16) sufficient to cover the neutrino beam events and their accompanying hadronic showers. In the spectrometer section, again every fifth plane is fully instrumented. However, the remainder are not instrumented at all since the requirements for muon tracking are much less stringent.

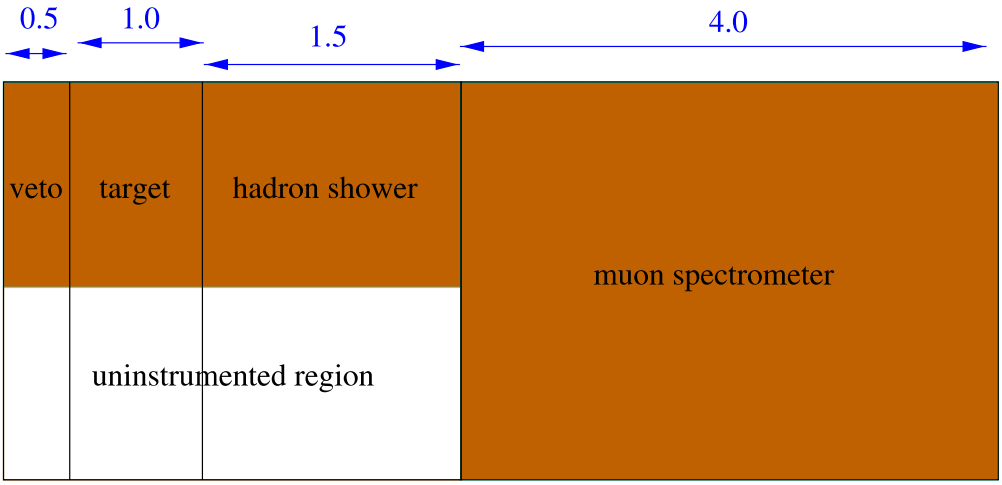

Figure 3.15: Four functional sections of the Near Detector (figure from [4]). The thicknesses (in metres) are for the steel planes only and do not include the scintillator planes. The beam impinges from the left and is centred on the shaded region. The shaded regions are instrumented with scintillator. Note that even in the "uninstrumented" region, every fifth plane is instrumented to cover this region as well.

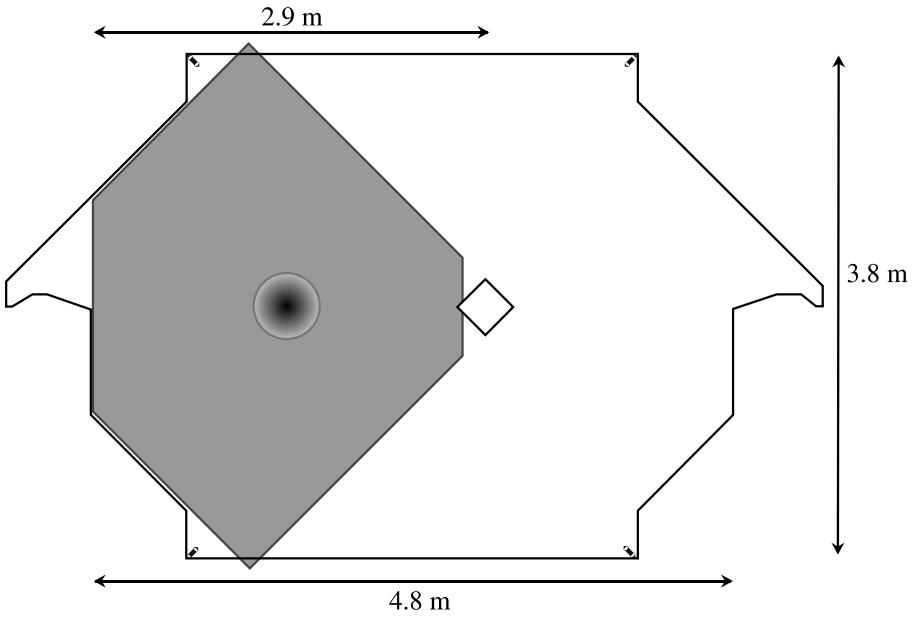

Figure 3.16: Sketch of a partially-instrumented Near Detector plane (figure from [4]). The shaded area is instrumented with scintillator strips which are read out from their outer (left, in this view) end only. The shaded circle indicates the 50-cm diameter beam region, and the square represents the magnet coil hole.

There is no multiplexing of the optical signals, i.e., there is only one fibre per pixel, and only one end of the strip is read out, with a reflector connector of aluminized mylar tape attached to the other end. The photodetectors used are Hamamatsu M64 tubes, which have 64 pixels per tube. However, in the spectrometer section the electrical signals from four PMT anodes are summed together, leading to a fourfold multiplexing.

Since the Near Detector will have to cope with a much higher event rate than the Far Detector, different front-end electronics are used. They are based on the QIE (Charge (**Q**) to Current (**I**) **E**ncoder) [83] electronics developed at Fermilab. The QIE can operate at 53 MHz, is pipelined so that it has no deadtime, and has a 16-bit dynamic range.

The DAQ system operates in three modes:

1. **Single Turn Extraction Mode.** This mode is triggered by a spill signal from the Main Injector. Data is recorded continuously at 53 MHz during the 10-μs spill and stored on FIFOs on the front-end cards. After the spill is finished, the DAQ collects and outputs zero-suppressed data from the FIFOs.

2. **Cosmic Ray Mode.** This mode is in operation during the two-second intervals between spills. This is the same mode in which the Far Detector operates. Data is recorded once a dynode trigger is received. The front-end FIFOs are read out as soon as data is available.

3. **Resonant Extraction Mode.** This mode is in operation during beam spills. As in Cosmic Ray Mode, data recording is triggered a dynode signal. However, the FIFOs are not read out until the end of the spill. This is essentially event-based triggering during beam spills rather than continuous readout.

3.4 Oscillation Analysis

MINOS searches for neutrino oscillations primarily as a disappearance experiment, namely, it looks for the disappearance of ν_μ. This is because, with the low-energy beam, the number of ν_τ with sufficient energy to create a τ-particle (> 4 GeV) will be insufficient for a statistically significant appearance measurement [84]. There are three main aspects to the oscillation analysis [84]: a hypothesis test to establish the existence of neutrino oscillations; measurement of the oscillation parameters Δm^2 and $\sin^2 2\theta$, and appearance tests to constrain parameters in a three-flavour oscillation framework.

3.4.1 The T-Test

A simple hypothesis test that will be used by MINOS is the T-test [85, 86]. The T-test measures the ratio of ν_μ CC events to the total number of events in both the Near and Far Detectors. A statistically significant difference between the ratios gives evidence of neutrino oscillations.

The ratio T is defined as follows:

$$T = \frac{N_{\nu_\mu \text{ CC-like}}}{N_{\nu_\mu \text{ CC-like}} + N_{\text{NC-like}}} \tag{3.1}$$

$$\longrightarrow \frac{N_{\nu_\mu \text{ CC}}}{N_{\nu_\mu \text{ CC}} + \sum_{x=e,\mu,\tau} N_{\nu_x \text{ NC}}} \quad \text{in the limit of perfect event idenfication,} \tag{3.2}$$

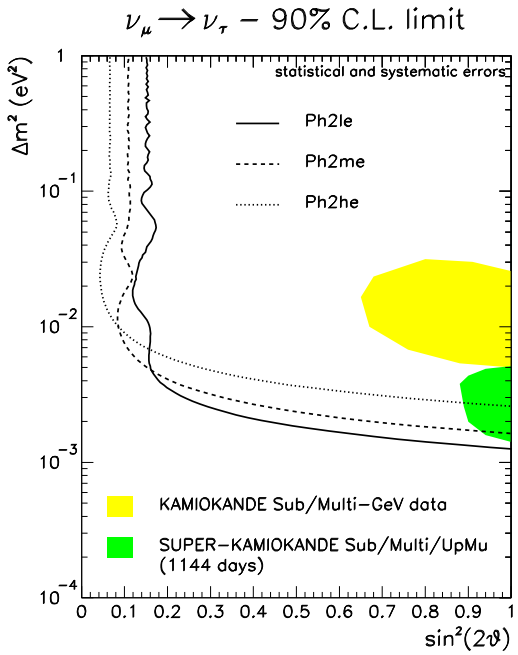

Figure 3.17: 90% confidence limits on $\nu_\mu \rightarrow \nu_\tau$ oscillation parameters using the T-test [86]. The limits shown are for a 5.4-kilotonne detector running for 4 years with 2×10^{20} protons on target per year. The allowed regions for Kamiokande [47] and Super-Kamiokande [60] are shown for comparison.

where all events are classified as either ν_μ CC-like or NC-like, and $N_{\nu_\mu \text{ CC-like}}$ and $N_{\text{NC-like}}$ are the number of events in the respective categories. The ν_μ CC events are identified by a long muon track. For neutrinos with energies greater than 2 GeV, CC events are defined as those events which span at least 35 planes. For lower energies, a Hough transform[2] is used to identify the muon track [88]. The NC-like events will include all NC, ν_e CC and ν_τ CC events. All NC reactions have the same cross-sections regardless of neutrino flavour, and the number of CC events in the NC-like events will be small; thus, the number of NC-like events should remain largely the same regardless of oscillations. Therefore, in the event of oscillations, T will decrease due to the decrease in $N_{\nu_\mu \text{ CC-like}}$.

Figure 3.17 shows the limits that could be set on the $\nu_\mu \rightarrow \nu_\tau$ oscillation parameters at 90% confidence limit for the three neutrino beam configurations. The limits are for 5.4-kilotonne detector running for 4 years with 2×10^{20} protons on target per year. The allowed regions for Kamiokande [47] and Super-Kamiokande [60] are shown for comparison. This shows that with the low-energy beam configuration, the T-test will be able to indicate ($\geq 3\sigma$) the existence of oscillations should they occur with the Super-Kamiokande parameter values.

3.4.2 Measurement of Oscillation Parameters

A more precise measurement of the oscillation parameters can be made by looking at the ν_μ CC energy spectrum in the Far Detector. ν_μ that have oscillated to a different flavour will be

[2]The Hough transform [87] is a method for finding analytic features (primarily straight lines) in two-dimensional images. It transforms coordinates from (x, y)-space into Hough space. If the points in (x, y)-space form a straight line, the lines in Hough space will converge to a single point. Further details of the Hough transform used in MINOS can be found in Appendix A of [88].

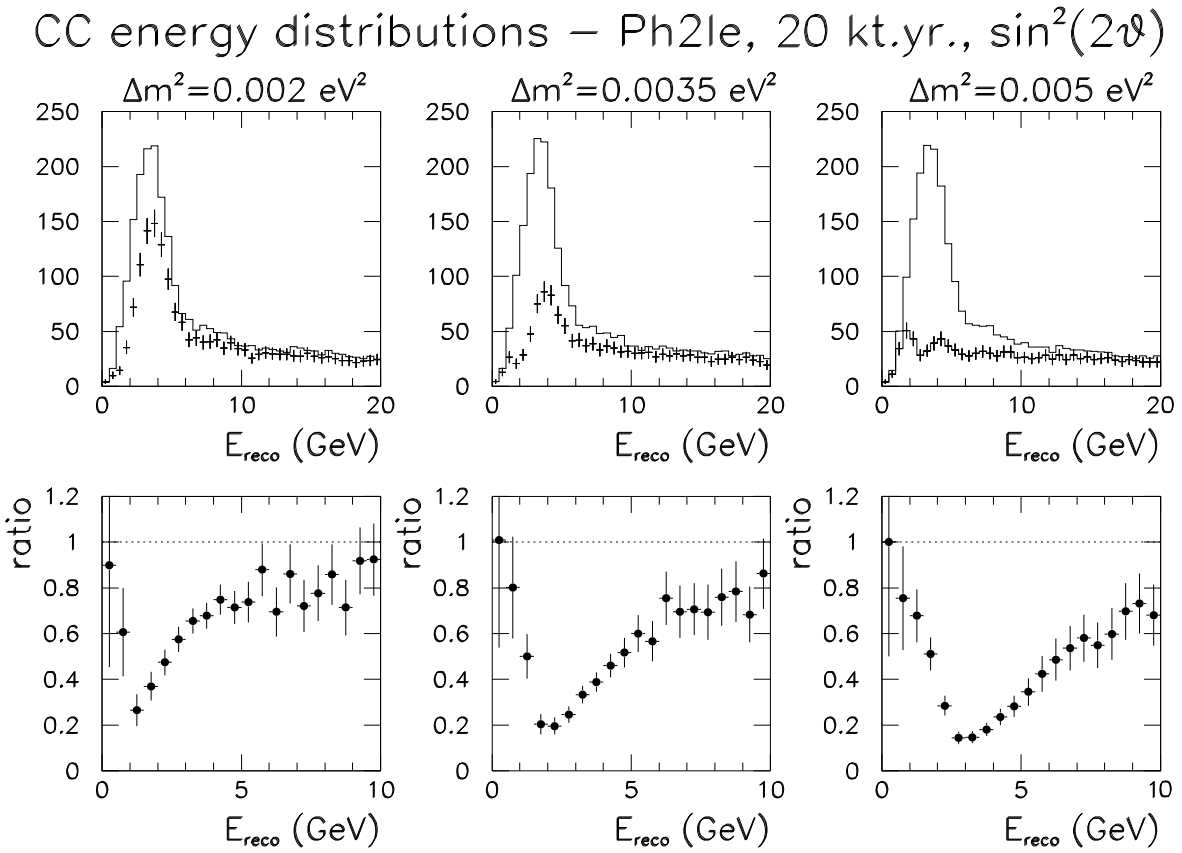

Figure 3.18: Parameter determination using ν_μ CC energy spectra for low-energy beam [84]. Three different values of Δm^2 are used along with $\sin^2 2\theta = 0.9$. The running time and conditions are as in Figure 3.17. In the top row of plots, the solid line shows the CC energy spectrum expected in the Far Detector for no oscillations, and the crosses show the spectrum that would be measured for the given oscillation parameters. The bottom row shows the ratio of these two spectra.

missing from the CC spectrum. These missing events will manifest as a dip in the ratio between the measured spectrum and the spectrum expected in the absence of oscillations. The unoscillated spectrum at the Far Detector will be determined using the CC energy spectrum measured at the Near Detector. The dip in the ratio can be used to determine the oscillation parameters: the depth of the dip gives the value of $\sin^2 2\theta$, and the energy at which the dip occurs determines Δm^2. Therefore, a correct energy calibration will be crucial for MINOS to measure the oscillation parameters accurately.

The top row of Figure 3.18 shows the oscillated and unoscillated spectra in the Far Detector for three values of Δm^2, and the bottom row shows the ratios of the spectra. Note that at the lowest Δm^2 shown, the ability of MINOS to resolve the full dip (i.e., see the ratio start at unity, decrease to its nadir, then increase back towards unity) is at its limit.

Figure 3.19 shows the 90% confidence limit allowed regions for the measurement of $\nu_\mu \to \nu_\tau$ oscillation parameters using the low-energy beam. The limits are for 5.4-kilotonne detector with 7.4, 16 and 25 $\times$ 10^{20} protons on target, roughly equivalent to running for 3, 6.5 and 10 years with 2.5 $\times$ 10^{20} protons on target per year. The allowed region from the L/E analysis of 1489.2 days of Super-Kamiokande data [89] is shown for comparison. This indicates that MINOS will be able to measure the value of Δm^2 more precisely than Super-Kamiokande.

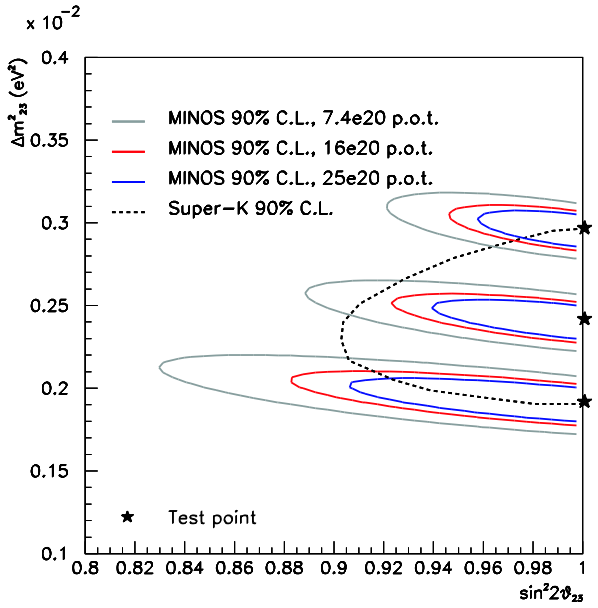

Figure 3.19: Sensitivity of $\nu_\mu \rightarrow \nu_\tau$ oscillation parameter measurements with the low-energy beam using the ratio of CC energy spectra in the Far Detector (figure is an updated version of one found in [88]). The allowed regions at 90% confidence limit are shown for three values of Δm^2.

3.4.3 Appearance Tests

As mentioned at the beginning of this section, searching for ν_τ appearance will not be profitable since the energies of most of the neutrinos from the low-energy beam will be below the creation threshold of the tau-lepton. Figure 3.20 shows the limits obtained from a $\tau \rightarrow \pi + X$ analysis using the high-energy beam, which offers higher energies and higher event rates than the low-energy beam. The limits are for 5.4-kilotonne detector running for 4 years with 2×10^{20} protons on target per year. Even so, MINOS will not be able to cover the Super-Kamiokande allowed region.

Results from Super-Kamiokande [54] and CHOOZ [92] indicate that $\nu_\mu \rightarrow \nu_e$ oscillations in atmospheric neutrinos are strongly suppressed ($< 10\%$). Nevertheless MINOS will attempt to detect ν_e appearance as it will help constrain $|U_{e3}|^2$ in a three-flavour mixing framework (recall $U_{e3} = \sin^2\theta_{13}\, e^{-i\delta}$ from Equation 2.6). The analysis looks at ν_e CC events in the two detectors [91]. Cuts are used to select ν_e CC events and reject NC background. The number of CC events in the Near Detector is used to determine the amount of ν_e beam contamination. The limits that can be obtained are shown in Figure 3.21.

3.5 Calibration of Detectors

A correct energy calibration of the MINOS detectors is crucial to the successful measurement of the oscillation parameters using the ν_μ CC energy spectra; an error of 4% in the relative energy calibration between the Near and Far Detectors can induce a spurious oscillation signal at large $\sin^2 2\theta$ and $\Delta m^2 \sim 10^{-3}$ eV^2 [88], and an error in the absolute energy calibration will cause a shift in the oscillatory dip seen in Figure 2.1 and a corresponding shift in the oscillation parameters measured. To keep systematic errors less than the statistical errors after four years of running, the requirement of the MINOS calibration programme

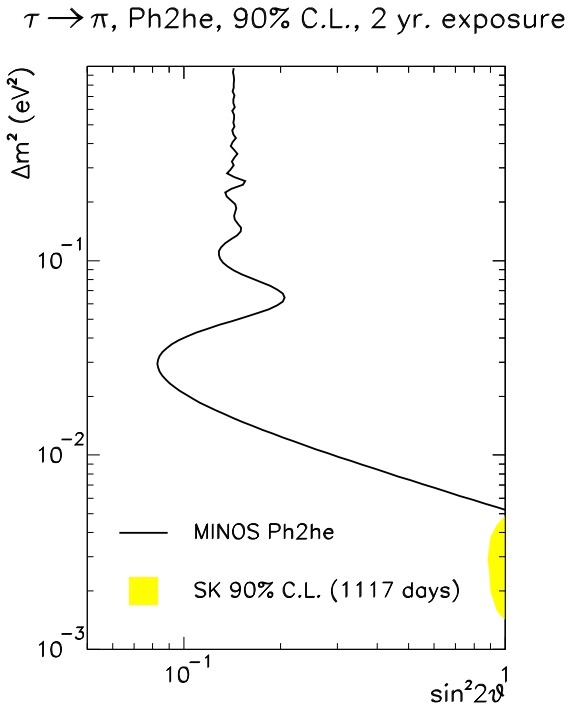

Figure 3.20: 90% confidence limit on oscillation parameters for ν_τ appearance using the high-energy beam [90].

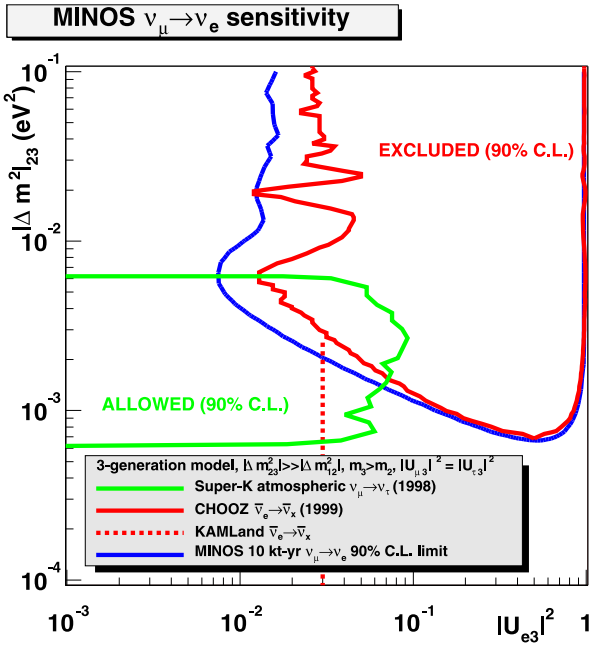

Figure 3.21: 90% confidence limit on $\nu_\mu \rightarrow \nu_e$ oscillation parameters in a three-flavour mixing framework is shown in blue (figure from [91]). Matter effects are included, and the CP-violating phase δ is assumed to be zero. The exclusion limit from CHOOZ, the projected exclusion limit from KamLAND, and the allowed region from Super-Kamiokande are shown for comparison.

is to achieve a 2% relative calibration and a 5% absolute calibration [93].

The ν_μ is identified by the charged-current (CC) reaction

$$\nu_\mu + N \rightarrow \mu^- + X \ , \tag{3.3}$$

which yields a long muon track with an associated hadronic shower. This gives two energy scales, for muons and hadrons, to consider when reconstructing the visible event energy. There is also some invisible energy in the nuclear recoil which must be estimated using Monte Carlo simulations and added to the visible energy to reconstruct the neutrino energy.

There are five main components to the detector calibration: the light injection system, cosmic muons, stopping muons, the Calibration Detector, and the NEUGEN (NEUtrino GENerator) simulation package.

3.5.1 Light Injection System

The light injection (LI) system [94] is used to calibrate the readout system on a timescale of hours. This is primarily to reduce the effects of temperature fluctuations, which affect the gains of the PMTs and electronics, and to reduce nonlinearities in the readout response at high (> 100 photoelectrons) light levels. The LI system calibrates the charge on each readout channel from ADC counts to SigLin (Signal Linearized), which are the ADC counts for a particular light level at a particular reference time:

$$n_i' = C_i^{\text{readout}}(t) \left(n_i + f_i^{\text{nonlin}}(n_i) \right) \ , \tag{3.4}$$

where n_i is the response for channel i in ADC counts, n_i' is the response in SigLin, $C_i^{\text{readout}}(t)$ is the time-dependent calibration constant determined from the LI system, and $f_i^{\text{nonlin}}(n_i)$ is a correction for nonlinearity also determined from LI.

The system is based on pulsed ultra-violet light-emitting diodes (LEDs). Rack-mounted boxes, called pulser boxes, contain 20 LEDs. Each LED illuminates up to 71 clear fibres which transport the light to optical connectors on the back of the pulser box. From there, external clear fibres are connected to the pulser box with the other end inserted into reflective chambers, called light injection modules (LIMs), in the manifolds of the scintillator modules. These LIMs allow the light from the LEDs to illuminate the WLS fibres in the manifold, producing light pulses that emulate signals from the scintillator. Simultaneously, some fibres are connected to the PIN diodes on the VFBs, allowing the intensity of the injected light to be monitored.

3.5.2 Cosmic Muons

The strip-to-strip calibration uses high-energy cosmic muons to produce a uniform response of the scintillator over the entire detector [95]. This response q_i is defined in terms of SigCorr (Signal Corrected), which is the light produced by a high-energy muon incident perpendicularly at the centre of the strip:

$$q_i = C_i^{\text{scint}}(t) n_i' \tag{3.5}$$

where $C_i^{\text{scint}}(t)$ is the calibration constant determined for each strip end i. The timescale of the calibration depends on the cosmic muon flux at the detector, which is different for each detector because they are at different depths underground. It takes one month at the Far

Detector and a few days at the Near Detector in order to accumulate sufficient statistics for each strip in the detector.

High-energy muons are used for the strip-to-strip calibration because the ionization energy loss changes slowly for muons with momenta above the threshold for minimum ionization ($\sim$0.3 GeV/c), according to the Bethe-Bloch equation [9]. This means that the scintillator response will not vary greatly with changes in the muon energy. In practice, through-going muons, i.e., muons which enter and exit the detector, are used because the detectors are sufficiently large that through-going muons will be above the threshold.

3.5.3 Stopping Muons

The strip-to-strip calibration produces C^{scint} that depend on the energy of the cosmic sample used and are thus different at each detector (average energy $\sim$200 GeV at the Far Detector, $\sim$10 GeV at the Near). The absolute energy calibration produces the calibration constant C^{abs} to convert the response for each detector to a standard energy candle. The deposited energy m is expressed in terms of MIPs (Minimum Ionizing Particles):

$$m_i = C^{\text{abs}} q_i \ . \tag{3.6}$$

The calibration requires muons of known energy to calculate C^{abs}. Muons that stop within the detector are used, with the energy being determined from the range within the detector or track curvature. Either cosmic or beam muons can be used. In principle this is a one-off calibration, although it can be repeated every few days.

3.5.4 Calibration Detector

The light injection system, cosmic muons and stopping muons together produce the total energy deposited in the scintillator. However, particles also deposit energy in the steel, and the fraction varies with the type of particle. The Calibration Detector, which is a miniature version of the two main detectors, provides the conversion from energy deposited in scintillator to visible particle energy [96]:

$$E_x^{\text{vis}} = C_x^{\text{vis}} \sum_i m_i \tag{3.7}$$

where E_x^{vis} is the visible energy in GeV for a particle of type $x = e, \mu,$ or hadron, and C_x^{vis} is the calibration constant. In principle this is also a one-off calibration.

The C_x^{vis} were determined by exposing the Calibration Detector to a beam of particles of known energy. The test beams at CERN were used for this purpose. As the Calibration Detector is essentially a third MINOS detector, it first had to be subjected to the same calibrations using the light injection system and cosmic muons to determine its response in MIPs. From there, the visible particle energy scales could be determined. This visible energy calibration could then be applied to the Near and Far Detectors.

3.5.5 NEUGEN

NEUGEN is a general-purpose event generator used to simulate neutrino interactions over the energy range 100 MeV–100 GeV [97]. It was originally developed in the mid-1980s to simulate atmospheric neutrino backgrounds to proton decay for the Soudan-2 experiment [98]. It was later extended and adapted for use in MINOS. It is currently used to

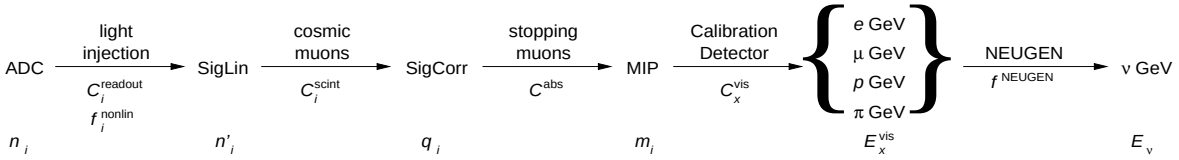

Figure 3.22: Flow chart of detector calibration. The units represent the state of the detector calibration, i.e., to what degree the detector has been calibrated, and the arrows represent the steps in the calibration. Above the arrows are names of procedures used for each step, and below the arrows are the calibration constants or functions used in that calibration step. Below the units are the variables used in the text.

simulate interactions of beam and atmospheric neutrinos in the MINOS detectors. It will also provide the conversion from the visible event energy to the neutrino energy E_ν in GeV:

$$E_\nu = f^{\text{NEUGEN}}\left(E_e^{\text{vis}}, E_\mu^{\text{vis}}, E_{\text{hadron}}^{\text{vis}}\right) \ , \tag{3.8}$$

where $f^{\text{NEUGEN}}(E_x^{\text{vis}})$ is the function which performs the conversion. The actual function may also depend on the kinematics of the interaction.

3.5.6 Summary of Detector Calibration

To summarize, the visible energies for the particles in the event are given by

$$E_x^{\text{vis}} = C_x^{\text{vis}} C^{\text{abs}} \sum_i C_i^{\text{scint}}(t)\, C_i^{\text{readout}}(t)\left(n_i + f_i^{\text{nonlin}}(n_i)\right) \ . \tag{3.9}$$

The E_x^{vis} are then used in Equation 3.8 to determine the neutrino energy. Figure 3.22 is a flow chart of the detector calibration showing the change in units of the measured quantities. It also names the procedure used for each step in the calibration and the C's and f's determined by that procedure. All of these calibrations are performed for the Near and Far Detectors. Since the Calibration Detector is a third MINOS detector, it is also subjected to the relevant calibrations, i.e., light injection and muons. This thesis will describe in detail a procedure for performing the cosmic muon calibration on the Calibration Detector, namely, calculating $C_i^{\text{scint}}|_{\text{CalDet}}$.

— CHAPTER FOUR —

Calibration Detector

4.1 The Detector

The Calibration Detector (CalDet) [100] is essentially a miniature cutout of the two main detectors. It consists of 60 planes that are 1 m square with a pitch of 5.9 cm, and it weighs 12.5 tonnes. The planes are divided into 5 supermodules for easier handling. They are made of the same materials as the two main detectors and have almost the same granularity; the steel plates are 25 mm thick[1] and the scintillator 1 cm. The scintillator modules contain 24 strips of 4.1-cm width which span the front of each steel plate. The strips are oriented vertically and horizontally rather than being canted at 45°.

There are some important differences with the two main detectors. There is no magnetic field for the Calibration Detector, meaning that track curvature cannot be used to determine the energy of muons. On one side of the detector, 6 m of clear fibre connect the scintillator modules to the PMT boxes as in the main detectors; however, on the other side 4 m of WLS fibre are used instead to simulate the greater dimensions of the Far Detector (see Figure 4.3). Readout systems (PMT boxes and electronics) from either the Near or Far Detector could be connected to the fibres.

The Calibration Detector also had a light injection system for calibration.

4.2 Particle Identification

The test beams delivered a mixture of electrons, protons, pions and muons. Additionally, the detector was bombarded constantly by cosmic-ray muons. Special systems were used for particle identification: a Čerenkov detector, a time-of-flight system, and cosmic counters.

A CO_2 Čerenkov detector was placed in the test beam line (see Figure 4.4 for approximate location) to identify electrons and positrons. The pressure in the Čerenkov chamber was adjusted (up to 3.3 bars) so that only electrons and positrons would have velocity above the Čerenkov threshold for the beam momentum used. The Čerenkov PMT signal was digitized using a VFB (and was also modified to serve as a dynode signal for the ASD-lite), and the digitization was output to the general data stream. Figure 4.5 shows a sample ADC spectrum from the Čerenkov detector.

[1] Although the Near and Far Detectors are one inch thick, European steel manufacturers would provide only metric sizes, hence the 0.4-mm discrepancy. This is accounted for in Monte Carlo simulations.

Figure 4.1: Photograph of the Calibration Detector during assembly outside the test beam area. Two humans (∼6' tall) are included to give a sense of scale.

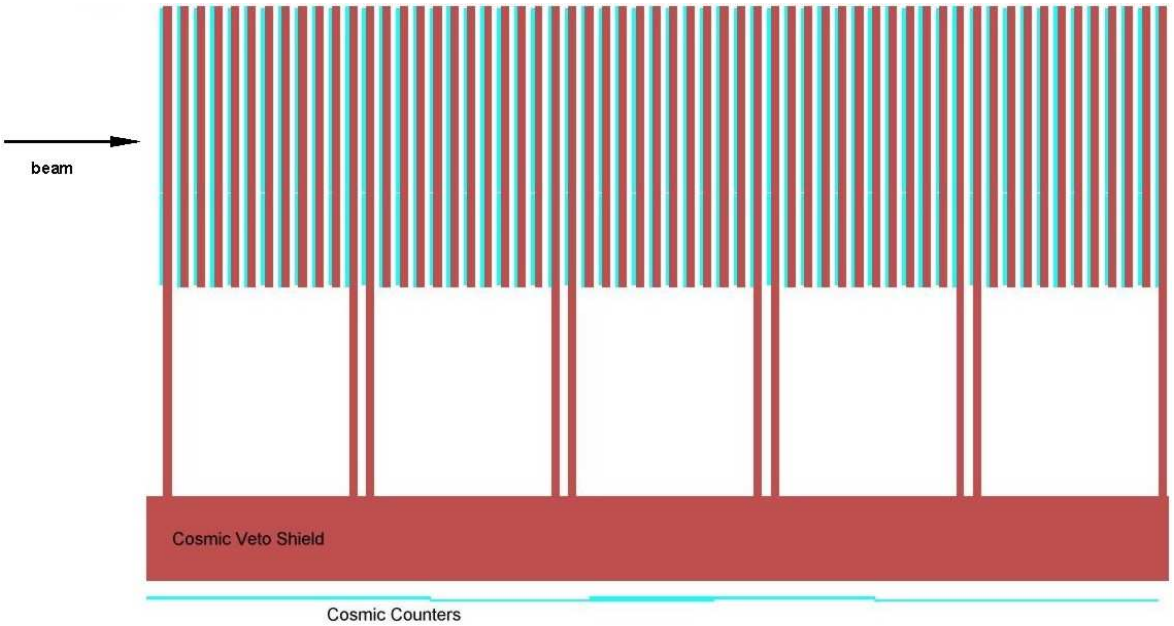

Figure 4.2: Side view of the Calibration Detector as rendered by GEANT [99]. Blue portions represent scintillator modules, and pink represents steel. The test beam enters from the left as shown. The Calibration Detector is divided into five supermodules, each containing 12 planes of scintillator and steel. The detector sits atop a steel block (labelled "Cosmic Veto Shield"), underneath which are 4 scintillator modules which act as cosmic counters.

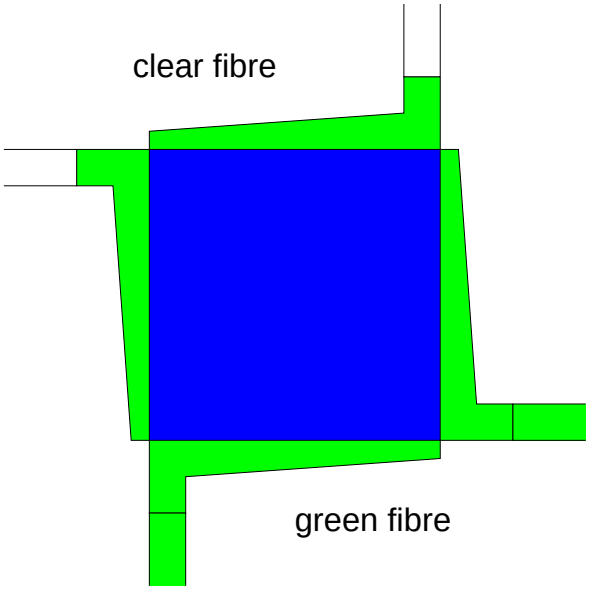

Figure 4.3: Illustration of the green and clear fibre connections between scintillator modules and PMT boxes in the Calibration Detector. The perspective is looking along the beam direction at the front face of the detector. The blue area represents the scintillator strips with WLS fibres. The green manifolds represent the WLS fibre pigtails. Connected to the top and left manifolds are 6-m clear fibres; bottom and right are 4-m WLS fibres.

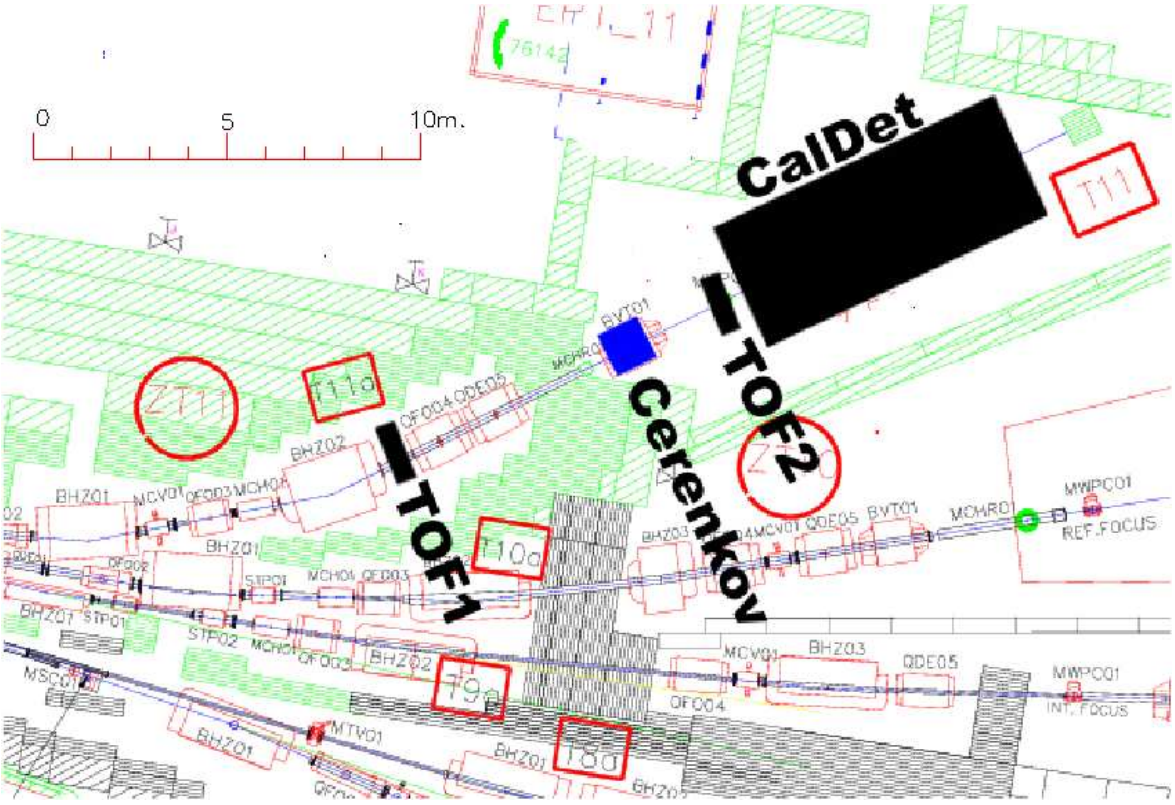

Figure 4.4: Layout of the Calibration Detector in the T11 test beam area (figure from [99]). Positions of the Čerenkov detector and the TOF paddles are also shown. The green hatched regions are concrete blocks shielding the beamline, and the rectangular objects with red outlines along the beamline are magnets for focussing the beam. The Calibration Detector, Čerenkov detector and TOF paddles are not drawn to scale.

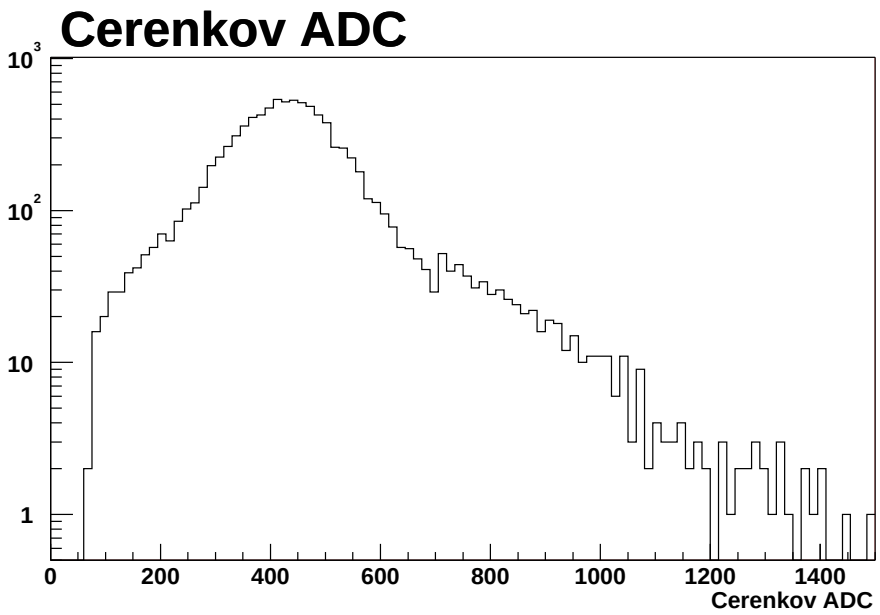

Figure 4.5: ADC spectrum from the Čerenkov detector (figure from [99]). This spectrum is from a run with the T11 test beam momentum set to 0.8 GeV/c.

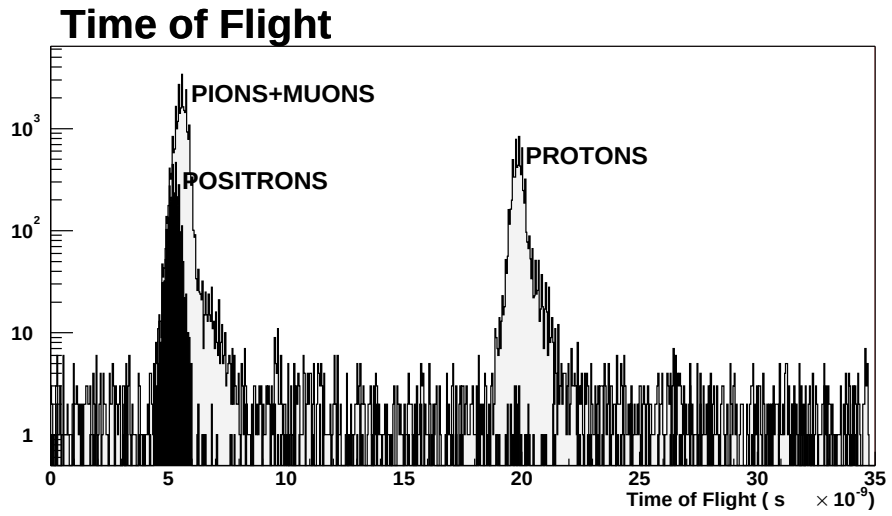

Figure 4.6: Time-of-flight spectrum from the TOF system (figure from [99]). This spectrum is from a run with the T11 test beam momentum set to 1.4 GeV/c. The peak of relatively slow protons is separated from the peak of relativistic particles (pions, muons and positrons). Events associated with a Čerenkov signal (positrons) are shown in black.

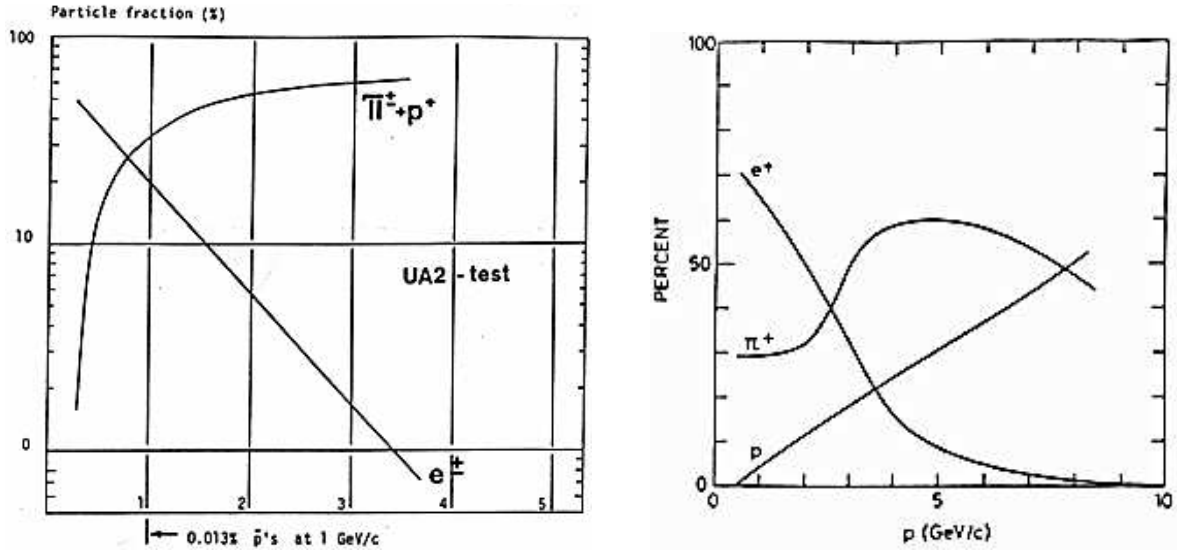

(a) T11 beam spectrum.

(b) T7 beam spectrum.

Figure 4.7: Particle fractions in the PS test beams (figures from [101]).

The time-of-flight (TOF) system was used to differentiate protons from pions and muons. It consisted of two scintillator paddles, each a 2.54-cm square of scintillator with a thickness of 1 cm optically coupled to a PMT. One paddle (TOF2 in Figure 4.4) was placed a few centimetres upstream of the centre of the front face of the Calibration Detector, and the other (TOF1) was placed 11.8 m upstream from there. The PMT signals were passed to a constant fraction discriminator and checked for a coincidence within a 100-ns time window. If a coincidence was found, the time difference was output to the general data stream. Figure 4.6 shows a typical time-of-flight spectrum from the TOF system. It shows the proton peak clearly separated from the peak containing pions, muons and positrons. The positrons could be distinguished by using the Čerenkov detector. Pions and muons had to be separated using some other technique such as event topology.

The cosmic counters were used to identify high-energy cosmic muons. The counters were four scintillator modules that were laid flat on the ground. A steel platform 30 cm thick was placed over the counters to absorb low-energy particles. The Calibration Detector sat atop the platform. Figure 4.2 shows the layout of these components. The counters were connected via clear fibres to standard MUX boxes and were read out along with the rest of the data.

4.3 CERN Test Beam Runs

The Calibration Detector was exposed to test beams produced from the PS ring at CERN. The test beams used were the T11 and T7 beams [101], which could deliver electrons, protons, pions and muons (see Figure 4.7 for beam composition) at a momentum specified by the users. The T11 beam can deliver particles of momentum 0.2–3.5 GeV/c, and the T7 beam can deliver 0.5–10 GeV/c. The momentum bite is 2% for the T11 beam and 1% for T7.

The Calibration Detector was exposed to the test beams during six separate periods (see Table 4.1 for summaries of each period):

Period	Dates	Beam	Electronics
I	08/01–09/01	T11	Far
II	06/02	T7	Far
IIIa	early 09/02	T11	hybrid
IIIb	late 09/02	T11	Far
IV	10/02	T7	Far
Va	early 09/03	T7	hybrid
Vb	late 09/03	T7	Near
VI	10/03	T11	Near

Table 4.1: Summary of test beam runs.

Period I (August–September 2001) in T11 This was largely a commissioning run since it was the first time the Calibration Detector had been run in a test beam, although an attempt was made to take low-energy beam data. Far Detector readout systems were used for both ends of each strip. An offline trigger, requiring that 4 out of 5 adjacent planes be read out, was used. However, beam event rates were much higher than the rates for which the VA electronics had been designed, resulting in significant problems due to electronics deadtimes.

Period II (June 2002) in T7 Following the high rate problems of 2001, a hardware trigger requiring a coincidence in the TOF system was implemented for this and subsequent periods. This period was used to take high-energy beam data. Far Detector readout was used for both strip ends.

Period IIIa (early September 2002) in T11 This was largely a commissioning run for the first use of Near Detector readout systems. Six planes were instrumented on one side with Near Detector PMT boxes and electronics; the remaining 54 planes on that side were left uninstrumented. The other side of all 60 planes was instrumented with Far Detector readout. This hybrid combination was used to compare the performance of the two readout systems.

Period IIIb (late September 2002) in T11 This period was used to repeat the low-energy beam measurements of 2001, but this time using the TOF trigger. Data was also taken with the supermodules rotated 30° to study the effects of particles entering at oblique angles. Far Detector readout was used for both strip ends.

Period IV (October 2002) in T7 This period was used to take additional high-energy beam data with Far Detector readout for both strip ends.

Period Va (early September 2003) in T7 This was the first data-taking with the full hybrid readout system. The strips were fully instrumented on one end with Near Detector readout and on the other with Far Detector readout. Both low- and high-energy beam data was taken.

Period Vb (late September 2003) in T7 This was the first data-taking with a fully Near Detector setup. One end of each strip was connected with clear fibres to Near Detector readout, while the other was connected to WLS fibres with reflector connectors of aluminized

mylar attached on the ends of the fibres. There was one week of running with 3-m WLS fibres, followed by another week with 1-m fibres. This was done to simulate the size of the Near Detector. High-energy beam data was taken during this period.

Period VI (October 2003) in T11 Some final low-energy beam data was taken during this period with the Near Detector only setup. Data was also taken with the supermodules at an angle.

The Calibration Detector also took cosmic muon data between these periods with Far Detector readout on both strip ends, and between test beam runs within each period with the same setup as for the beam runs. During Period I cosmic muon data was also taken between beam spills during beam runs. Additionally, in June 2003 cosmic data was taken with Far Detector readout on one side and reflector connectors on the other. The 4-out-of-5 trigger was used for all cosmic data runs. This thesis is concerned primarily with cosmic data from Period I.

— CHAPTER FIVE —

Reconstruction of Muon Tracks in the Calibration Detector

The first step in the calibration using cosmic muons is to reconstruct the muon tracks. In the Calibration Detector, which has a thickness of 785 g/cm^2 vertically and 1177.5 g/cm^2 horizontally and is illuminated by cosmic muons with average energy $\approx$ 4 GeV [102], these tracks are straight (barring hard or multiple scatters) because there is no applied magnetic field. This chapter will describe the package developed to reconstruct such tracks.

5.1 Event Reconstruction in `loon`

Event reconstruction is performed in `loon` (Lookit [sic] those Object-Oriented Neutrinos!)[1], the offline reconstruction software for MINOS [103]. It is based on ROOT, the data analysis framework developed at CERN and based on C++ [104].

The DAQ system produces ROOT files containing *digits*, short for *digitizations*, for each *snarl* in a run. The digits are the charges, expressed in ADC counts, for each channel. One digit corresponds to the readout from a single channel. A snarl is the readout of a time slice from the Data Collection Process (recall Section 3.2). A snarl is equivalent to a single event in the Far Detector and also in the Near Detector when it is run in either the Cosmic Ray Mode or Resonant Extraction Mode. When the Near Detector is run in Single Turn Extraction Mode, a snarl corresponds to an entire beam spill and may contain several events. These ROOT files are then used by `loon` for event reconstruction.

The reconstruction path, shown in Figure 5.1, is performed on each snarl:

- The first step is to perform demuxing[2] (short for "demultiplexing") for the Far Detector to produce *demuxed digits*. Each demuxed digit is associated with a unique strip end. This step is superfluous for the Near and Calibration Detectors.
- The demuxed digits are then collected into *strips*. The strips may contain digits from either or both strip ends.

[1] The loon is the state bird of Minnesota.

[2] For each digit there is an eightfold ambiguity as to with which strip it is associated. The demultiplexing algorithm [105, 106] resolves this ambiguity and determines the associated strip for each digit. For planes with digits on opposite sides, the digits are associated with their common strip alternative. Should any unpaired digits remain, their associated strips are determined by correlating with upstream and downstream information.

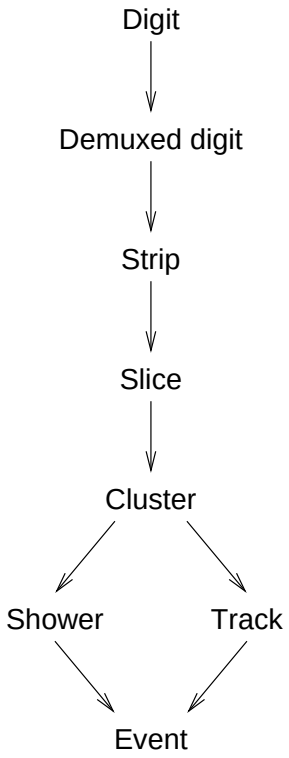

Figure 5.1: Event reconstruction path in `loon`.

- The strips are then divided into time *slices*, which correspond to single real events. This step is needed primarily for the Near Detector in Single Turn Extraction Mode, although it is also useful in the other modes and detectors when there is event pileup in a single snarl.

- For each slice, the strips are then formed into *clusters*, which are 2-dimensional associations of spatially adjacent strips. This is done for each view, and there may be multiple clusters in each view.

- The clusters from opposite views can then be merged to form 3-dimensional objects, either *showers* or *tracks*.

- The various showers and tracks which are spatially and temporally correlated are formed into *events*. From here, cuts can be applied to identify the particle interaction.

Different algorithms can be used depending on the event being reconstructed.

In all detectors, the uvz-axes define a right-handed orthogonal three-dimensional coordinate system used for reconstruction. The orientation of the axes is illustrated in Figure 5.2. The z-axis is defined to be horizontal along beam direction, i.e., increasing plane number. The u- and v-axes are defined along the increasing strip number within the two projections. For the Calibration Detector, the v-axis is vertical and the u-axis horizontal. The first plane of the Calibration Detector is a v-view plane.

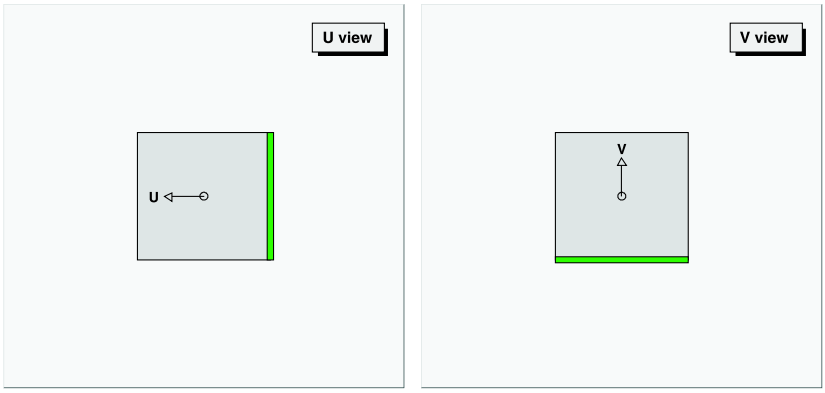

Figure 5.2: Plane views for the Calibration Detector (figure provided by [107]). Strip 0 in each view is shown in green. The strips in the u-view are oriented vertically such that strip number measures distance horizontally. The strips in the v-view are oriented horizontally such that strip number measures distance vertically.

5.2 The BubbleSpeak Package

The BubbleSpeak package was developed by this author for use in `loon` to reconstruct straight tracks from demuxed digits. It was originally developed for cosmic muons in the Far Detector and has been adapted for cosmic and beam muons in the Calibration Detector. The algorithms and parameters described here are for the Calibration Detector.

5.2.1 Strip Formation

The first step, once any necessary demuxing has been done (none needed for the Calibration Detector), is to create strips from the digits. This is done simply by sorting the digits by plane and strip number, then looping over the sorted list to associate digits on opposite ends of strips.

5.2.2 Clustering

The purpose of clustering is to eliminate digits that do not belong to the track, including those caused by noise and PMT cross-talk. The clustering algorithm[3] assumes that double-ended strips, i.e., strips with digits from both ends, have been traversed by a particle rather than being the coincidence of two cross-talk or noise digits. (On average there are $\sim$8 cross-talk and noise digits per event.) It also assumes that cross-talk and noise produce digits with lower charge (1 photoelectron) than those produced by particles (typically 4 photoelectrons for minimum-ionizing particles). The two views are treated independently. The double-ended strips in each view are fitted by a straight line, weighted by the charge of the strip to de-emphasize noise and cross-talk digits, to establish a central track which acts as a seed for the next step. This is illustrated for an example event in Figure 5.3(a). For the u-view, the fitted line is given by

$$u = mz + b \,, \tag{5.1}$$

[3]Originally, an algorithm to merge nearby clusters was developed for the Far Detector. However, this algorithm did not prove as successful for the Calibration Detector. Details can be found in Appendix B.

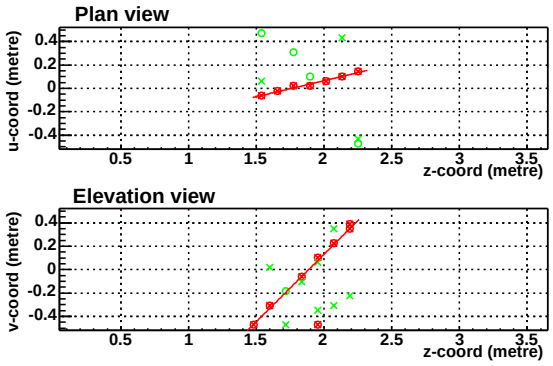

(a) Establishing the seed track. The red symbols indicate double-ended strips, and the green are for single-ended strips. A straight-line track, shown in red, is fitted to the double-ended strips, weighted by charge. This fitted track, shown in red, forms the seed for the next step in the clustering algorithm.

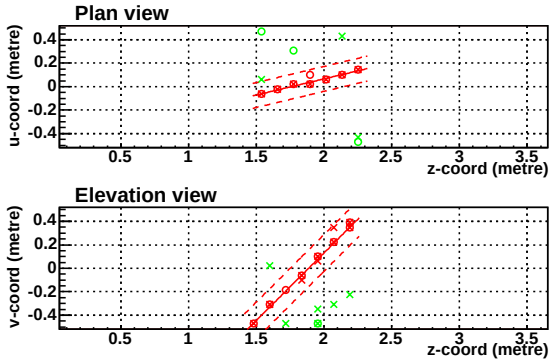

(b) Adding strips to the main cluster. The fitted track from the previous step is shown as a solid red line. Two boundaries are established 10 cm on either side of the fitted track and are demarcated by the dashed red lines. Any strips, be they single- or double-ended, that lie within this band are added to the main cluster and are shown in red. Those strips that lie outside the band, shown in green, are discarded and not considered in the next step of the reconstruction.

Figure 5.3: Example of clustering a CalDet event showing the two steps. The event shown is a cosmic muon entering through the top of the detector and exiting out the bottom. In each diagram, the plan (u) view is shown on top and the elevation (v) view on bottom. The circles and crosses represent the digits of the event and mark the locations of the strips with which the digits are associated. The different symbols represent opposite ends of the strips.

where the fit parameters m and b are calculated as

$$m = \frac{\sum_i w_i \sum_i w_i u_i z_i - \sum_i w_i u_i \sum_i w_i z_i}{\sum_i w_i \sum_i w_i z_i^2 - \sum_i w_i z_i \sum_i w_i z_i} , \tag{5.2}$$

$$b = \frac{\sum_i w_i u_i \sum_i w_i z_i^2 - \sum_i w_i u_i z_i \sum_i w_i z_i}{\sum_i w_i \sum_i w_i z_i^2 - \sum_i w_i z_i \sum_i w_i z_i} , \tag{5.3}$$

where i runs over all double-ended strips, w_i is the charge (in ADC counts) of strip i, and u_i and z_i are the u- and z-coordinates respectively of strip i (similarly for the v-view).

In the next step, any strips, be they single- or double-ended, that lie within 10 cm of this seed track are added to the main cluster. Any strips that lie outside this band are considered to be cross-talk and are discarded from further consideration in the reconstruction. This band clustering is done for each projection. The results for the example are shown in Figure 5.3(b).

The basis for the 10-cm cut is illustrated in Figure 5.4. Figure 5.4(a) shows the distribution of the perpendicular distance between the reconstructed strip and the central track. Close to the fitted track, the distribution is dominated by double-ended strips, shown in red. Farther from the track, the double-ended distribution tails off steeply, leaving the single-ended strips in green to dominate. This suggests that double-ended strips near the track result from particle hits, whereas all other double-ended strips and single-ended strips result from cross-talk and noise. Looking at the distribution of charge per strip end (see Figure 5.4(b)) confirms that the distribution for double-ended strips within 10 cm of the track looks like that for a minimum-ionizing particle, whereas the other distributions look appropriate for single photoelectrons. Therefore, a 10-cm cut is reasonable for the band clustering algorithm. A stricter cut of 5 cm is used later for track fitting (see Section 5.2.3).

In Figure 5.4(a), the plan view distribution on the left has a plateau around 0.5 m, whereas the elevation view distribution on the right tails off over most of the range. As illustrated in Figure 5.5, this results from cross-talk digits and track geometry. Since most cosmic muons are downward-going, they will span the detector from top to bottom in the elevation view, sometimes quite steeply; therefore, cross-talk digits, which reconstruct as being $\sim$0.5 m away from the original track digit in the same plane, will typically have a perpendicular distance from the track less than 0.5 m. In the plan view, however, cosmics can travel parallel or nearly so to the beam direction; for such tracks the cross-talk digits will have a perpendicular distance of $\sim$0.5 m, hence the plateau. The entries beyond 0.6 m are from noise digits on planes separated from the track.

5.2.3 Track Reconstruction

The next step in reconstruction is to identify potential muon tracks. The clustering step has produced two clusters, one in each projection. The first step in track identification is to decide whether these two clusters match up. Figure 5.6 shows the distribution of differences in plane number of the ends of the u-view and v-view clusters. If the downstream end of the clusters lie within one plane of each other, i.e., $\Delta\text{plane} = \pm 1$, they are considered to match. The same is done with the upstream ends of each cluster. If both upstream and downstream ends match, then the two clusters together are considered to form a track. The apparent asymmetry favouring a u-view plane number higher than the v-view plane number, i.e., $\Delta\text{plane} = 1$, arises because the first plane is a v-view plane and the last is a u-view plane. Any tracks that end in either of these planes will have $\Delta\text{plane} \geq 1$. The red distribution, which excludes such tracks, is symmetric for the $\Delta\text{plane} = \pm 1$ bins.

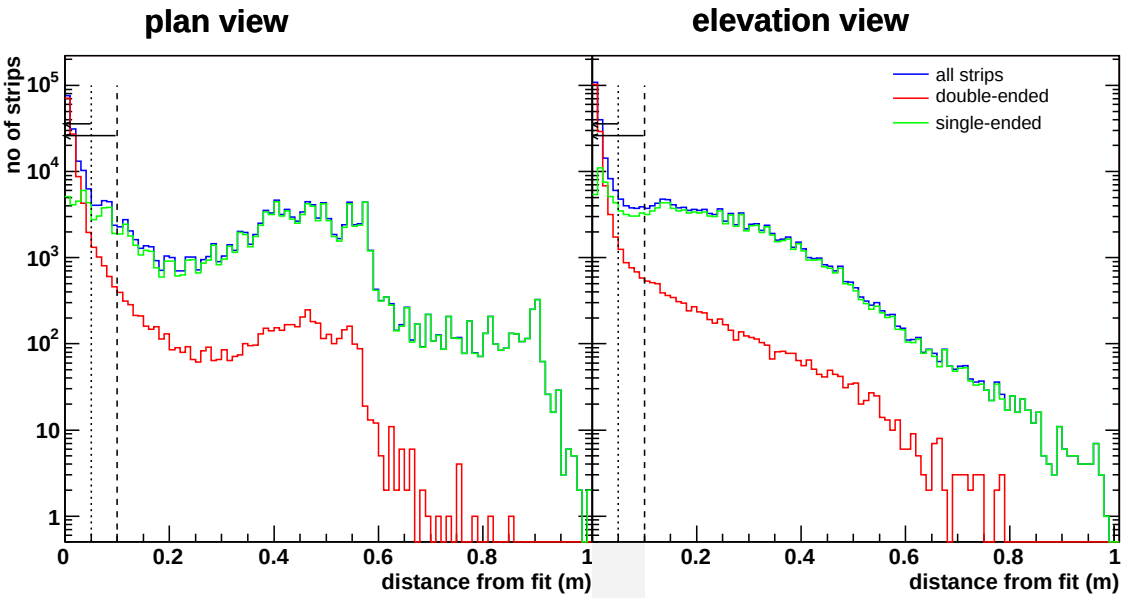

(a) Distance of reconstructed strip from fitted central track. The plot on the left is for the plan (u) view, and the one on the right is for the elevation (v) view. The blue distribution is for all strips. The red distribution is for all double-ended strips and represents digits potentially produced by a particle track. The green distribution is for all single-ended strips and represents digits probably produced by cross-talk and noise. The dashed line indicates the 10-cm cut used in the clustering algorithm. The dotted line indicates the 5-cm cut used in the track fitting algorithm described in Section 5.2.3.

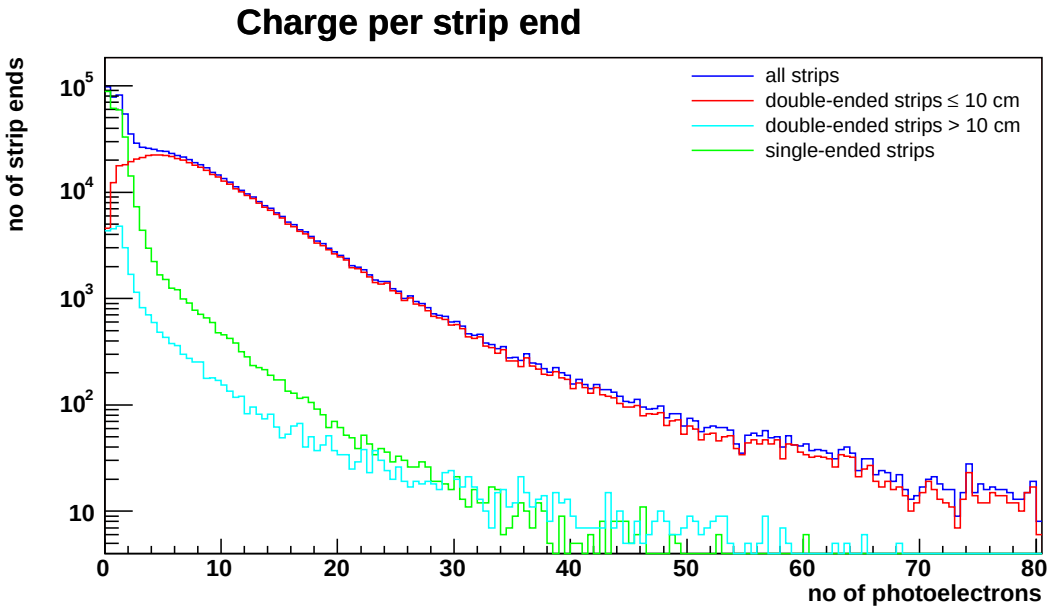

(b) Charge in npe (number of photoelectrons) per strip end. The blue spectrum is for all strips, be they single- or double-ended. The red spectrum is for double-ended strips with distance from the fitted track $\leq$ 10 cm. The cyan spectrum is for double-ended strips with distance from the fitted track $>$ 10 cm. The green spectrum is for all single-ended strips.

Figure 5.4: Determination of 10-cm band width cut in band clustering algorithm.

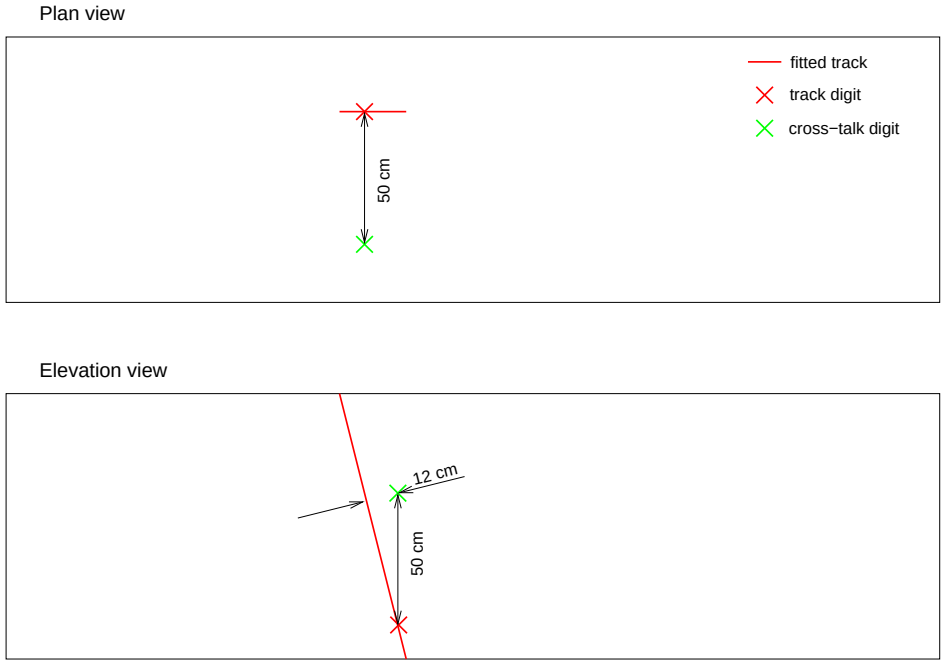

Figure 5.5: Illustration of distance of cross-talk from track. In the plan view, in which the track is parallel to the beam direction, the cross-talk digit is 50 cm away from the original track digit and is also 50 cm away from the track. In the elevation view, in which the steep track is nearly perpendicular to the beam direction, the cross-talk digit is again 50 cm away from the original track digit but only 12 cm away from the track.

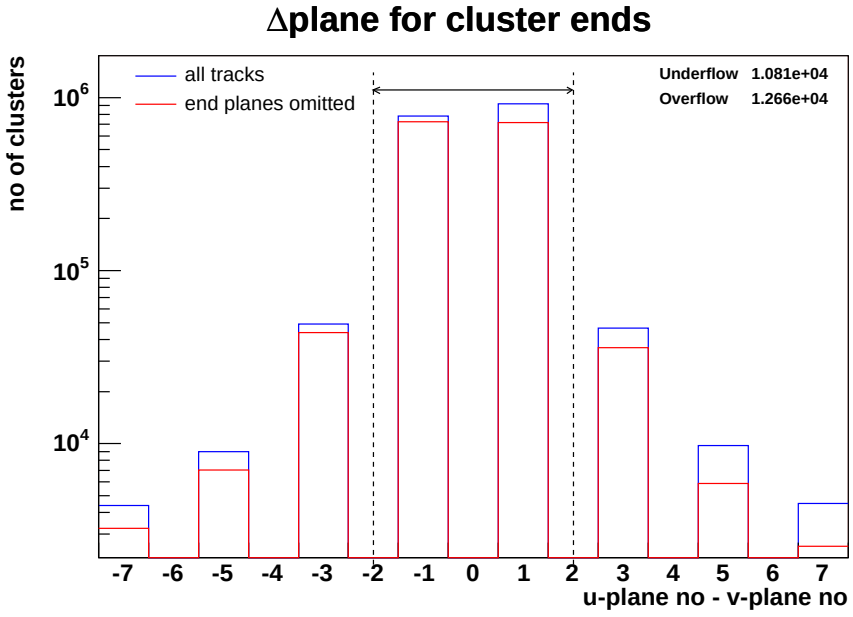

Figure 5.6: Difference in planes of ends of u-view and v-view clusters. Both upstream and downstream ends are shown in the same distribution. The blue distribution includes all reconstructed tracks. The red distribution excludes tracks that end at the first or last plane of the detector. The dashed lines demarcate the acceptance cut.

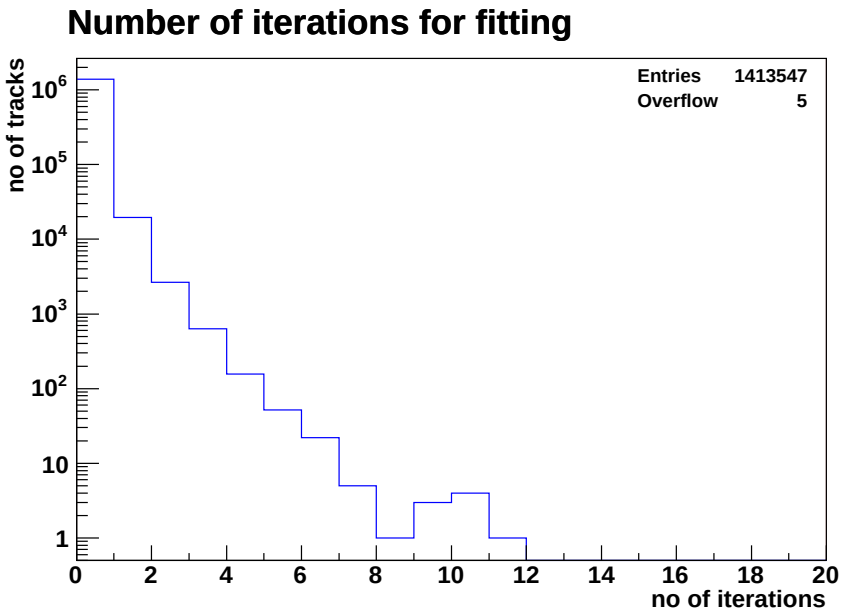

Figure 5.7: Number of iterations for track fitting. The overflows represent cases when the fit iterations oscillate between two different states.

Next, the digits that form the track itself are identified. In each projection a straight two-dimensional line is fitted to the strips in the main cluster with the strips weighted by the charge (recall Equations 5.1–5.3, but with i running over all strips in the cluster). Any strips that lie within 5 cm of the fitted line are considered to be part of the track, and all others are not. This is the same principle as that shown in Figure 5.3(b), but with a narrower band. Then another straight line is fitted to the strips that are part of the track. With this new fitted line, again any strips within 5 cm of said line are considered to be part of the track, whether they were previously or not, and all others are not. Another straight line is fitted, and the process of selecting and deselecting strips based on proximity to the fitted line is again reiterated. This iteration continues until either no change is made between iterations, or 20 iterations have been complete. The latter condition is to handle the case when the iterations oscillate between two different states. As can be seen from Figure 5.7, this is an exceedingly rare occurrence ($< 10^{-5}$). The strips that remain at the end form the track.

In general the tracks are assumed to be for downward-going particles, so the vertex (track origin) is set to be at the location of the spatially topmost digit. However, the same algorithm is used for identifying beam muons. If a track has digits in any of the first three planes, it is assumed to be a track for a beam particle, and the vertex is therefore set to be at the location of the most upstream digit. This will cause a misidentification of the vertex for cosmics that enter through the top of the detector and exit through the front face, but such particles should miss the cosmic counters and therefore should not present a problem.

Figure 5.8 shows examples of reconstructed tracks. In the clustering diagrams on the left, there appear to be ghost tracks among the discarded green digits. These are due to the fibre lacing pattern in the MUX boxes which causes cross-talk digits to mirror the main track.

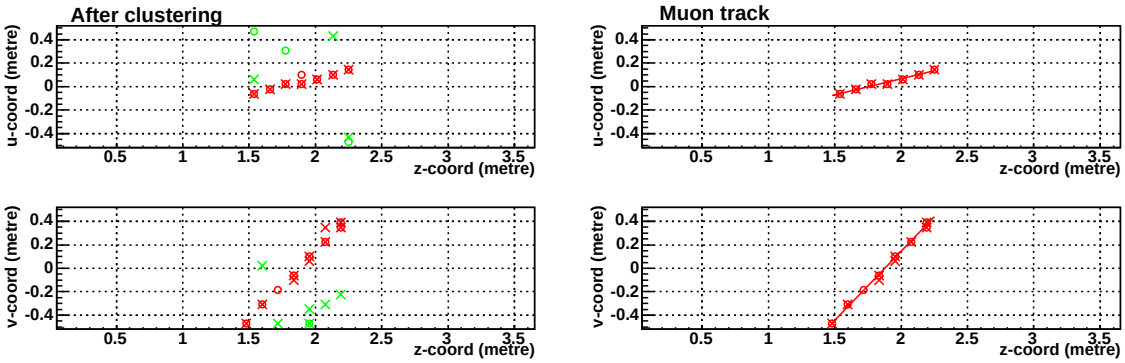

(a) Typical cosmic muon entering through top of detector and exiting out bottom. This is the same event as shown in Figure 5.3.

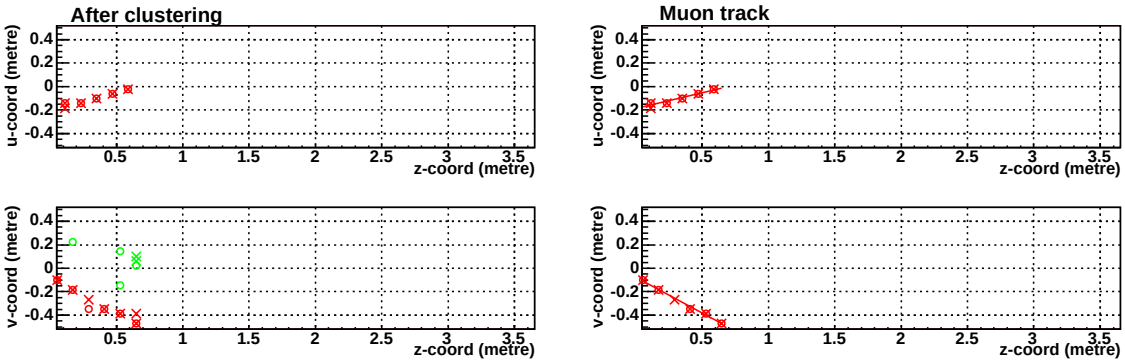

(b) Cosmic muon entering through front of detector.

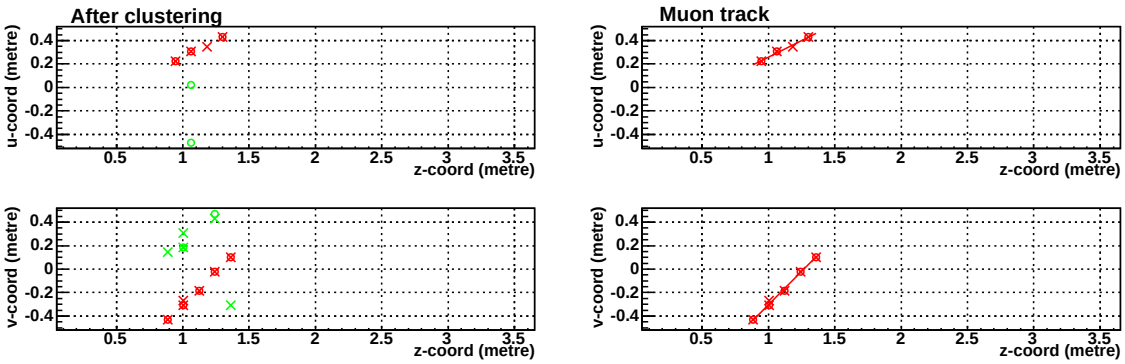

(c) Cosmic muon entering through side of detector.

Figure 5.8: Reconstruction of cosmic muon tracks. The format of the diagrams are the same as in Figure 5.3. The diagrams on the left display the results of clustering. The red symbols represent digits that are in the main cluster and thus retained for the track identification. The green symbols represent digits that have been discarded by the clustering and are not considered in the track identification. The diagrams on the right display the fitted track. Only the digits that have been retained in the fitted track are shown. The solid red line is the final fitted track.

— CHAPTER SIX —

Strip-to-Strip Calibration of the Calibration Detector

This chapter describes the strip-to-strip calibration developed by this author and applied to the Calibration Detector. The purpose of the strip-to-strip calibration is to define a uniform response of the scintillator across the detector by calculating the C_i^{scint} (as defined in Section 3.5) for each strip end. Normally this converts from SigLin units to SigCorr units. However, at the time this analysis was done the light injection calibration was not yet available. Instead a PMT gain calibration C_i^{PMT} was used to convert from ADC counts to npe (number of photoelectrons), and then the $C_i^{\text{scint}'}$ would convert from npe to SigCorr:

$$\begin{aligned} p_i &= C_i^{\text{PMT}}(t) n_i \ , \\ q_i &= C_i^{\text{scint}'}(t) p_i \ , \end{aligned} \tag{6.1}$$

where p_i is the response for channel i in npe and n_i, q_i are as defined in Section 3.5. Despite the fact that the calibration starts from npe rather than SigLin, the principle behind the calibration is still valid and can be applied in the same manner once the light injection calibration is available.

The data presented in this chapter is from 2001 test beam runs unless specified otherwise. Therefore, beam events are interspersed with cosmic muon events. The two downstream (with respect to the test beam) cosmic counters were read out on both sides, but due to faulty MUX boxes the two upstream cosmic counters were read out on one side only.

6.1 Calibration Method

The approach is to define a sample of minimum-ionizing (or nearly so) muons and use that to calculate a conversion factor for each strip end in the detector. High-energy muons are used because, while the ionization increases as muon energy increases, it does so only logarithmically. This means that high-energy muons can be treated as minimum ionizing to first order. Cosmic muons are used as this allows illumination of all three detectors.

For the method described here, a sample of cosmic muons is collected over a period of time. For each muon its track is reconstructed. In the Near and Far Detectors, only those which are through-going, i.e., enter and exit the detector, are retained as they have travelled through a substantial amount of detector material and are therefore high energy. Also, only those whose track can be fitted by a straight line are retained to simplify the track fitting.

This further ensures that the muons have high energy as otherwise their tracks would be significantly deflected by the magnetic field. In the Calibration Detector, its small size and lack of magnetic field mean that muons that are through going and have straight tracks may still have low energy; therefore, the cosmic counters are used to select muons that have passed through the 30-cm steel and are at least minimum ionizing.

Once the sample of cosmic muons has been collected, the calibration constants can be calculated. For each strip end in the detector, the charge deposited by each muon passing through that strip is histogrammed. Then, at the end of the appointed period, the mean of the histogram is used as the conversion factor for that strip end. This should provide a uniform response across the detector in SigCorrs.

6.2 Location of Cosmic Counters

The precise locations of the cosmic counters were not well defined because the counters were shoved underneath the steel plate, so the first task was to determine their positions. The strips in the cosmic counters ran longitudinally so that decreasing strip number measured increasing distance in the transverse (u) direction. Initially, the counters were assumed to be centered transversely. The reconstructed tracks were extrapolated down to the level of the counters (1.1 m below the bottom face of the detector) to determine which strip number s_{proj} should be hit:

$$u_{\text{proj}} = \frac{\cos\theta_u}{\cos\theta_v}\left(1.6\text{ m} - v_{\text{vertex}}\right) + u_{\text{vertex}}\ , \tag{6.2}$$

$$s_{\text{proj}} = -\frac{u_{\text{proj}}}{w} + 12\ , \tag{6.3}$$

where

$u = 0, v = 0$ is defined to be the centre of the detector;
$u_{\text{vertex}}, v_{\text{vertex}}, z_{\text{vertex}}$ is the entry vertex of the muon track;
u_{proj} is the extrapolated transverse location of the track;
$\cos\theta_u, \cos\theta_v, \cos\theta_z$ are the components of the track direction vector;
1.6 m is the vertical distance from the centre of the detector to the cosmic counters;
$w = 4.1$ cm is the width of the scintillator strips.

The digits (defined in Section 5.1) from cosmic counter hits were searched for a match with the projected strip number, i.e., $s_{\text{digit}} = s_{\text{proj}}$. Where there were multiple digits with the desired strip number, either from different counters or from opposite strip ends, the one with the highest charge in ADC counts n_{digit} was retained. The counter number c_{digit} was plotted versus the extrapolated longitudinal (z) position in Figure 6.1(a). The cosmic counters, outlined in black, were defined to cover the most populous bins.

The process was then reversed to find any offset of the cosmic counters in the transverse direction. The extrapolated end point of the track determined which counter number c_{proj} and strip number s_{proj} should be hit, and the cosmic counter digits were searched for matches with $c_{\text{digit}} = c_{\text{proj}}$. Note that since the cosmic counters overlapped each other in z, there could be multiple valid values of c_{proj}. Where there were multiple digits found, the one with a strip number closest to the desired one was retained, i.e., $|\Delta s| = |s_{\text{digit}} - s_{\text{proj}}|$ minimized,

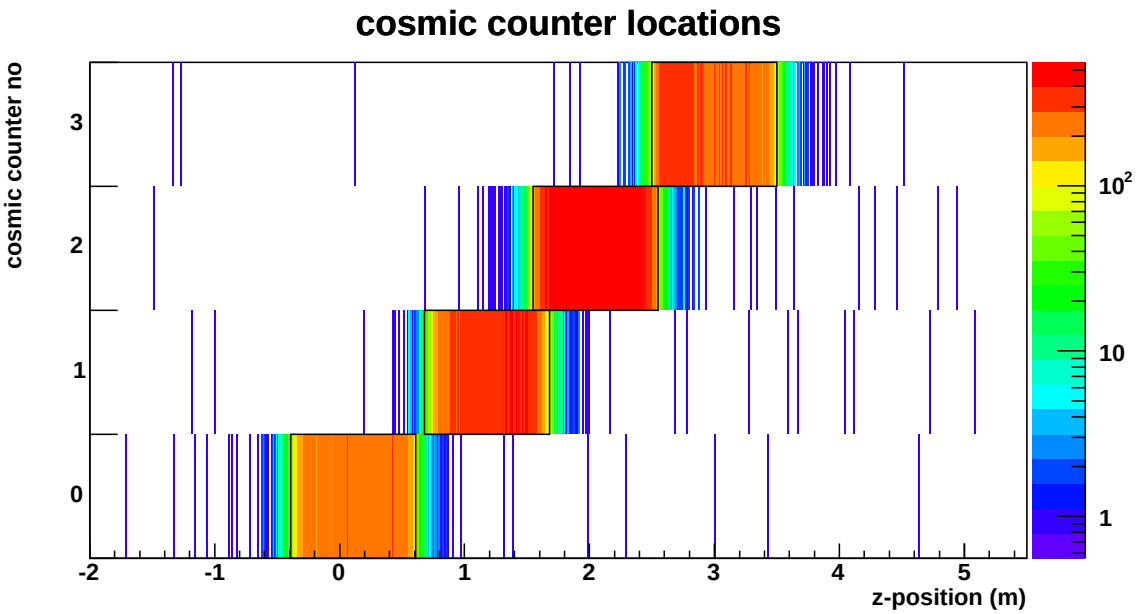

(a) Cosmic counter number of best-matched digit versus extrapolated longitudinal position of track. The cosmic counters are outlined in black.

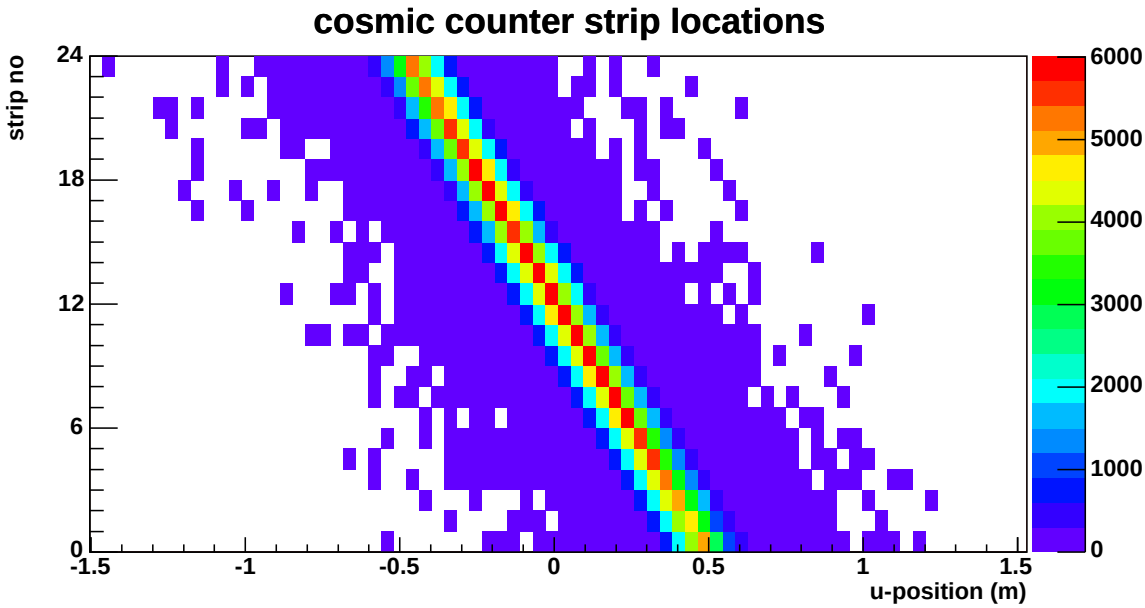

(b) Strip number of best-matched digit versus extrapolated transverse position of track. The position bins are 4.1 cm wide.

Figure 6.1: Location of cosmic counters. Each track was extrapolated to the level of the cosmic counters and the most likely cosmic counter strip hit was determined. Then the digits from the cosmic counters were searched for a match with the most likely strip. There is one entry per track.

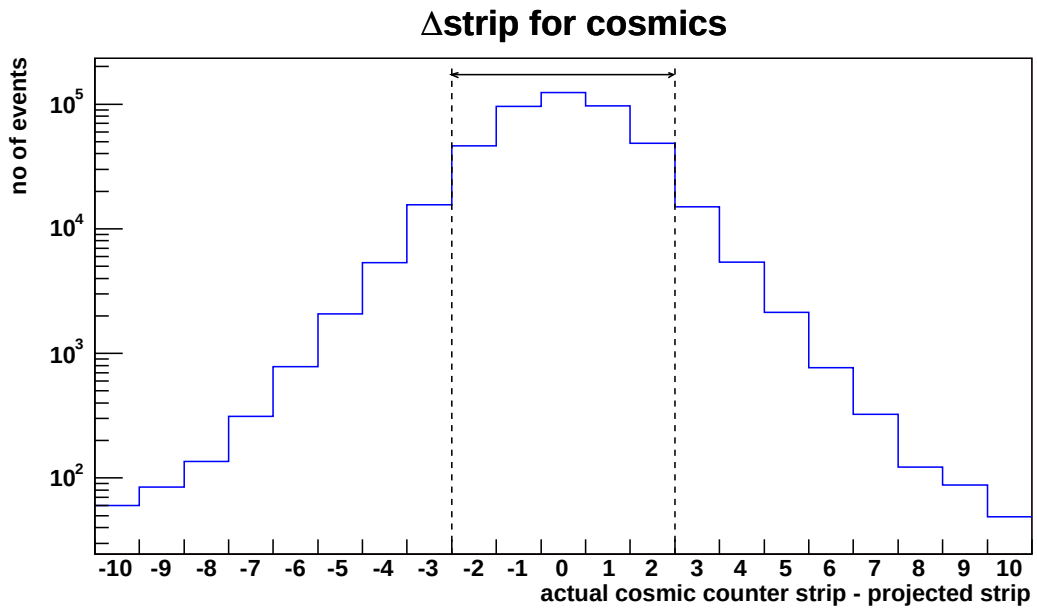

Figure 6.2: Difference in strip number between cosmic counter digits and projected end point of reconstructed track. The dashed lines indicate the cut used in Section 6.3.

cosmic counter #	z-position (m)
0	0.11
1	1.18
2	2.05
3	3.00

Table 6.1: Longitudinal locations of cosmic counters.

again with the highest n_{digit} breaking any remaining ties. Figure 6.2 shows the distribution of Δs. The locations of the counters in the transverse direction were adjusted until the Δs distribution was roughly centered on zero.

Figure 6.3 shows the ADC spectrum from digits that have $c_{\text{digit}} = c_{\text{proj}}$ and $s_{\text{digit}} = s_{\text{proj}}$. The spectrum has a peak for minimum-ionizing particles at $\sim$300 ADC counts and the barest hint of a bump from the single-photoelectron peak at $\sim$100 ADC counts. A cut on the charge is made to select cosmic counter digits resulting from track particles.

With the adjusted locations of the counters, the entire process was repeated with the additional proviso that the counter digit must pass the cut on charge. The process iterated manually until the locations of the cosmic counters, both longitudinally and transversely, and the cut on charge all converged to the nearest cm, mm and 5 ADC counts respectively. Table 6.1 lists the centres of the cosmic counters in the longitudinal direction. The first cosmic counter was protruding from underneath the detector, but it was still covered by the steel plate. The transverse centre was at +1.3 cm, and the cut on charge was at 150 ADC counts.

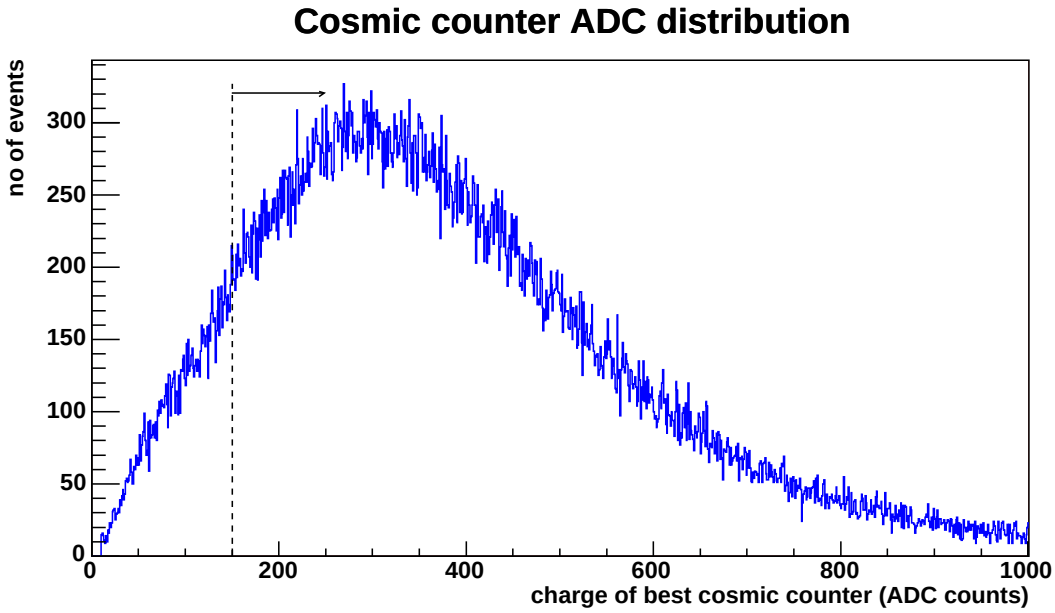

Figure 6.3: ADC spectrum from cosmic counters. Entries are for digits that match both the counter and strip numbers of the projected end point of the reconstructed track. The dashed line indicates the cut at 150 ADC counts.

6.3 Selection of Cosmic Muons

The first step in the calibration is to select likely candidates for high-energy through-going cosmic muons from the tracks reconstructed using the BubbleSpeak package (Section 5.2).

The first criterion is to identify reasonable tracks by requiring at least three planes be hit in each projection, so that the track spans at least six planes in total. This is to make it more likely that the reconstructed track matches the real track closely.

The next criterion is to identify high-energy cosmics by using the cosmic counters. Due to the small size of the Calibration Detector, through-going muons may still be below the minimum ionization threshold as can be seen from the green spectrum of Figure 6.4. Requiring a coincident readout from any of the cosmic counters ensures that the muon passes through the 30-cm steel above the counters; the red spectrum shows that such muons have energy greater than 1 GeV, which is above the required threshold. The cuts used are that there be an aligned cosmic counter digit with charge $\geq$ 150 ADC counts. A digit is considered to be aligned if the track intersects the appropriate cosmic counter or within 10 cm of the ends, and if $|\Delta s| \leq 2$. The alignment cuts are less stringent than in Section 6.2 because of uncertainties in the extrapolated track.

The blue distribution in Figure 6.5 shows the angular distribution of all reconstructed events. As can be seen from the longitudinal distribution, many beam particles ($\cos\theta_z = 1$) have also been reconstructed. Requiring an aligned hit in the cosmic counters leaves a mostly clean cosmic muon sample in green. The remaining upward events are actually downward muons that exit out the front of the detector and are subsequently treated as beam events by the reconstruction package when determining the vertex (recall Section 5.2.3). Since they have travelled through the steel plate before intersecting the protruding portion of the first cosmic counter, they are still valid cosmics and are retained in the analysis.

The remaining cuts are based on the track quality. The third criterion is to select tracks without missing planes, i.e., planes without any strips read out. Figure 6.6 shows the number

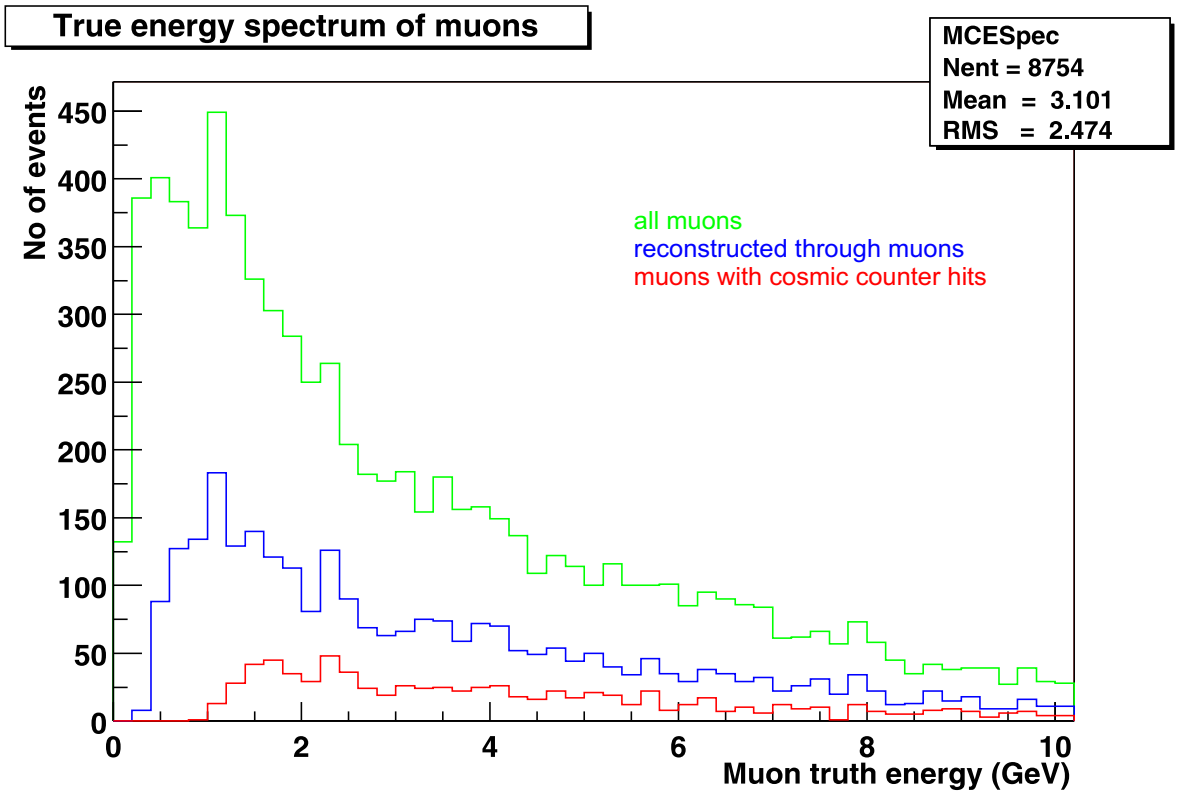

Figure 6.4: Energy spectrum of cosmic muons in the Calibration Detector obtained from a Monte Carlo simulation. The green spectrum is for all cosmic muons that intersect the detector. The blue spectrum represents all through-going muons that are reconstructed by the technique described in Section 5.2. The red spectrum represents those reconstructed through-going muons that coincide with a readout from one of the cosmic counters.

of missing planes per track. Tracks with no missing planes are accepted. Tracks with one missing plane are also accepted because there were some dead PMTs in the detector (see occupancy plots in Figure 6.9), so such planes were more likely to be missed if the track passed close to an end read out by a dead PMT.

The final criterion is to select events that look like tracks rather than showers. Each double-ended strip in the event is designated as good or bad depending on whether or not the reconstructed track intercepts the strip. If the ratio of bad strips to good strips exceeds 0.3 or the number of bad strips exceeds 5, the event is rejected as being too shower-like. The effects of these cuts are shown in Figure 6.7.

The final angular distribution, once all of these cuts have been applied, is shown in red in Figure 6.5. The vertex distribution is shown in Figure 6.8. The transverse distribution is fairly uniform with excesses of events at the sides for muons that enter through the side of the detector. The vertical distribution has an excess for events entering through the top of the detector. It also displays a decrease of events as the entry vertex becomes lower. This is caused by the track length cut, which means that muons which enter at a lower height must be much shallower in order to span the requisite number of planes before they exit the detector. The longitudinal distribution is skewed towards the upstream portion of the detector with excesses at the ends for muons entering through the front or rear of the detector. The deficit of events in the downstream portion is caused by the two upstream counters being read out on one side only, leading to fewer triggers than from the two downstream counters. Muons entering the rear portion tend to hit the two upstream counters, so they are less likely

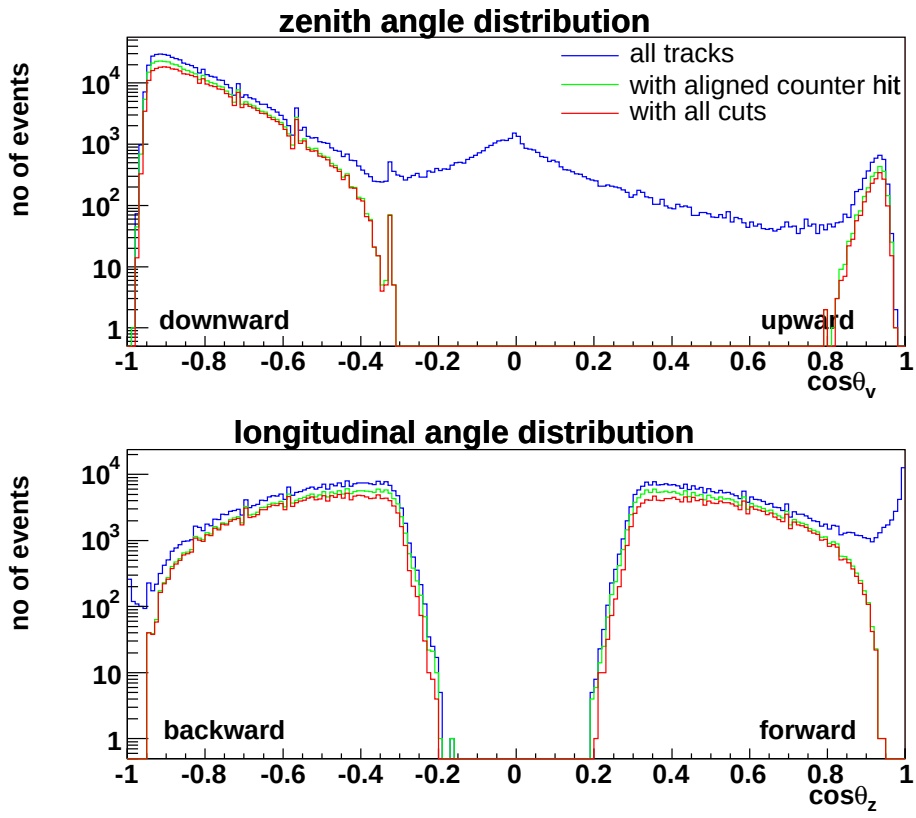

Figure 6.5: Angular distribution of cosmic muons. The distribution in blue shows all reconstructed events. The distribution in green shows cosmic muons with an aligned hit in the cosmic counters. The distribution in red shows the cosmic muons with cuts on the track quality. The upper plot shows the zenith angle distribution ($\cos\theta_v$). The lower plot shows the angular distribution with respect to the beam direction ($\cos\theta_z$). The spikes in the distribution are quantization effects caused by the strips lining up in a perfectly straight line.

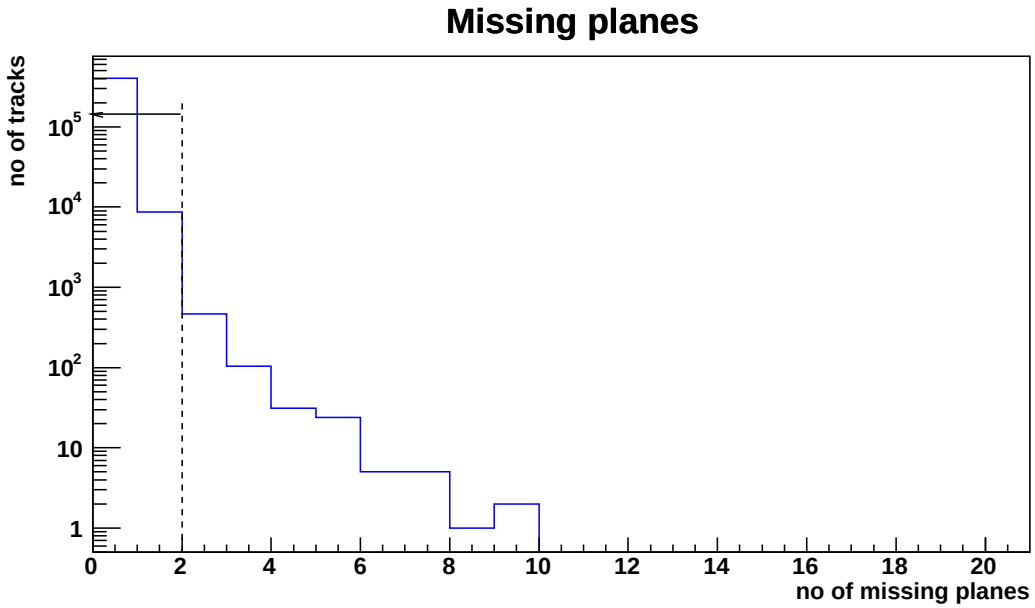

Figure 6.6: Number of missing planes per event. The dashed line indicates the cut on events with two or more missing planes.

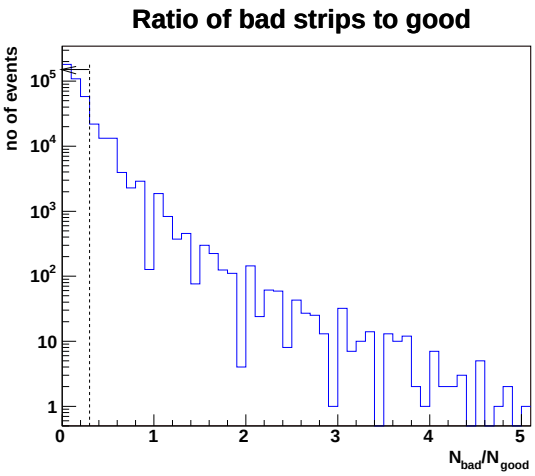

(a) Ratio of bad strips to good strips. The dashed line demarcates the cut at 0.3.

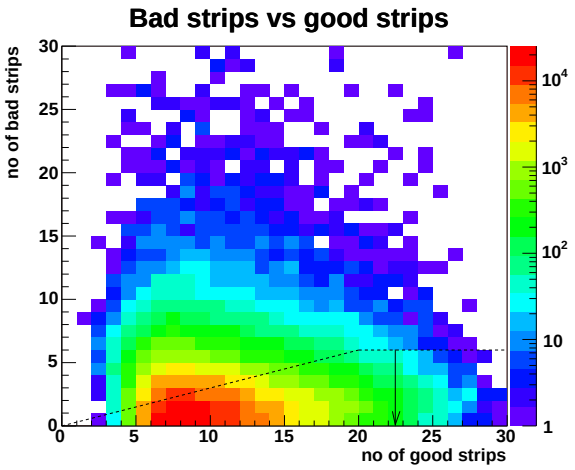

(b) Distribution of number of bad strips versus number of good strips. The dashed lines indicate the cuts on the ratio and on the number of bad strips.

Figure 6.7: Cuts on shower-like events. Double-ended strips are classified as good or bad depending on whether or not the reconstructed track intercepts the strip. Cuts are then made on N_{good} and N_{bad}.

to cause a cosmic counter hit.

Figure 6.9 shows the occupancy plot for cosmic muons coinciding with a trigger in the cosmic counters. The detector is fully illuminated except for the bottom edges of the front and rear faces of the detector. This is caused by the selection cut requiring that at least 3 planes be hit in each view. This is not a problem since the beam events of interest will be at the centre of detector, so calibrating the edges of the detector is not as important. The occupancy plots also show the effects of "dead" PMTs and "dead" electronics channels as regions of low rates. Finally, the effect of the two upstream cosmic counters being read out from one side only is also visible in the occupancy plots as a bias towards the upstream portion of the detector. These two counters will generate fewer triggers than the two downstream counters. The latter two tend to favour events originating in the upstream part since a wider track angle can still hit these counters. This is illustrated in Figure 6.10 for cosmic counter 1.

To summarize, the selection criteria are as follows:

- in each projection, at least three planes must have digits associated with the track;
- there must be a cosmic counter digit of at least 150 ADC counts whose associated strip lies within two strip numbers of the extrapolated end point of the track and which is in a cosmic counter whose centre is within 0.6 m in the longitudinal direction of the extrapolated end point;
- there must be fewer than two missing planes, i.e., planes without any strips read out;
- the ratio of "bad" strips (which are not intersected by the reconstructed track) to "good" strips (which are intersected) must be less than 0.3;
- the number of bad strips must be 5 or less.

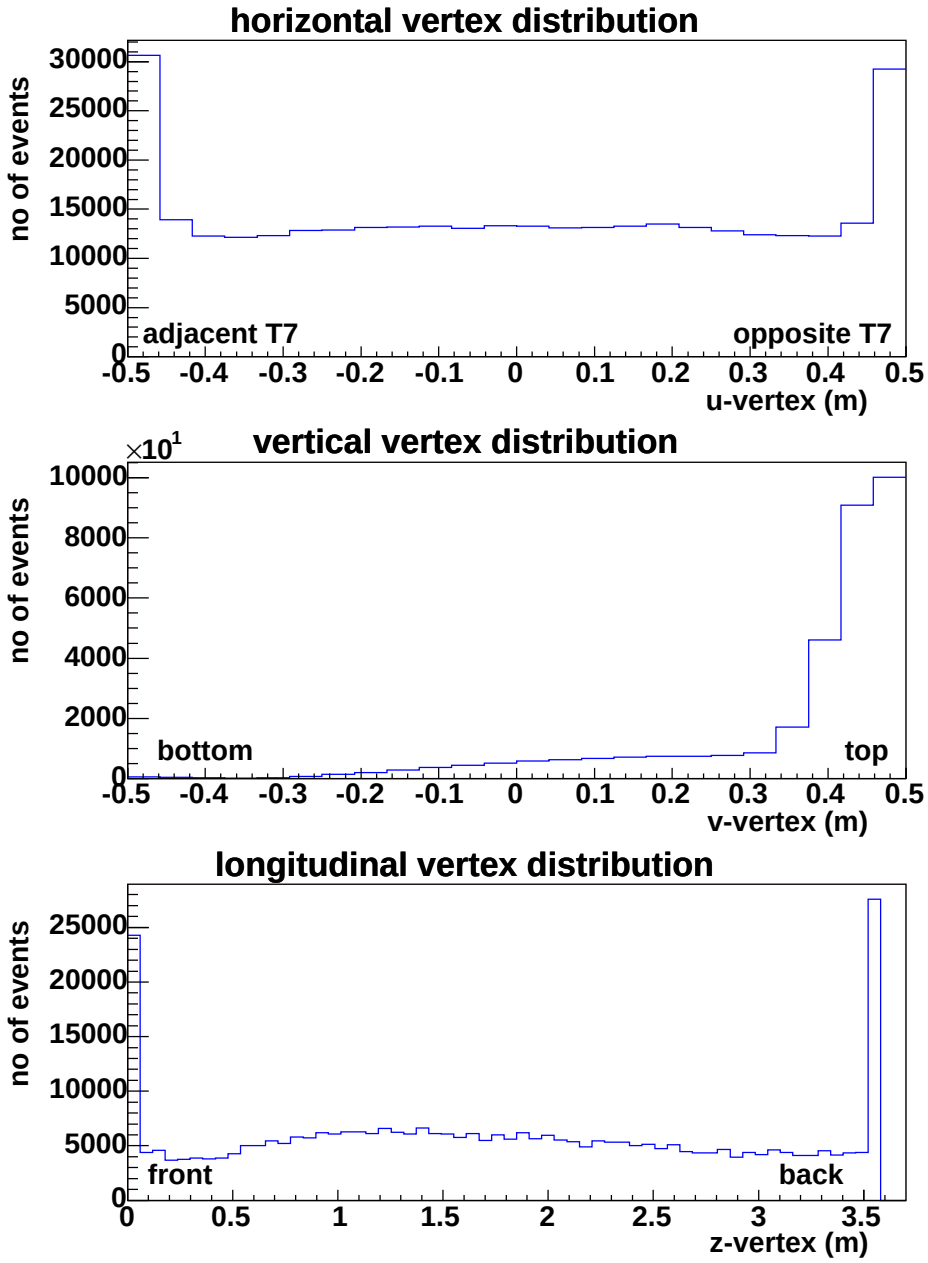

Figure 6.8: Vertex distribution of cosmic muons. The top plot shows the distribution in the transverse direction. The middle plot shows the distribution in the vertical direction. The bottom plot shows the distribution along the beam direction.

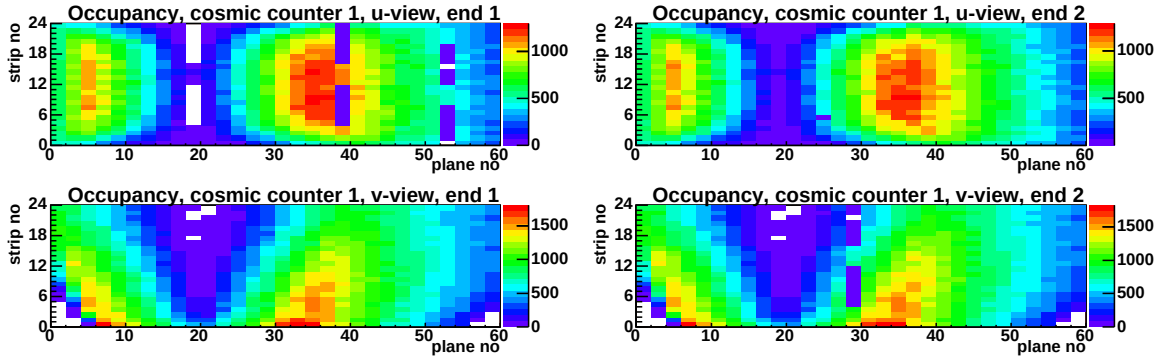

(a) Occupancy plot for muons causing a trigger in cosmic counter 1, which is the second most upstream counter. It is especially noticeable in the v-view how the tracks angle in towards the counter. Events in the downstream portion are favoured because the cosmic counter can be hit by a wider range of angles from downstream events than from upstream events (see Figure 6.10).

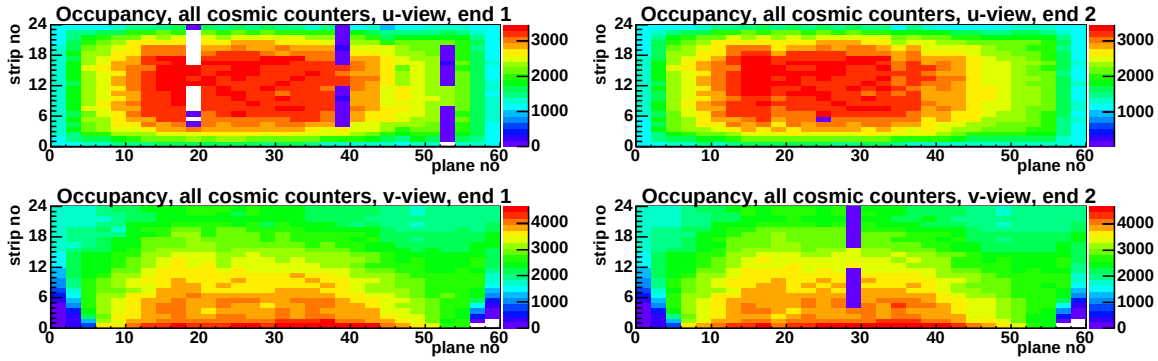

(b) Occupancy plot for muons causing a trigger in any cosmic counter. There is a slight bias towards tracks in the upstream portion of the detector. This is because the two upstream counters are read out on one side only due to a MUX box not functioning, reducing the triggers from those counters. Since those two counters are more likely to trigger on events in the downstream portion of the detector, the rate of events in the downstream part are suppressed.

Figure 6.9: Occupancy plots for cosmic muon events. The top row of plots is for the u-view (horizontal view), and the bottom is for the v-view (vertical). The left- and right-hand columns represent the two ends of each strip. In the plot for u-view, end 1, the blank patches indicate that there are three PMTs (16 strips each) with low trigger rates and therefore considered to be "dead". There is another dead PMT in v-view, end 2. There is also a dead channel in u-view, end 2.

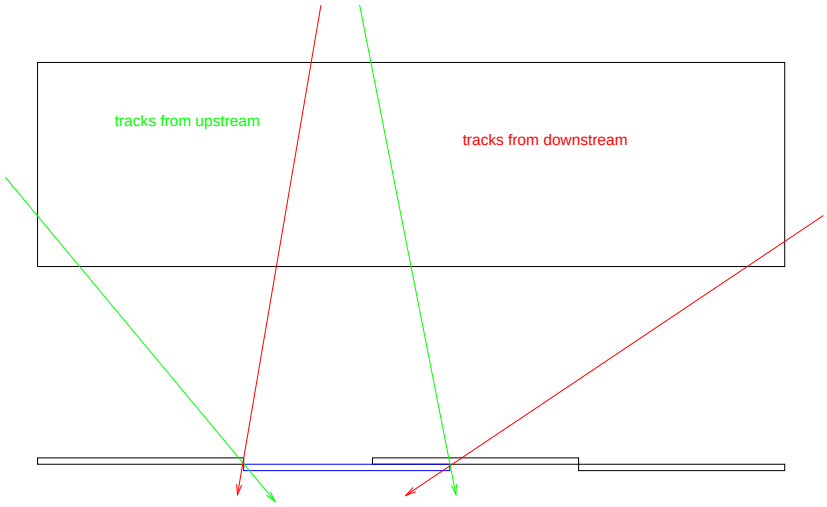

Figure 6.10: Illustration of the acceptance angles for cosmic counter 1. The counter is shown in blue. A wider range of track angles can be accepted for events from downstream (red) than for events from upstream (green).

Once all of these selection criteria have been satisfied, the track is deemed to be a suitable cosmic muon.

6.4 Correction for Angular Dependence

The next step in the calibration is to histogram the charge distribution for each channel (see Figure 6.11 for a typical example of a raw ADC distribution). Ideally, these histograms should be for minimum-ionizing muons that are incident perpendicularly to the strips, i.e., travel along the 1-cm thickness of the strip. Reality is that cosmics impinge at many different angles to the strip. They thus travel a different amount through the strip and produce a proportionately different amount of scintillation light. A pathlength correction needs to be applied to reduce the angular dependence of the muon response.

Another effect arises when using cosmic muons because the strips are oriented horizontally and vertically. u-view strips are oriented vertically (see Figure 5.2), so steep cosmic muons will tend to have longer pathlengths inside these strips compared to v-view strips (see Figure 6.12(a)). This results in an asymmetry between the responses of the two views. It is important to correct for this before calculating calibration constants because beam particles have roughly the same pathlengths in the strips regardless of view (see Figure 6.12(b)), so they do not have the same asymmetry in response. Again, a pathlength correction is required.

The simplest correction to make would be to divide the charge seen in a strip for a particular muon by the pathlength of that muon through the strip. However, due to the imperfect reconstruction of the track direction and location, this can lead to "corner clippers", muons which reconstruct as clipping a corner of a strip and thus have a short pathlength, but in reality travel through the length of the strip and thus produce a large energy deposit. Thus this large charge divided by the abnormally (and incorrectly) small pathlength can lead to a disproportionately huge corrected charge. The reverse situation can also happen, leading to a disproportionately tiny corrected charge. Thus this correction can work to distort the distribution significantly.

The approach adopted is to use an average pathlength correction illustrated for a v-view

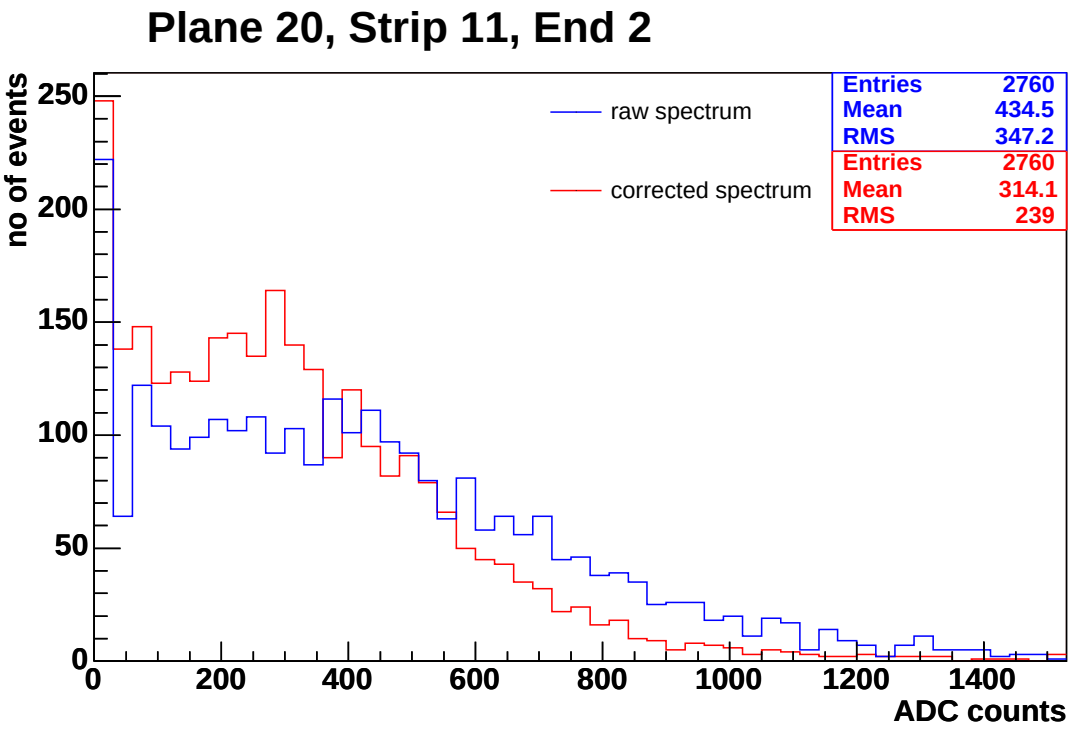

Figure 6.11: Example raw (blue) and calibrated (red) ADC spectra from one end of a strip near the centre of the detector. The corrections for angular dependence (Section 6.4) and variation along strip length (Section 6.5) are included in the calibrated spectrum.

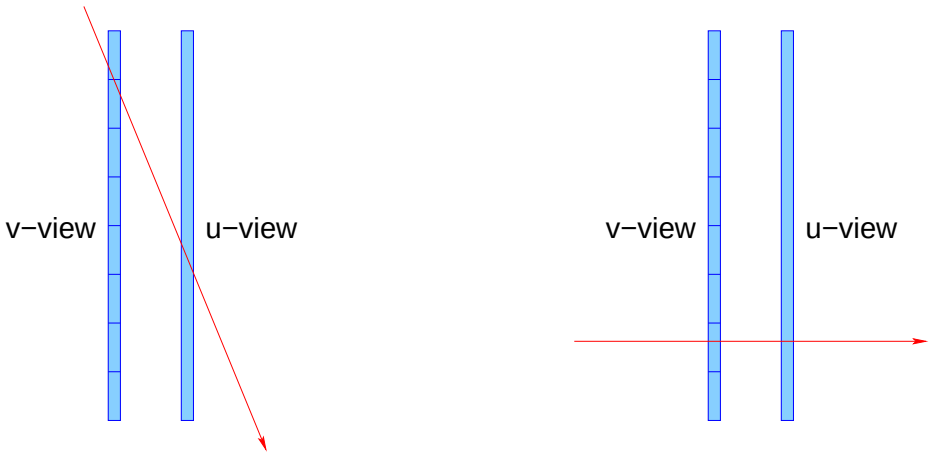

(a) Steep cosmic muon passing through strips. The pathlength in the v-view strips is shorter than in the u-view strips.

(b) Beam particle passing through strips. The pathlength is the same for both views.

Figure 6.12: Illustration of pathlengths of particles in strips.

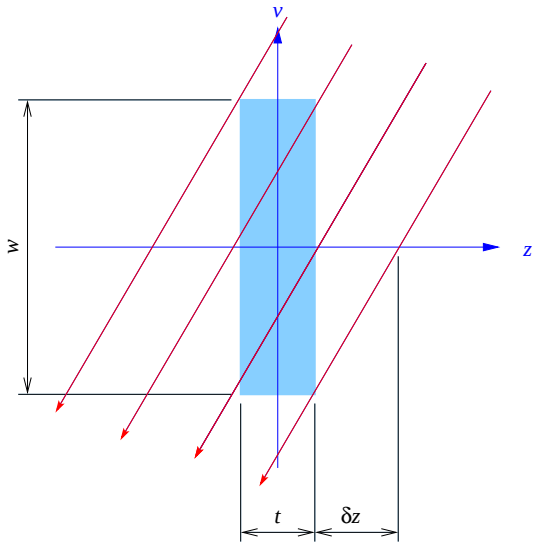

Figure 6.13: Average pathlength correction. For a track at a given angle, the average pathlength projected in transverse dimensions is calculated by integrating over possible intersections. This gives the average transverse pathlength in terms of the strip width w, strip thickness t, $\cos\theta_v$ and $\cos\theta_z$. The example shown is for a v-view strip.

strip in Figure 6.13. For a fixed incident track direction, the average is taken over all possible trajectories, projected in transverse dimensions, which intersect the strip. The average transverse pathlength $\langle s_{transverse} \rangle$ is then given by:

$$\langle s_{transverse} \rangle = \frac{\int_{-\frac{t}{2}-\delta z}^{\frac{t}{2}+\delta z} s_{transverse}(z)\, dz}{\int_{-\frac{t}{2}-\delta z}^{\frac{t}{2}+\delta z} dz}\ , \tag{6.4}$$

which evaluates to

$$\langle s_{transverse} \rangle = \frac{wt}{w|\cos\theta_z| + t|\cos\theta_v|}(\cos^2\theta_z + \cos^2\theta_v)^{\frac{1}{2}}\ , \tag{6.5}$$

where w = strip width and t = strip thickness. The strip is assumed to have infinite length, so the average pathlength can then be calculated from Equation 6.5 and the reconstructed longitudinal pathlength as:

$$\begin{aligned} \langle s \rangle^2 &= \langle s_{transverse} \rangle^2 + \langle s_u \rangle^2 \\ &= \langle s \rangle^2(\cos^2\theta_z + \cos^2\theta_v) + \langle s \rangle^2 \cos^2\theta_u \\ \therefore \langle s \rangle &= \frac{wt}{w|\cos\theta_z| + t|\cos\theta_v|} \quad \text{from Equation 6.5.} \end{aligned} \tag{6.6}$$

The idea is then that, while this will not produce the "correct" corrected value for that particular track, averaged over all possible tracks of that given angle the "incorrectness" will average itself out.

As can be seen from Figure 6.14, the average pathlength correction reduces the angular dependence of the muon response for both the clear and green fibre ends. The correction also reduces the asymmetry in the response between the two views.

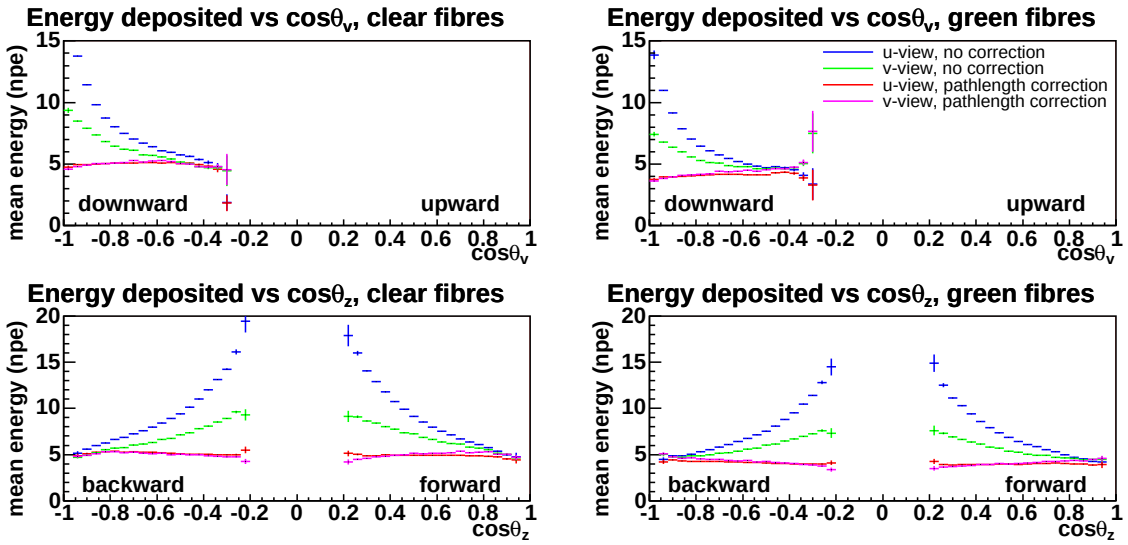

Figure 6.14: Effect of average pathlength correction. The charge per strip end is shown as a function of zenith angle ($\cos\theta_v$, upper plots) and angle w.r.t. beam direction ($\cos\theta_z$, lower plots). The plots on the left are for the strip ends read out by clear fibre, and on the right are for green fibre. The blue and green show the charge without a pathlength correction and clearly depends on the track angle. The red and magenta show the charge with the average pathlength correction applied. Its angular dependence has been greatly reduced. The averages include zeroes when there is a digit on the other end of the strip. The attenuation correction from Section 6.5 has been applied to all entries.

6.5 Correction for Variation Along Scintillator Length

6.5.1 Observations from Data

Another effect that needs to be corrected for is the attenuation along the length of the scintillator (see Figure 6.15), caused primarily by absorption of photons in the WLS fibre. By using the other projection, the intersection position of the track along the strip length can be found. This allows a plot to be made of the variation of the muon response along the strip length. There is clearly attenuation along the strip length. The attenuation is not a simple exponential; rather, it is expected to be the sum of two exponentials, the long attenuation length (typically $\sim$10 m) resulting from absorption in the polystyrene core of the WLS fibre, the short (typically $\sim$0.8 m) from self-absorption in the fluor dopant [108]. For photons travelling a short distance in the WLS fibre, the amount of absorption is dominated by the steep initial drop. This is the case on the clear fibre side (recall Section 4.1) where the change from one end to the other amounts to a change from 0 m to 1 m of WLS fibre (plus pigtails). For photons travelling a long distance, the absorption is governed by a more gradual tailing off, which is what is seen on the green fibre side where the change is from 4 m to 5 m. Therefore, the absorption is greater for the readout that is coupled through clear fibre rather than WLS fibre. Due to resolution effects, the total attenuation can be approximated by a straight line in the central portion of the strip.

There is also a drop-off at the ends of the strip. This is due to the strip ends being unpainted, leading to loss of scintillation light out of the ends. These effects were studied in a Monte Carlo simulation, which is described in the next section.

There are also jumps in alternate bins in the v-view. These are an artifact of the 2.05-cm

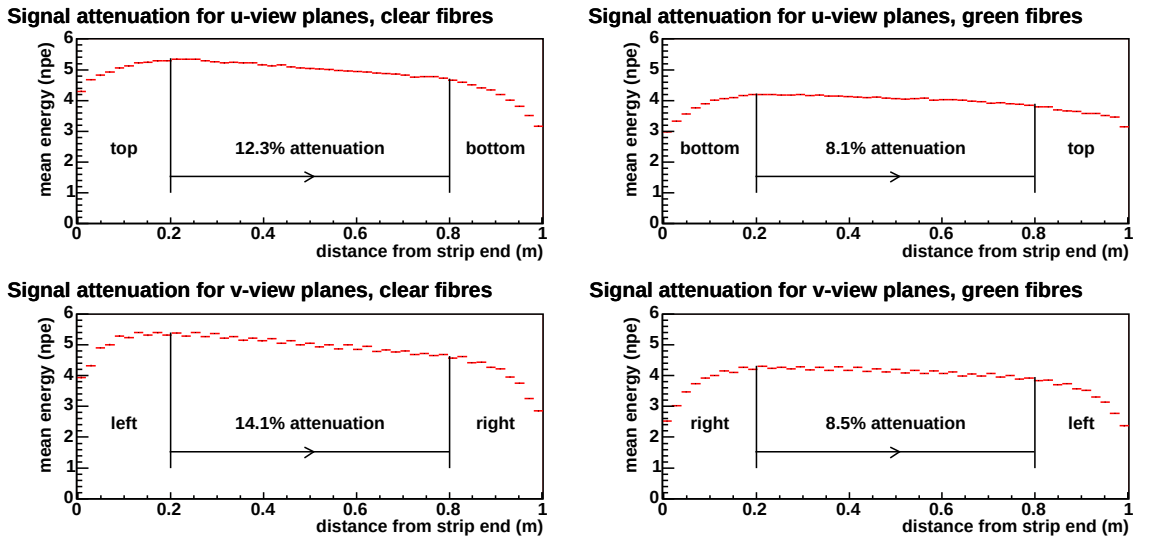

Figure 6.15: Variation of light output along strip length. The attenuation is greater for the readout end that is coupled through clear fibre rather than WLS fibre. This is because the attenuation follows a double exponential.

bin size, half the strip width; particles passing near the centre of the strip will have more scintillation light trapped by the WLS fibre, resulting in those bins having higher output. The neighbouring bins are near the edges of the strip so have lower output. This effect is not evident in the u-view because the angles seen in that view are less prone to quantization effects.

6.5.2 Simulation of Light-Trapping in MINOS Scintillator

The Monte Carlo simulation of the MINOS scintillator is written in Fortran. It was originally developed by Keith Ruddick for liquid scintillator [109] and has been adapted for use with plastic scintillator by this author. It simulates the scintillator response to minimum-ionizing muons.

The MINOS scintillator consists of a polystyrene base doped with 1.0% PPO as the primary fluor and 0.030% POPOP as the secondary fluor [75]. Minimum-ionizing muons impinge on the scintillator at various angles, ionizing the polystyrene. The ionization energy is transferred to the PPO by a resonant dipole-dipole interaction known as the Förster energy transfer. The PPO then emits UV (ultraviolet) photons. The POPOP absorbs the UV photons and emits blue photons [9] with a mean wavelength of 460 nm. The blue photons are emitted isotropically along the muon tracks and propagated through the scintillator until they are absorbed by the K27 dye in the WLS fibre [77]. The dye then emits green photons (mean wavelength 530 nm) that are then propagated through the fibre by total internal reflection until they reach the photodetector. The photodetector then converts the photons into photoelectrons. The number of photoelectrons produced gives a measure of the light output. The photodetector thus measured the light output in number of photoelectrons (npe).

6.5.2.1 Geometry

The strip dimensions used in the simulation are the same as those in the Calibration Detector: 1 cm $\times$ 4.1 cm $\times$ 1 m. A WLS fibre of 1.2 mm diameter is embedded inside the scintillator

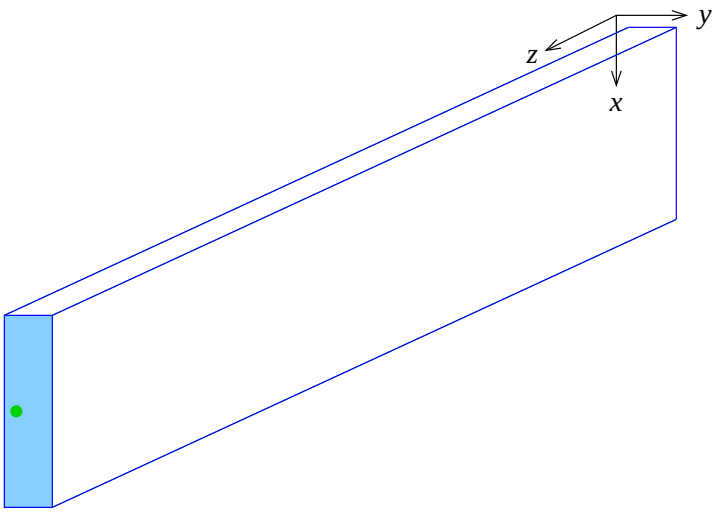

Figure 6.16: Coordinate system used for light-trapping simulation. The x-axis measures along the strip width, the y-axis along the strip thickness, and the z-axis along the strip length. To simulate u-view strips, the x-axis coincides with the u-axis, and similarly for v-view strips.

with its axial centre at a depth of 1.4 mm. Pigtails, which are the extra lengths of WLS fibres in the manifolds (see Figure 3.9), of 38 or 110 cm can be included to simulate the shortest and longest pigtails used in CalDet. The additional 4 m of WLS fibre or 6 m of clear fibre can also be included to simulate the added fibre used in CalDet.

The coordinate system used is shown in Figure 6.16. The transformation from (x, y, z) to (u, v, z) differs for each view:

$$u\text{-view:} \qquad (x, y, z) \rightarrow (u, z, -v) \tag{6.7}$$

$$v\text{-view:} \qquad (x, y, z) \rightarrow (v, z, u)\ . \tag{6.8}$$

The muons are incident on the strip with a zenith angle distribution taken from CalDet data (Figure 6.17(a)). Each entry is weighted by the number of strips intersected by the reconstructed track. This is done because certain angles may intersect more strips, so conversely a strip is more likely to be intersected by tracks at those angles. The two projections are also treated separately. The azimuthal angle distribution is also taken from CalDet data (Figure 6.17(b)). The entry vertex along the strip length is smeared by one strip width to simulate the potential misreconstruction in the other projection.

6.5.2.2 Production and Propagation of Blue Photons

The energy deposited by the muon is selected from a Landau distribution with a mean of 1.98 MeV/cm times the pathlength of the muon in the strip. One blue photon is produced for every 100 eV of energy deposited. The photons are randomly uniformly distributed along the length of the track. The fibre is treated as a non-scintillator, so any photons produced inside it were discarded. The wavelengths of the photons are sampled from the spectrum shown in Figure 3.8(a). The photons are emitted isotropically.

The propagation of blue photons is shown in Figure 6.18. Each photon is propagated until it hits a wall of the strip, it hits the fibre, or it is absorbed by the scintillator. The transmission probability of the scintillator is taken from the spectrum shown in Figure 6.19. If the photon hits an unpainted end of the strip, it is assumed to have escaped and thus discarded. If the

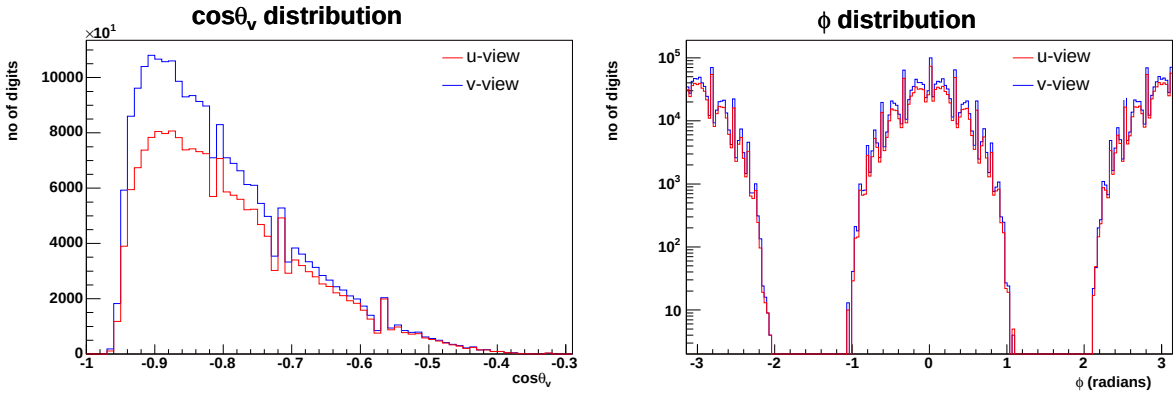

(a) Zenith angle distribution

(b) Azimuthal angle distribution

Figure 6.17: Angular distributions of cosmic muons per strip. For each cosmic muon, its entry in the distribution was weighted by the number of strips intersected by the reconstructed track.

photon hits a painted wall, it could be reflected with a probability given by Figure 6.20 or absorbed otherwise. If reflected, it is assumed to reflect diffusely due to the rough surface and thus emerges isotropically from the wall to continue propagating through the scintillator. If the photon hits the fibre, it could be reflected from the fibre surface and again continue to propagate through the scintillator. These reflections are governed by Snell's law. If the photon enters the fibre, it could be transmitted through the fibre and continue its propagation. Otherwise, the photon is absorbed in the fibre. The absorption length in the WLS fibre λ_{WLS} consists of a constant bulk component λ_{bulk} and a wavelength-dependent fluor component λ_{fluor}:

$$\frac{1}{\lambda_{WLS}} = \frac{1}{\lambda_{bulk}} + \frac{1}{\lambda_{fluor}} \tag{6.9}$$

where $\lambda_{bulk} = 875$ cm and λ_{fluor} is taken from the distribution shown in Figure 6.21.

6.5.2.3 Production and Propagation of Green Photons

A blue photon that is absorbed in the fibre is converted into a green photon with a wavelength sampled from the spectrum shown in Figure 3.8(b) and emitted isotropically from the absorption point. The green photon is then propagated towards the photodetector. The propagation of green photons is shown in Figure 6.22. If the photon is not totally internally reflected from the walls of fibre, it is assumed to escape from the fibre at some point before reaching the photodetector, so it would emerge into and be absorbed in the scintillator. The photon could also be absorbed in the fibre en route to the photodetector. The absorption length in the WLS fibre is as described in Section 6.5.2.2. The absorption length in the clear fibre is constant at 1175 cm.

Green photons that reached the photodetector were counted. The quantum efficiency of the photodetector was taken from Figure 6.23.

6.5.2.4 Comparison with Data

Several parameters were allowed to vary in order to study their effects in isolation. The chief findings are that:

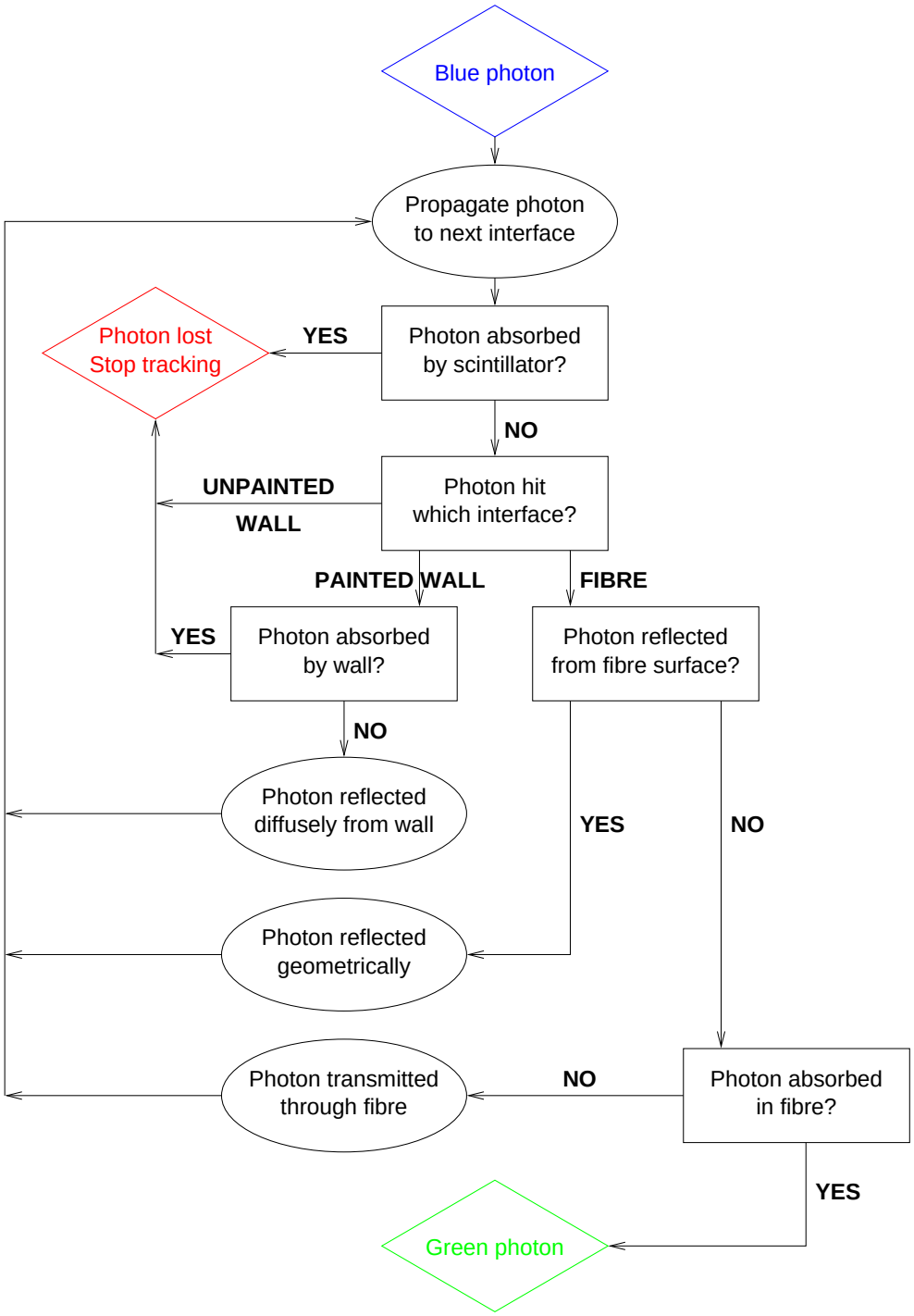

Figure 6.18: Flow chart of the propagation of blue photons. Each photon is propagated until it hits a strip wall or the fibre with the possibility of it being absorbed en route by the scintillator. If the photon hits an unpainted end of the strip, it escapes out the end and is thus lost. If the photon hits a painted wall, it could be absorbed there. If not absorbed, it reflects diffusely and continues propagating. If the photon hits the fibre, it could reflect from the fibre and continue propagating through the scintillator. It could also be transmitted through the fibre and emerge from the other side to continue propagating. Otherwise, it is absorbed in the fibre to produce a green photon.

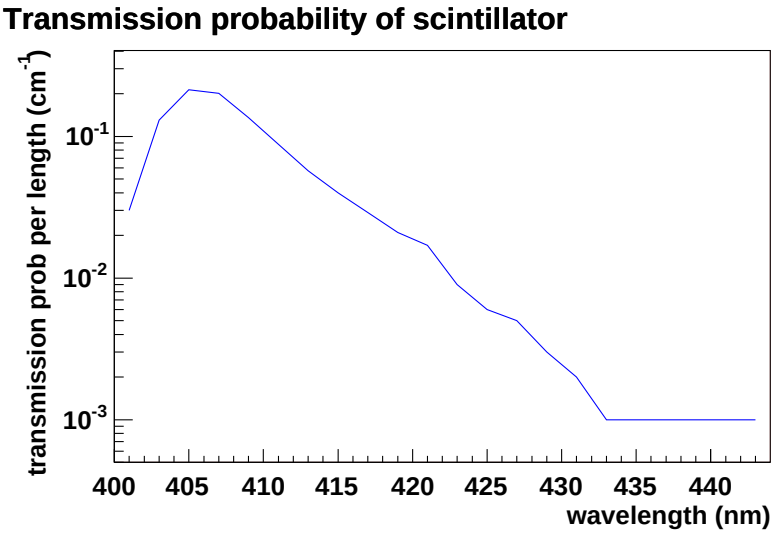

Figure 6.19: Transmission probability of scintillator used in the simulation [108].

view	fibre	attenuation [m^{-1}]	
		data	MC
u	clear	.218	.251
u	green	.141	.176
v	clear	.253	.235
v	green	.148	.151

Table 6.2: Comparison of attenuation factors between data and simulation for the two views and readout fibres.

- increasing the bulk absorption in the WLS fibre increases the light attenuation along the strip length;
- increasing the bulk absorption in the scintillator confines the drop-offs due to the unpainted walls to regions closer to the strip ends since photons are less likely to survive as far as the ends.

The bulk absorption lengths in the fibre and the scintillator were adjusted to match the results from data, as can be seen in Figure 6.24. The slight discrepancies in the final bins are attributed to the simulation ignoring the slight possibility of photons reflecting from the unpainted walls of the strip back into the scintillator, which would result in a slight increase in the light yield at the ends.

With the extra pigtails and connection fibre included, good agreement was generally found between data and Monte Carlo. This means that the attenuation along the strip length is understood and can be approximated as linear when the ends are excluded.

From Figure 6.24, the dropoffs due to light escaping from the unpainted ends appear to be confined to within 20 cm of each end. To confirm this, the simulation was run with 8-m long strips. To simplify things, the muons impinged perpendicularly and uniformly over the front ($y = 0$ in Figure 6.16) face, i.e., as if it were a beam particle. The results shown in Figure 6.25 confirm that the dropoffs are confined to the outer 20 cm even for the longer strips found in the Far Detector. The attenuation also exhibits the double exponential nature

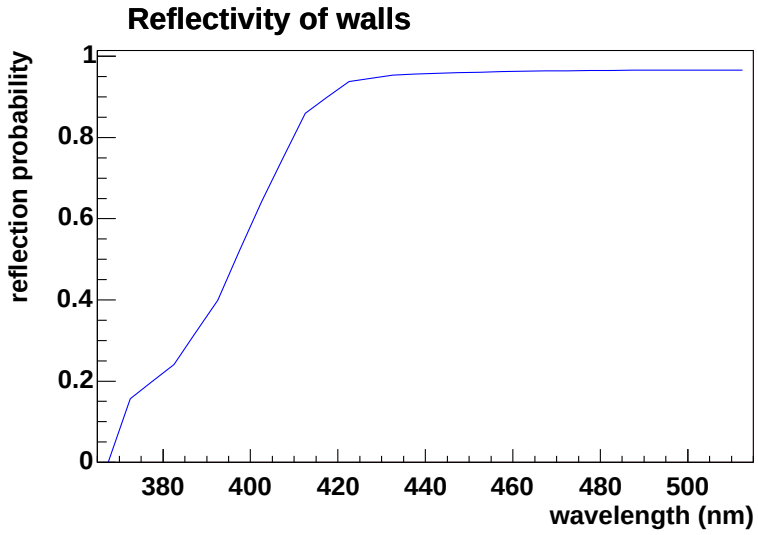

Figure 6.20: Reflectivity of painted scintillator walls used in the simulation [108].

described in [108].

6.5.3 Correction Along Strip Length

As seen in the previous sections, the charge output varies with the position along the strip length of the intersection of the muon. To eliminate this dependence from the strip-to-strip calibration, a correction is applied. The end effects complicate the correction. However, we are primarily interested in calibrating the central portions of the strips, as test beam particles will impinge on the centre of CalDet. Also, in the main detectors the strips will be much longer, so the drop-off regions will form a smaller percentage of the total length and will certainly be excluded by any cuts on fiducial volume. So any digits that result from intersections within 20 cm of either end of a strip are omitted from the histograms. Any digits lying in the central 60 cm of the strip are corrected by a correction factor and included in the histograms.

The correction factor is calculated to correct the response to be equivalent to the centre of the detector where test beam particles will impinge on CalDet. A straight line is fitted to the central 60 cm of the attenuation curve. The line is then scaled so that it is unity at the centre of the strip. Then, for each digit its correction factor is found from the scaled line and the charge is divided by the correction factor A:

$$A = 1 - m(d - 0.5\ \mathrm{m})\ , \tag{6.10}$$

where m is the slope of the fitted line and d is the distance from the readout end. The values of m for the data shown in this section are shown in Table 6.2.

6.6 Calculation of Calibration Constants

By applying the corrections described in Sections 6.4 and 6.5 to each digit associated with a cosmic muon, calibrated charge spectra (see red distribution in Figure 6.11) are obtained for each strip end. Nominally, each entry is proportional to the energy deposited by a high-

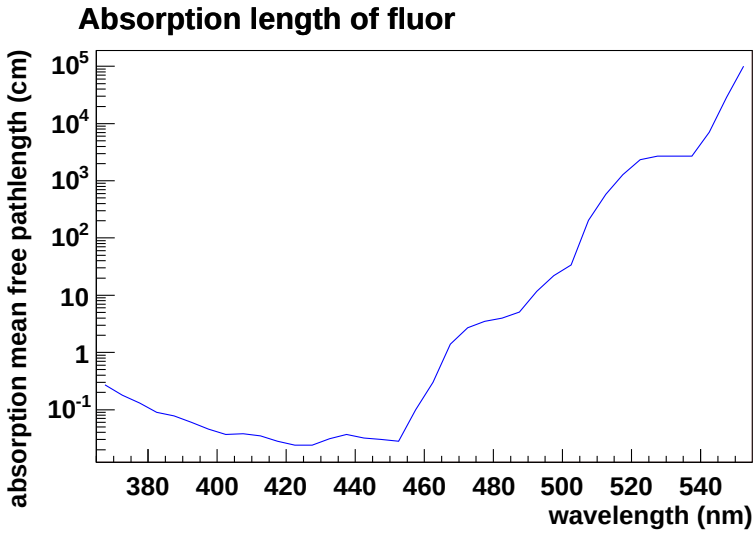

Figure 6.21: Absorption length of the fluor component in the WLS fibre [110].

energy muon traversing the strip perpendicularly at its centre. The means of the calibrated spectra are used to calculate the calibration constants $C_i^{\text{scint}'}$ (from Equation 6.1) which convert the channel response from number of photoelectrons (npe) to Signal Corrected (SigCorr):

$$C_i^{\text{scint}'} = \frac{1}{2\,\overline{p_i^{\text{corr}}}}\ , \tag{6.11}$$

where $\overline{p_i^{\text{corr}}}$ is the mean in npe of the calibrated spectrum for channel i. The factor of $\frac{1}{2}$ is included so that a muon produces one SigCorr per strip (2 strip ends per strip $\times\ \frac{1}{2}$ SigCorr per strip end). One SigCorr is approximately one minimum-ionizing particle (MIP) because nearly minimum-ionizing cosmic muons were used to fill the histograms.

Figure 6.26 summarizes the calibration constants obtained using 348 784 cosmic muons from a 13.2-hour run. Figure 6.26(a) is a map of $\overline{p_i^{\text{corr}}}$ for each channel, and Figure 6.26(b) shows the distribution of $\overline{p_i^{\text{corr}}}$. The channels with high values are artifacts of low PMT gains; the map of ADC/SigCorr values in Figure 6.26(c) shows that these channels have typical responses in ADC counts.

The relative error of the calibration constant $\frac{\delta C}{C}$ is calculated for each channel as

$$\frac{\delta C}{C} = \frac{\sigma_{p^{\text{corr}}}}{\overline{p^{\text{corr}}}\sqrt{N}}\ , \tag{6.12}$$

where $\sigma_{p^{\text{corr}}}$ is the RMS in npe of the calibrated spectrum, and N is the number of entries in the spectrum. Figure 6.27(a) maps the relative errors of the npe/SigCorr values in Figure 6.26(a). The distribution of the relative errors (see Figure 6.27(b)) shows that most of the channels have been calibrated to less than 3% error. Figure 6.27(c) shows that channels with high relative error are due to low statistics.

6.6.1 Consistency Check Within a Run

As a consistency check, the data was divided into two interleaved subsets corresponding to even- and odd-numbered events, the calibration constants calculated for both subsets, and

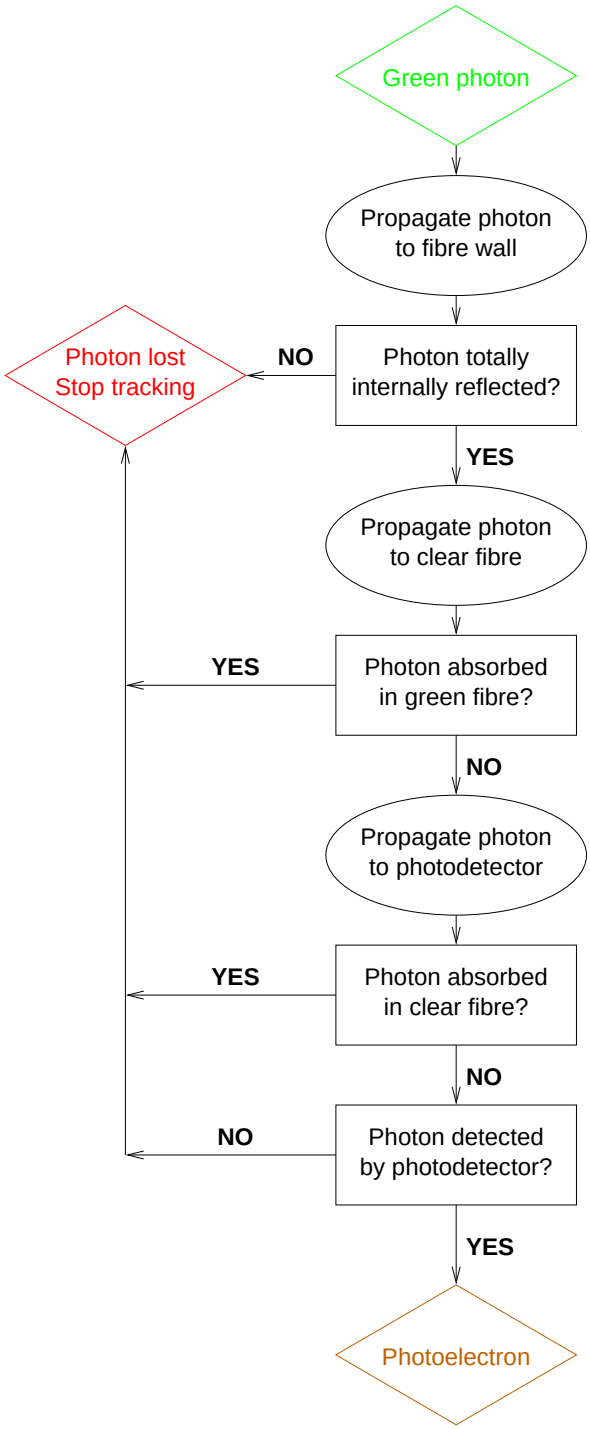

Figure 6.22: Flow chart of the propagation of green photons. Each photon is propagated to the fibre wall. If the photon is not totally internally reflected there, it is assumed to escape from the fibre at some point before reaching the photodetector, so it will be lost in the scintillator. Otherwise, the photon is propagated to the photodetector with the possibility of it being absorbed en route by either the WLS fibre or the clear fibre. Once at the photodetector, the photon may be converted into a photoelectron.

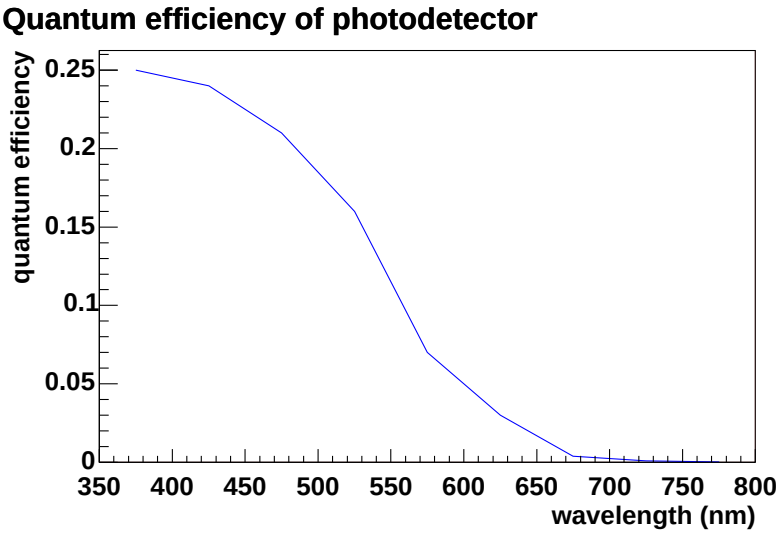

Figure 6.23: Quantum efficiency of the photodetector used in the simulation [111].

the constants from the two subsets compared with each other. The subsets were chosen to be interleaved so that any time variations in the data would appear in both subsets and therefore cancel out in the comparison.

The relative shift in the histogram means between the two subsets was calculated as

$$\frac{\Delta p}{\overline{p}} = \frac{\overline{p_{\text{odd}}} - \overline{p_{\text{even}}}}{\frac{1}{2}\left(\overline{p_{\text{odd}}} + \overline{p_{\text{even}}}\right)} , \tag{6.13}$$

where $\overline{p_{\text{odd}}}$ and $\overline{p_{\text{even}}}$ were the means of the odd and even subsets respectively. Figure 6.28(a) shows that there is no systematic shift in the means.

The error estimates were checked by calculating

$$A = \frac{\overline{p_{\text{odd}}} - \overline{p_{\text{even}}}}{\sqrt{\sigma^2_{p_{\text{odd}}} + \sigma^2_{p_{\text{even}}}}} , \tag{6.14}$$

where $\sigma_{p_{\text{odd}}}$ and $\sigma_{p_{\text{even}}}$ were the standard errors in the odd and even subsets respectively. The distribution of A was expected to have a mean of 0 and an RMS of 1 if the calibration constants were consistent between the two subsets and the error estimates were accurate. Figure 6.28(b) shows that the mean was consistent with zero (0.000 ± 0.018), but the RMS was 0.935 ± 0.014, which is less than unity. This indicates that the errors on the histogram means were overestimated. This occurred because the charge histograms were not Gaussian (recall Figure 6.11), so the tails of the histograms increased the RMS and therefore the error estimates. However, this is not a significant effect, so the error estimates are correct to first order.

6.6.2 Comparison Between Two Runs

The same comparisons were performed between two data runs separated by three days. The two runs were treated as different sets and were not interleaved. The results, shown in Figure 6.29, indicate that while there is no appreciable systematic shift between runs (mean shift $= -0.0007 \pm 0.0007$ from Figure 6.29(a)), the histogram means are not fully

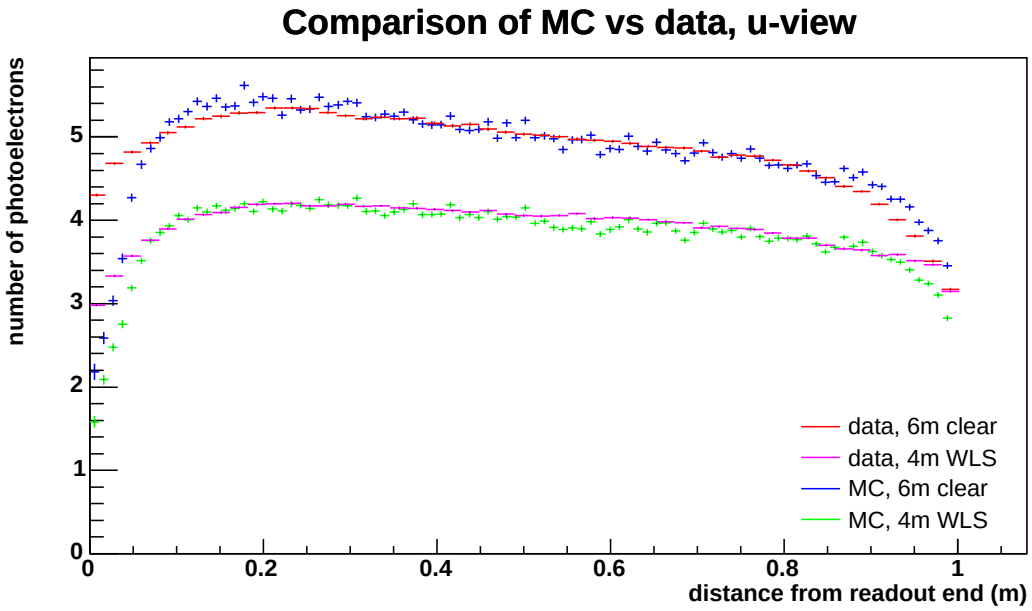

(a) Comparison for u-view strips.

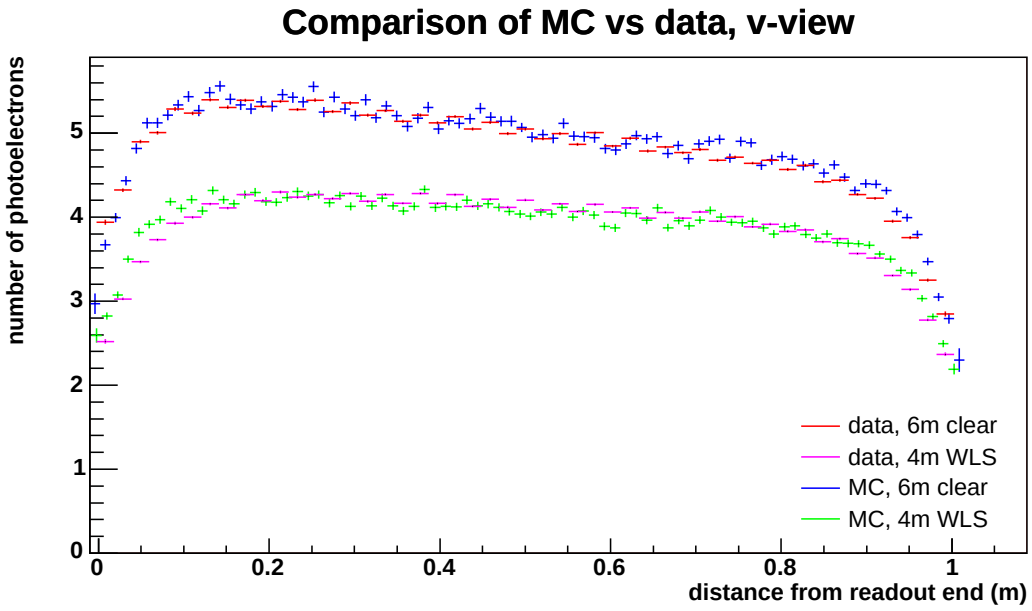

(b) Comparison for v-view strips.

Figure 6.24: Comparison of light attenuation between data and simulation. Separate comparisons are shown for clear and WLS fibre sides for each view.

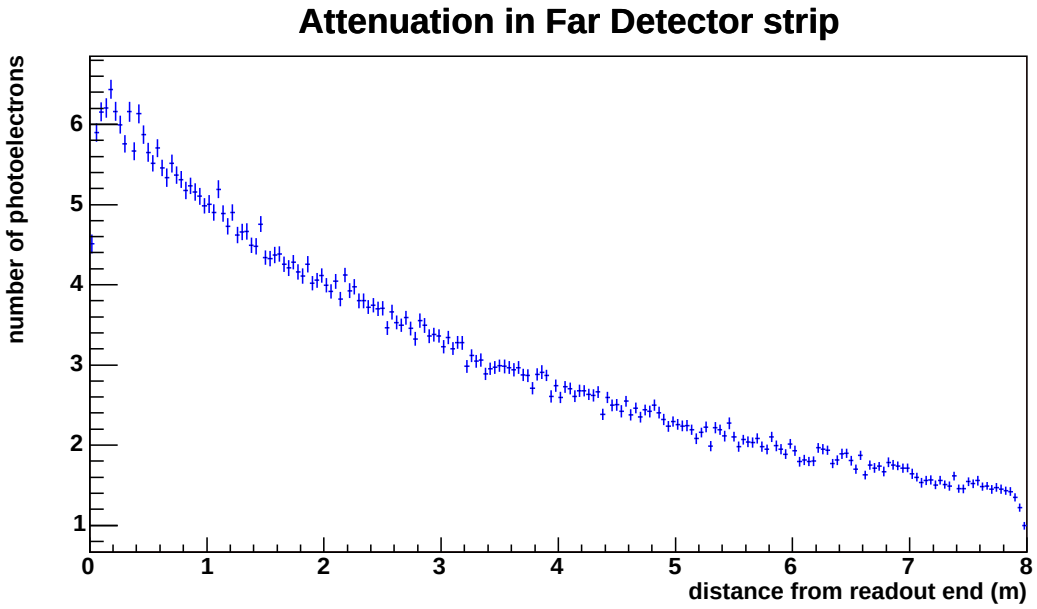

Figure 6.25: Simulated attenuation along strip length of Far Detector strips. There are dropoffs in the final 20 cm of each end. The attenuation in the central portion follows a double exponential.

consistent (RMS of $A = 1.064 \pm 0.015$ from Figure 6.29(b)). This is not surprising because the two runs would have experienced different time variations. These fluctuations would be eliminated by the light injection calibration. Nevertheless, the constants are consistent to first order.

6.7 Application of Strip-to-Strip Calibration

The strip-to-strip calibration was applied to a sample of 3.5-GeV/c particles taken in 2001 (Period I) using the T11 test beam. As mentioned in Section 4.3, the data from this period was plagued by problems due to electronics deadtimes. Reading out a VA chip, the basis of the Far Detector electronics, results in a deadtime of 5 μs. Since each VMM reads out 6 VA chips sequentially, this results in a total effective deadtime per chip of 30 μs. Should two events be separated by less than 30 μs, dead chips would result in "holes" in the detector. To reduce the problems from these holes, the analysis in this section required events to be separated by 40 μs.

6.7.1 Electrons

Electrons were selected using the Čerenkov counter (see Section 4.2). The Čerenkov ADC distribution for this run is shown in Figure 6.30. The peak above 1500 ADC counts is for electrons, the other resulting from noise and heavier particles. To obtain a cleaner sample, events with less than 1700 ADC counts were cut. 15 997 electrons were retained after the cut.

Figure 6.31(a) shows the distribution of the total charge in npe read out through the clear fibre and WLS fibre for the electron sample. The distribution for the side with WLS fibre (shown in green) has lower charge than the clear-fibre distribution (shown in blue) because of the extra attenuation through the WLS fibre.

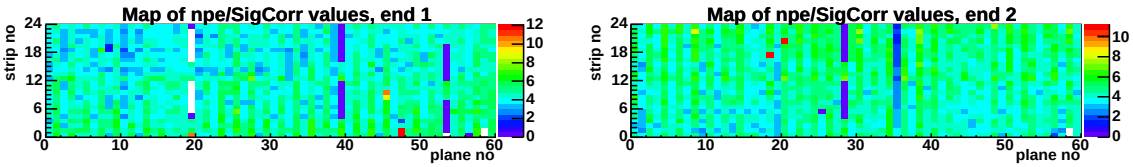

(a) Map of $\overline{p_i^{\text{corr}}}$ in units of npe/SigCorr.

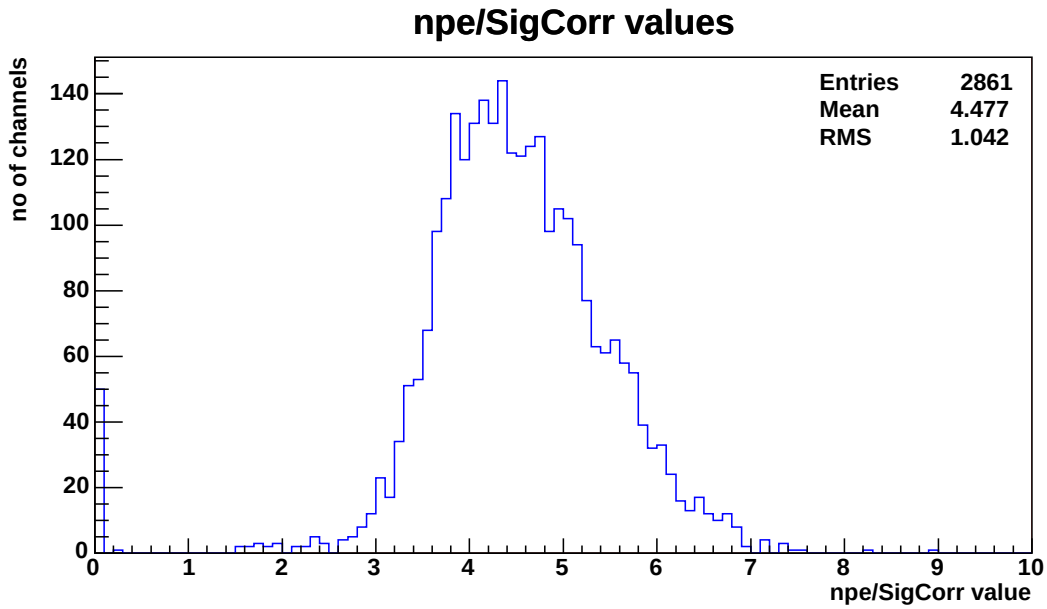

(b) Distribution of $\overline{p_i^{\text{corr}}}$ values.

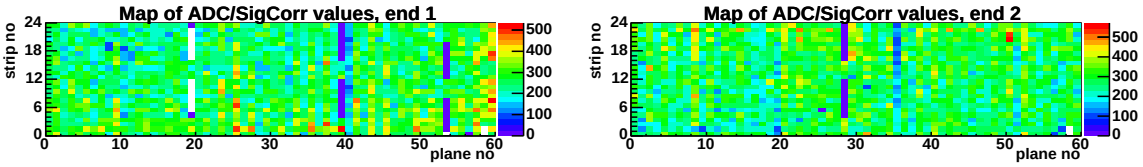

(c) Map of ADC/SigCorr values.

Figure 6.26: Calibration constants generated using 348 784 cosmic muons from a 13.2-hour run.

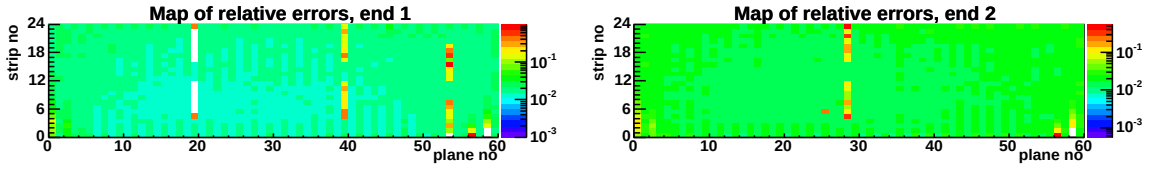

(a) Map of relative errors of calibration constants.

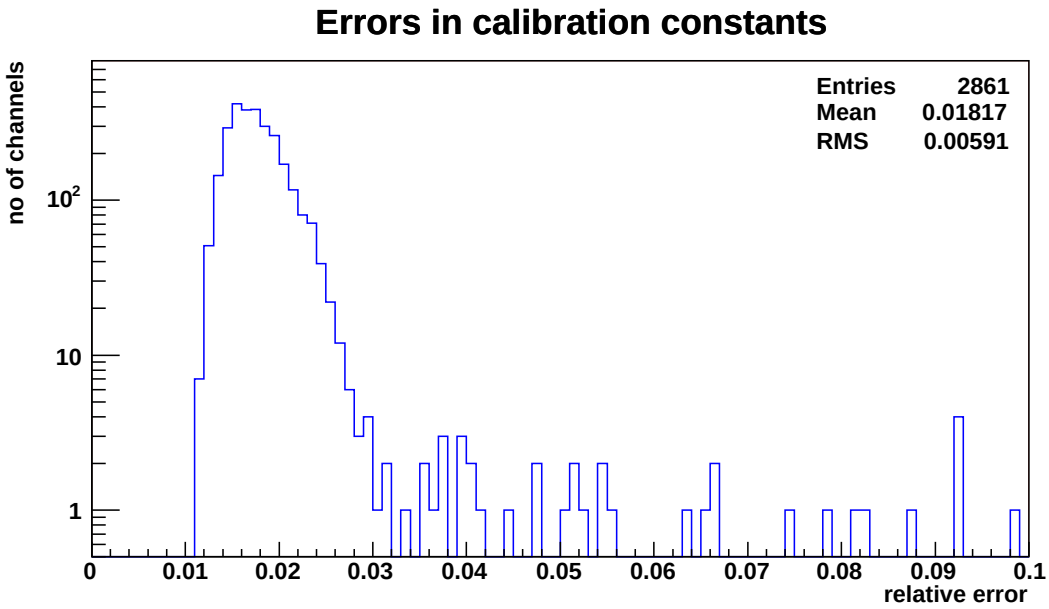

(b) Distribution of the relative errors.

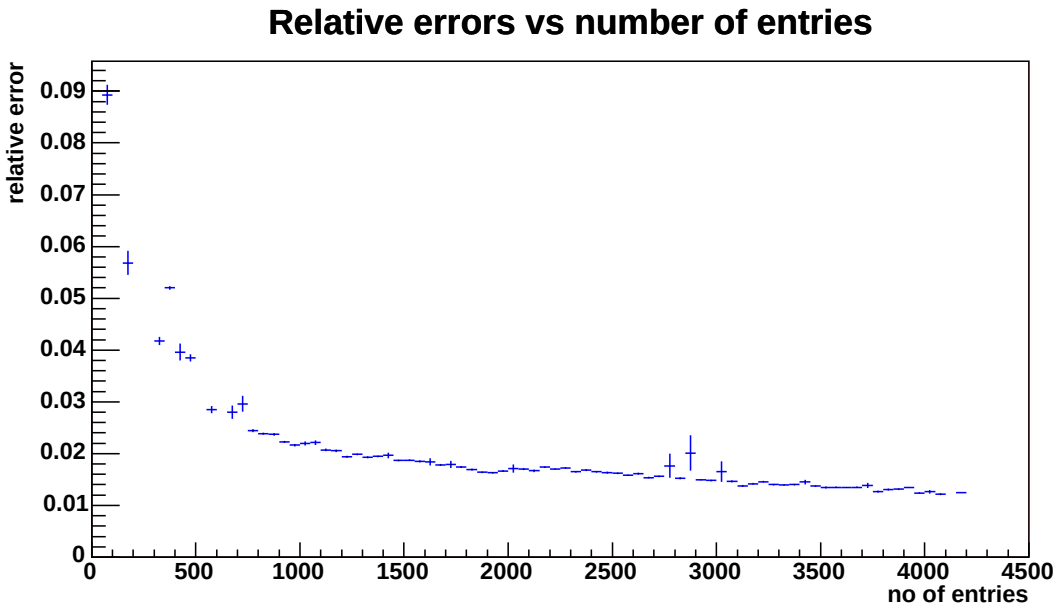

(c) Variation of calibration constants as function of number of entries.

Figure 6.27: Relative errors of calibration constants from the same 13.2-hour run.

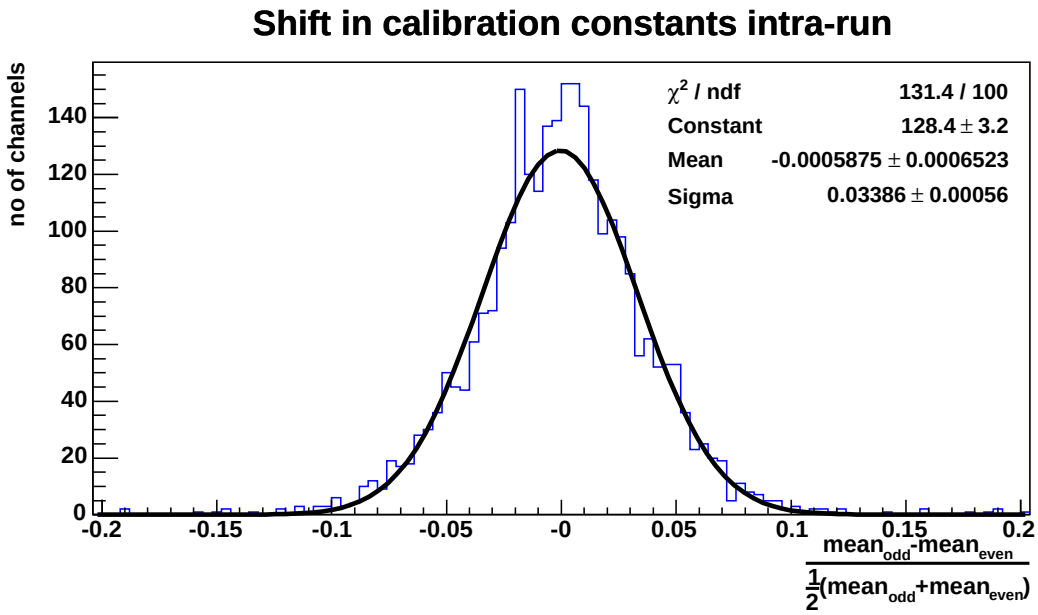

(a) Relative shift in value of $\overline{p_i^{corr}}$.

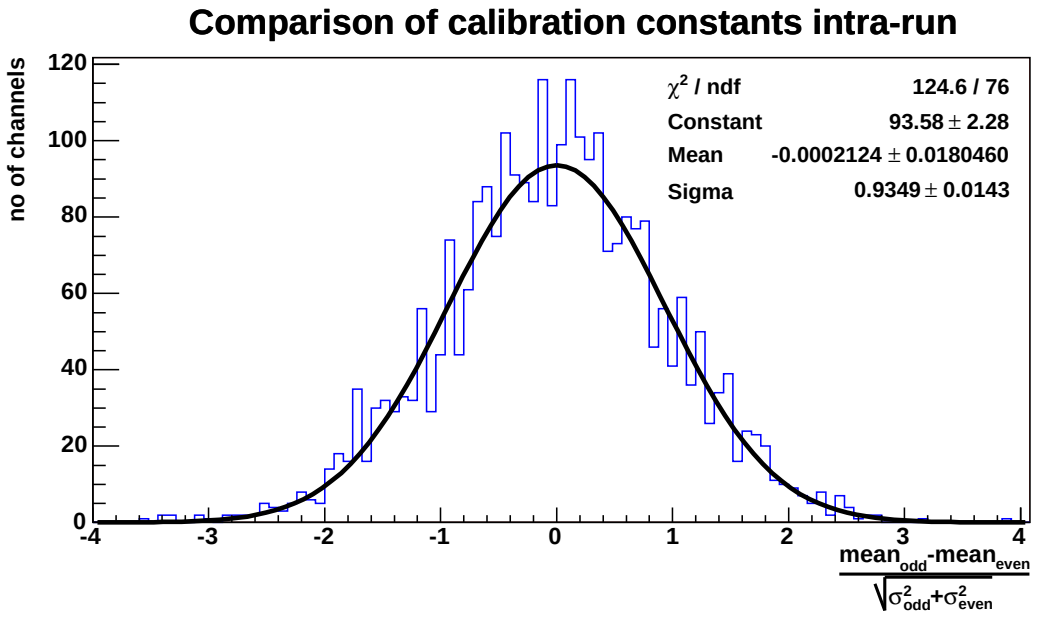

(b) Check of error estimates of $\overline{p_i^{corr}}$.

Figure 6.28: Consistency check of calibration constants within a single run.

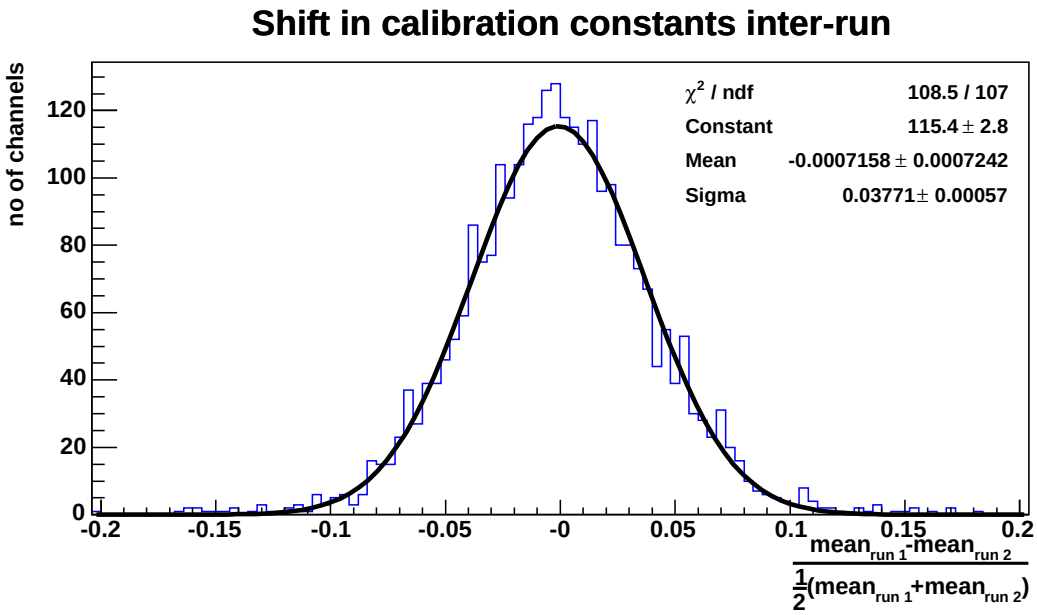

(a) Relative shift in value of $\overline{p_i^{\text{corr}}}$.

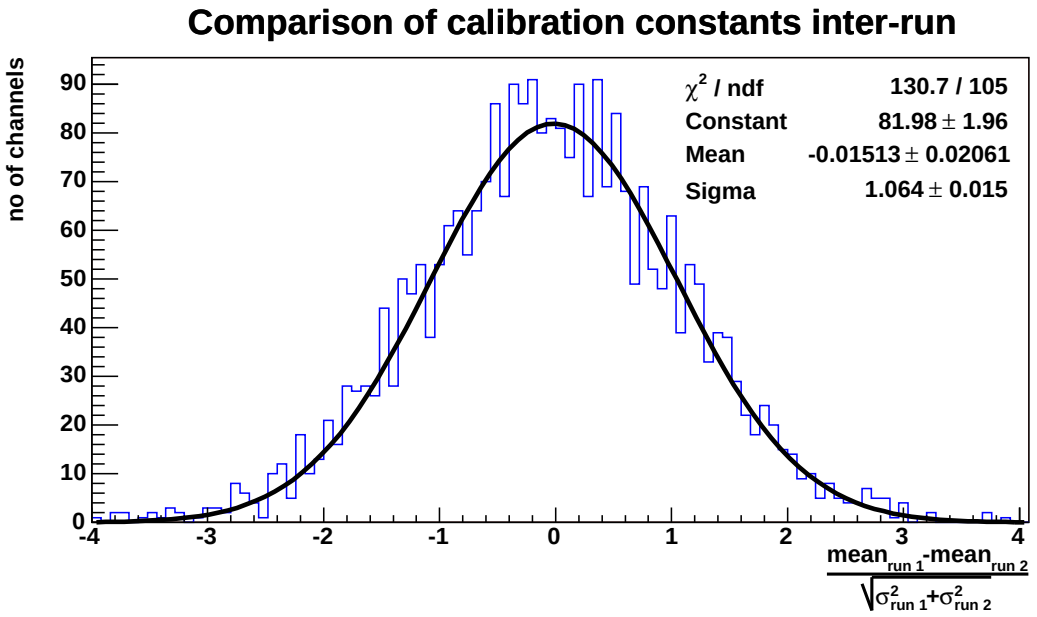

(b) Check of error estimates of $\overline{p_i^{\text{corr}}}$.

Figure 6.29: Comparison of calibration constants between two separate runs.

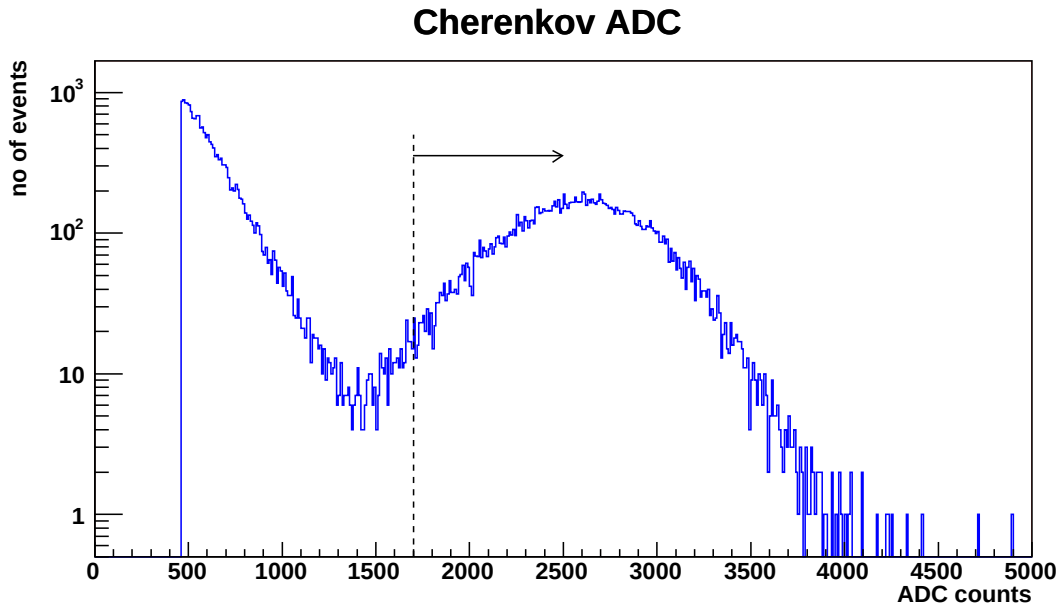

Figure 6.30: Čerenkov ADC distribution. The dashed line shows the cut at 1700 ADC counts.

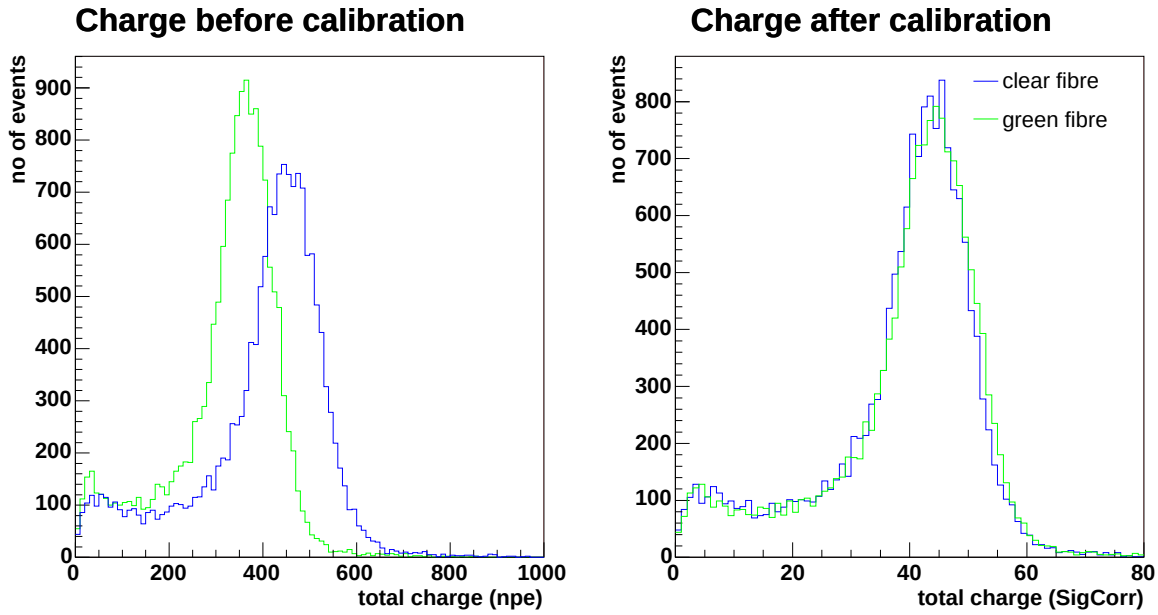

(a) Total charge in npe before calibration

(b) Total charge in SigCorr after calibration

Figure 6.31: Total charge of electrons. The blue histogram shows the charge read out from the side coupled through clear fibre, and the green shows the charge from the side with WLS fibre.

Figure 6.31(b) shows the total charge in SigCorr after applying the strip-to-strip calibration. The difference between the means of the two distributions has been reduced from 21% to 1.8%. This demonstrates that the calibration has largely equalized the response from the two sides. The remaining 1.8% discrepancy can be interpreted as a systematic error. The relative width of the total charge is 13.5%, which agrees reasonably well with the expected value of 12.3% calculated [4] from

$$\frac{\sigma_{E_{\rm e}}}{E_{\rm e}} = \frac{23\%}{\sqrt{E_{\rm e}}} \tag{6.15}$$

where $E_{\rm e}$ is the electron energy measured in GeV.

6.7.2 Muons

Beam muons were used to study the energy deposited per plane. At 3.5 GeV, the muons have sufficient energy that they enter the front of the detector and exit out the rear without being absorbed. The muon tracks were reconstructed using the algorithm described in Section 5.2. The beam muons were selected by requiring that the first and last planes of the detector were hit, and also that at least 55 planes were hit. 16 200 muons were retained after these cuts.

Figure 6.32(a) shows the energy deposited in SigCorr per plane. The average energy in the first plane is lower than other planes. This is because there is steel in front of subsequent planes, so there will be δ-rays escaping from the steel and entering the scintillator, thereby increasing the amount of energy deposited relative to the first plane. From the second plane the average energy per plane is slightly more than 1 SigCorr ($\approx$ 1 MIP). This is because the muons have energy above minimum ionization, so, according to the Bethe-Bloch formula [9], the energy deposited will be greater than for a minimum-ionizing particle (see Figure 6.33). From here the energy deposited decreases as the muon penetrates farther into the detector. This also results from the muons having energy above minimum ionization; according to Bethe-Bloch, the energy deposited decreases as the particle loses energy (see Figure 6.33). The anomalously low average energies of planes 19, 28, 39 and 53 are caused by dead PMTs (recall Figure 6.9).

The variation in the energy per plane $\overline{m}$ was estimated by fitting a straight line to Figure 6.32(a) and histogramming the relative difference $\frac{\Delta\overline{m}}{\overline{m}}$ between the data and the fit line for each plane, omitting the first four planes and the ones with dead PMTs:

$$\frac{\Delta\overline{m}}{\overline{m}} = \frac{\overline{m}_{\rm data} - \overline{m}_{\rm fit}}{\overline{m}_{\rm fit}} \,. \tag{6.16}$$

The histogram, plotted in Figure 6.32(b), shows that the variation is 1.8%. The average statistical error per strip is 1.8% (see Figure 6.27(b)). However, since the muons are illuminating the entire face of the detector, the energy per plane is being averaged over all 24 strips; therefore, the statistical error per plane reduces to $\frac{1.8\%}{\sqrt{24}} = 0.4\%$, which is negligible compared to 1.8%. This means that for muons, the calibration has a 1.8% systematic error, which is an independent confirmation of the estimate obtained from electrons.

Figure 6.34 shows the same plots as in Figure 6.32, but without applying the strip-to-strip calibration. The variation is 6.9%, so applying the strip-to-strip calibration reduces the variation in energy per plane significantly.

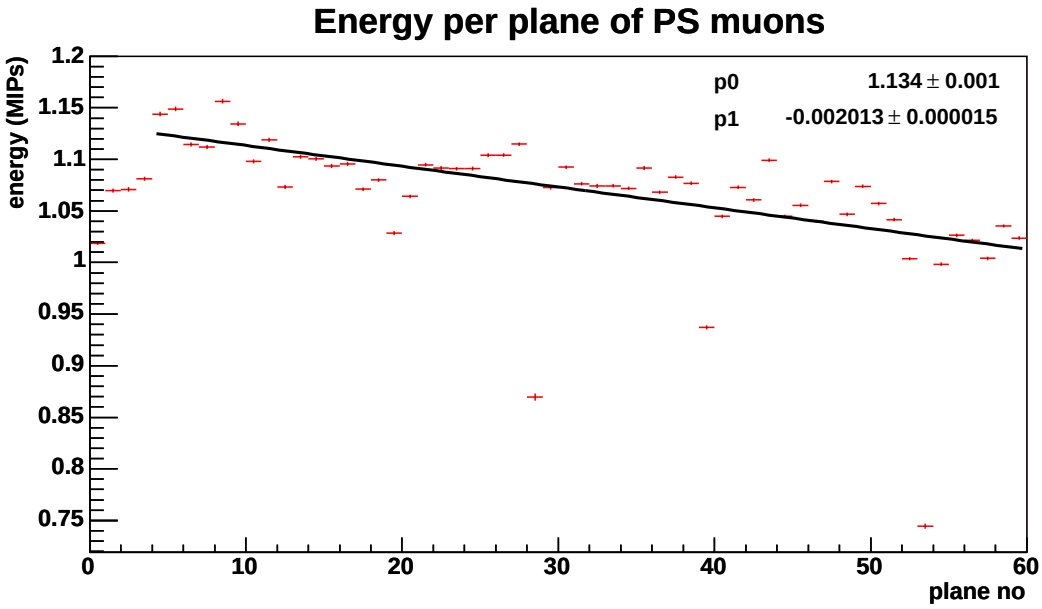

(a) Energy per plane in SigCorr of beam muons. The red points represent data. The black line is a linear fit to the data.

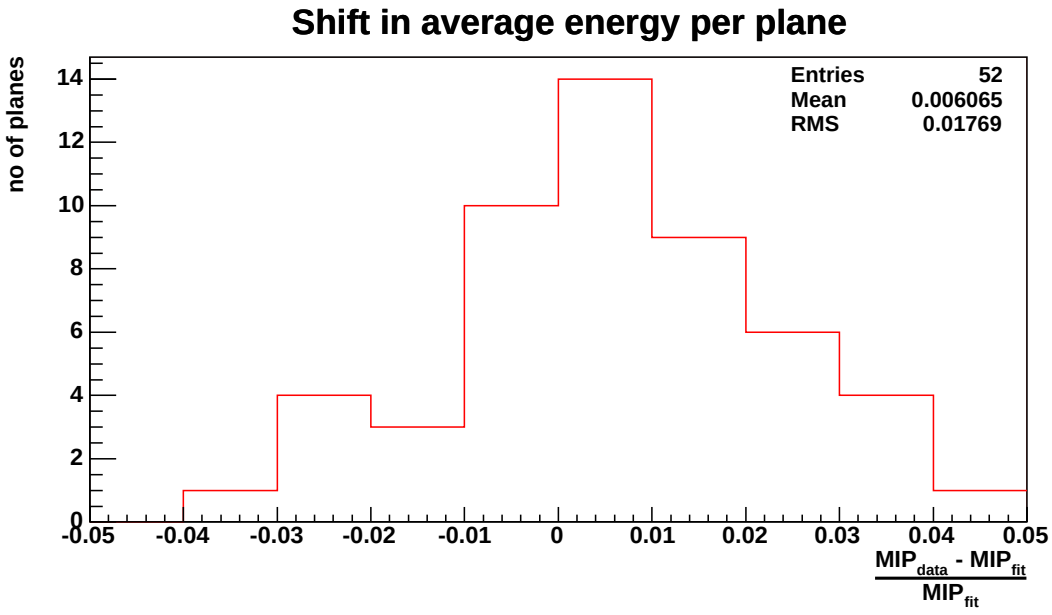

(b) Relative difference in average energy per plane between data and fit.

Figure 6.32: Results from applying to strip-to-strip calibration to beam muons.

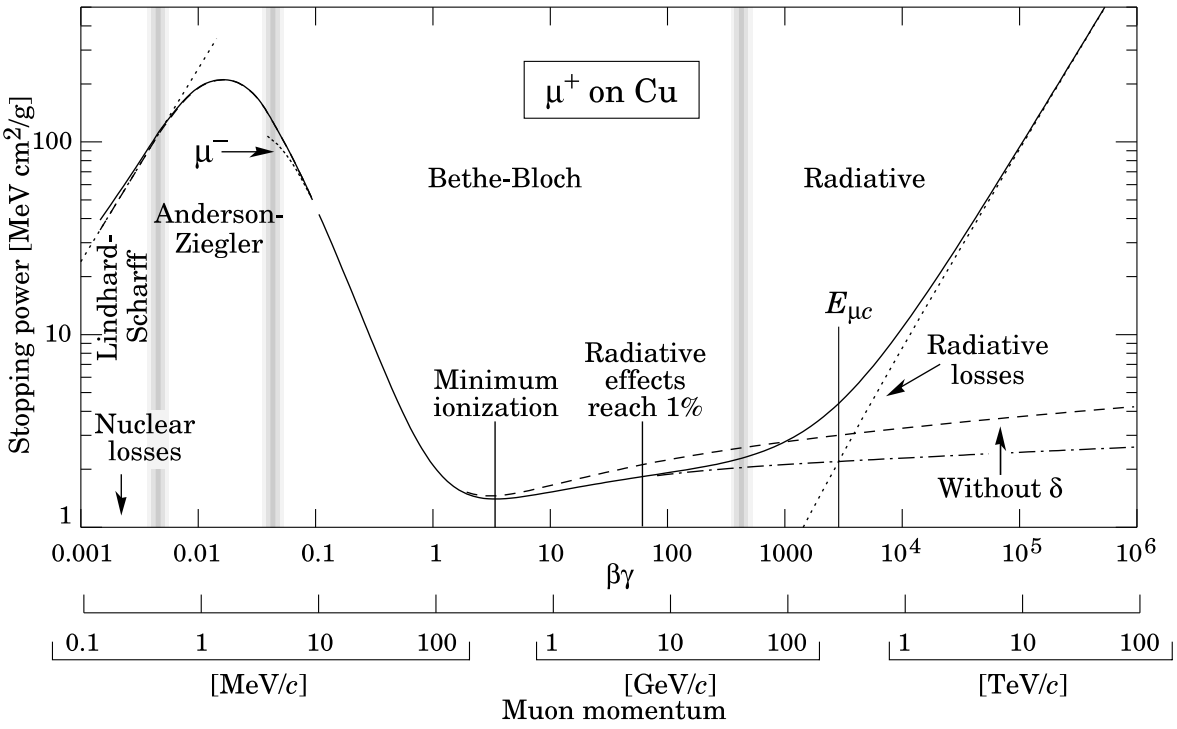

Figure 6.33: Stopping power of muons in copper according to the Bethe-Bloch formula (figure from [9]).

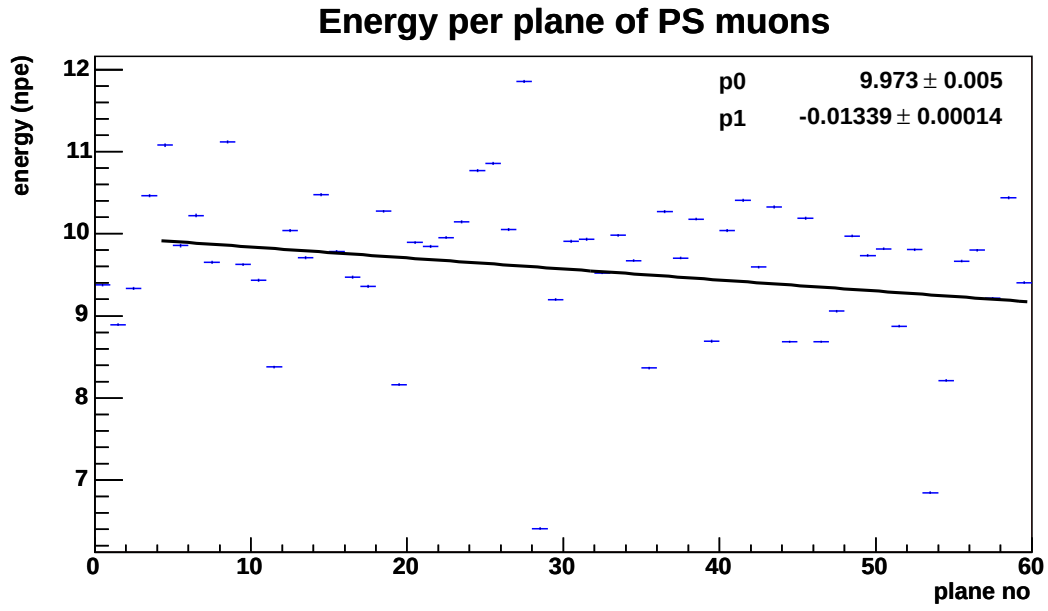

(a) Energy per plane in npe of beam muons. The blue points represent data. The black line is a linear fit to the data.

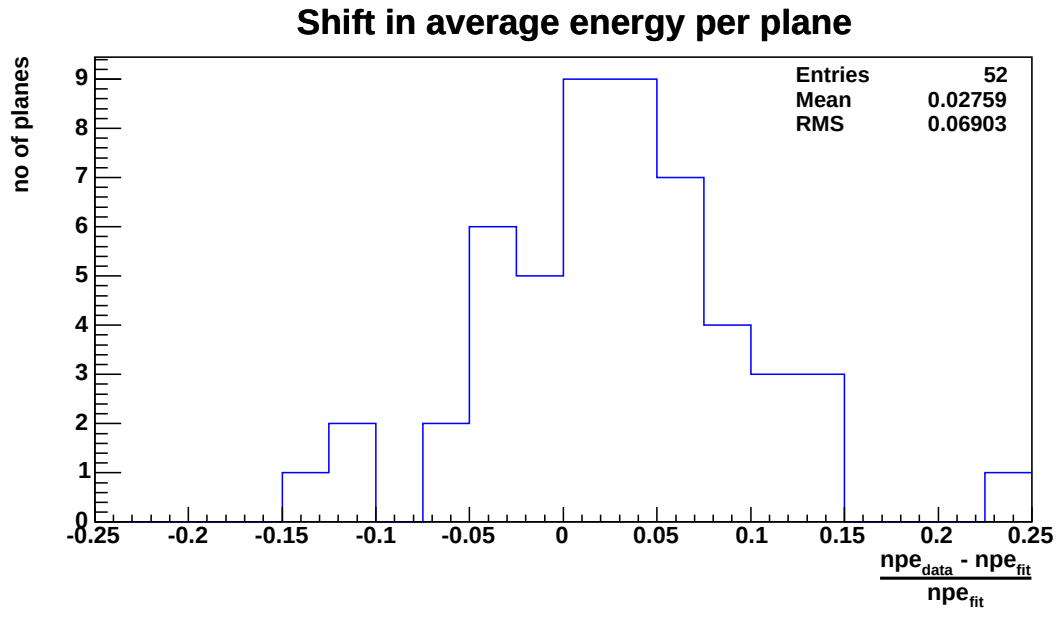

(b) Relative difference in average energy per plane between data and fit.

Figure 6.34: Results from beam muons before applying strip-to-strip calibration.

— CHAPTER SEVEN —

Impact of Strip-to-Strip Calibration on MINOS

7.1 Energy Resolution of the MINOS Detectors

As discussed in Chapter 3, MINOS measures the neutrino oscillation parameters by using the ν_μ charged-current spectra. The energy of the neutrino $E_{\nu_\mu}^{\text{true}}$ is

$$E_{\nu_\mu}^{\text{true}} = E_\mu^{\text{vis}} + E_{\text{hadron}}^{\text{vis}} + E^{\text{invis}} \,, \tag{7.1}$$

where E_μ^{vis} and $E_{\text{hadron}}^{\text{vis}}$ are the visible energies of the muon and hadronic shower respectively, and E^{invis} is the invisible energy in the nuclear recoil. As a first approximation, MINOS will measure the reconstructed neutrino energy $E_{\nu_\mu}^{\text{reco}}$ as

$$E_{\nu_\mu}^{\text{reco}} = E_\mu^{\text{vis}} + E_{\text{hadron}}^{\text{vis}} \,, \tag{7.2}$$

so the discrepancy ΔE between the reconstructed and true energies will be

$$\Delta E \equiv E_{\nu_\mu}^{\text{true}} - E_{\nu_\mu}^{\text{reco}} = E_{\nu_\mu}^{\text{true}} - E_\mu^{\text{vis}} - E_{\text{hadron}}^{\text{vis}} \,. \tag{7.3}$$

In reality, of course, the detector resolution will have to be accounted for. The energy of the muon is measured by using either its range in the detector or the curvature of its track in the magnetic field. The muon energy resolution is estimated [82, 112] to be

$$\frac{\sigma_{E_\mu}}{E_\mu} < 12\% \,, \tag{7.4}$$

in particular $\sim$6% by range for muons contained within the detector and $\sim$11% by curvature for muons which exit the detector [112]. The energy of the hadronic shower is measured by using the detector as a calorimeter. The intrinsic shower resolution has been measured [99] to be

$$\frac{\sigma_{E_{\text{hadron}}}^{\text{intrin}}}{E_{\text{hadron}}} = \frac{50\%}{\sqrt{E_{\text{hadron}}}} \,, \tag{7.5}$$

where E_{hadron} is measured in GeV. However, since the shower energy is measured using calorimetry, the variation in light output from strip to strip becomes significant. As seen in Figure 6.26(c), the variation in light levels between strips is $\frac{\sigma_{E_{\text{strip}}}}{E_{\text{strip}}} = 23\%$. Therefore, the

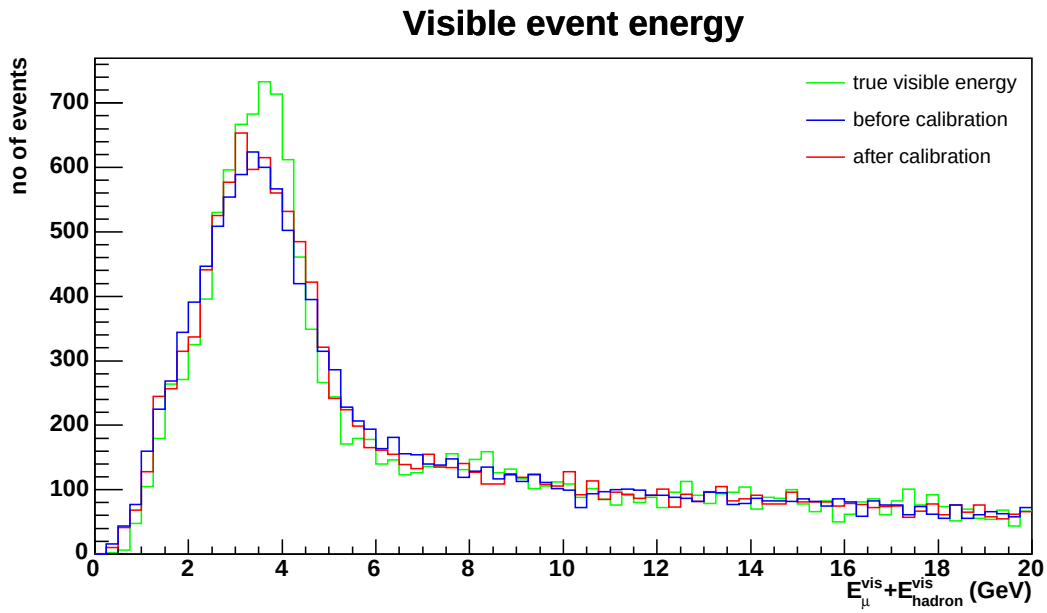

Figure 7.1: Effect of detector resolution on visible event energy. The green distribution shows the true visible energy spectrum. The blue distribution includes smearing for detector resolution. The red distribution shows the smeared spectrum after the strip-to-strip calibration has been applied.

total shower resolution is

$$\begin{aligned}\frac{\sigma_{E_{\text{hadron}}}}{E_{\text{hadron}}} &= \sqrt{\left(\frac{\sigma^{\text{intrin}}_{E_{\text{hadron}}}}{E_{\text{hadron}}}\right)^2 + \left(\frac{\sigma_{E_{\text{strip}}}}{E_{\text{strip}}}\right)^2} \\ &= \sqrt{\left(\frac{50\%}{\sqrt{E_{\text{hadron}}}}\right)^2 + (23\%)^2}\,.\end{aligned} \tag{7.6}$$

The strip-to-strip calibration is designed to eliminate variations between strips, i.e., applying the calibration reduces $\frac{\sigma_{E_{\text{strip}}}}{E_{\text{strip}}}$ to 2%, corresponding to the statistical error of the calibration.

Figure 7.1 illustrates the effect of the detector resolution on the reconstructed visible event energy for neutrinos produced by the low-energy beam. The distribution in green shows the true visible energy spectrum. The distribution in blue has the muon energy smeared by 12% (worst case of Equation 7.4) and the hadron energy smeared by Equation 7.6, resulting in a broadened spectrum. Applying the strip-to-strip calibration reduces the smearing of the hadron energy, giving the narrower red spectrum.

Figure 7.2 illustrates how the detector resolution affects the reconstructed neutrino energy. The blue distribution shows the discrepancy ΔE between the true neutrino energy and the reconstructed visible energy with full smearing included. The red distribution shows ΔE with the strip-to-strip calibration applied, reducing the smearing of the reconstructed hadron energy. The red is narrower than the blue by 13%, indicating that the calibration reduces the discrepancy between true and reconstructed energy.

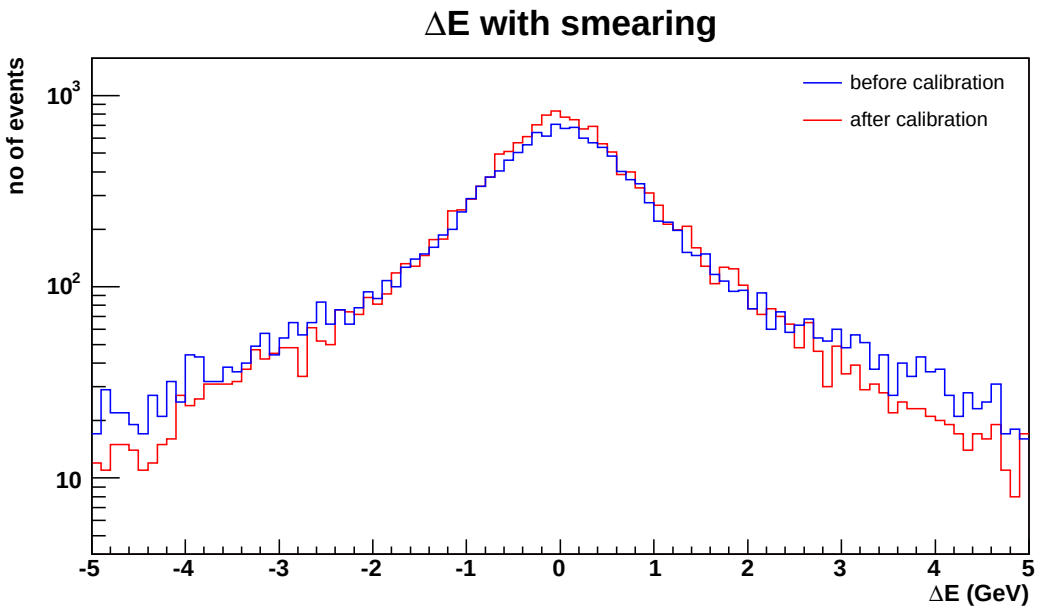

Figure 7.2: Effect of detector resolution on energy reconstruction. The blue distribution shows ΔE (from Equation 7.3) where the reconstructed visible energy has been smeared for detector resolution. The red distribution shows ΔE with the strip-to-strip calibration applied to the reconstructed energy.

7.2 Effect on Oscillation Parameter Measurement

The effect of the strip-to-strip calibration on the measurement of oscillation parameters by MINOS was studied using a Monte Carlo simulation based on ROOT. It was developed originally by Dr. Alfons Weber to study parameter fitting using the charged-current (CC) and neutral-current (NC) spectra [113]. It has been adapted by this author to include detector resolution effects.

The Monte Carlo simulates 25 000 ν_μ from the low-energy beam interacting in the Far Detector, which is equivalent to 32×10^{20} protons on target. This produces 16 565 CC events. For these events the visible muon energy is smeared by 12% (worst case of Equation 7.4) and the visible hadron energy by Equation 7.6, with $\frac{\sigma_{E_{\text{strip}}}}{E_{\text{strip}}}$ set to both 2% and 23% to simulate the detector resolution with and without the strip-to-strip calibration applied. The visible energy spectrum, normalized to be equivalent to 4 years of running with 2×10^{20} protons on target per year, is shown as the green distribution in Figure 7.3(a) without the calibration applied, and in Figure 7.3(b) with.

An ideal oscillated spectrum is generated by weighting each event by the ν_μ survival probability:

$$\mathrm{P}(\nu_\mu \to \nu_\mu) = 1 - \sin^2 2\theta \sin^2 \left(\frac{1.27 \Delta m^2 L}{E_{\nu_\mu}} \right) , \tag{7.7}$$

where L is the set to the MINOS baseline (735 km). The oscillated spectrum with the oscillation parameters set to the latest Super-Kamiokande values ($\sin^2 2\theta = 1.00$, $\Delta m^2 = 2.4 \times 10^{-3}$ eV^2 [5]) is plotted as the red distributions in Figure 7.3.

A simulated spectrum of oscillated data is then generated. The number of entries in the data spectrum is set randomly using the number of events expected for 4 years of running with 2×10^{20} protons on target per year as the Poisson mean. The data spectrum is then filled

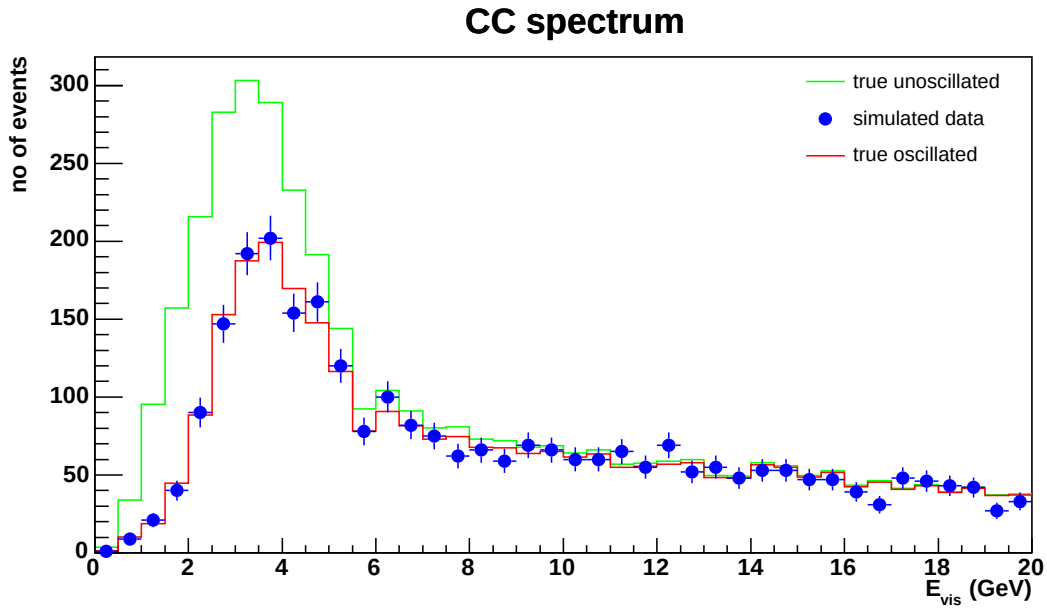

(a) Full (23%) strip-to-strip variations included.

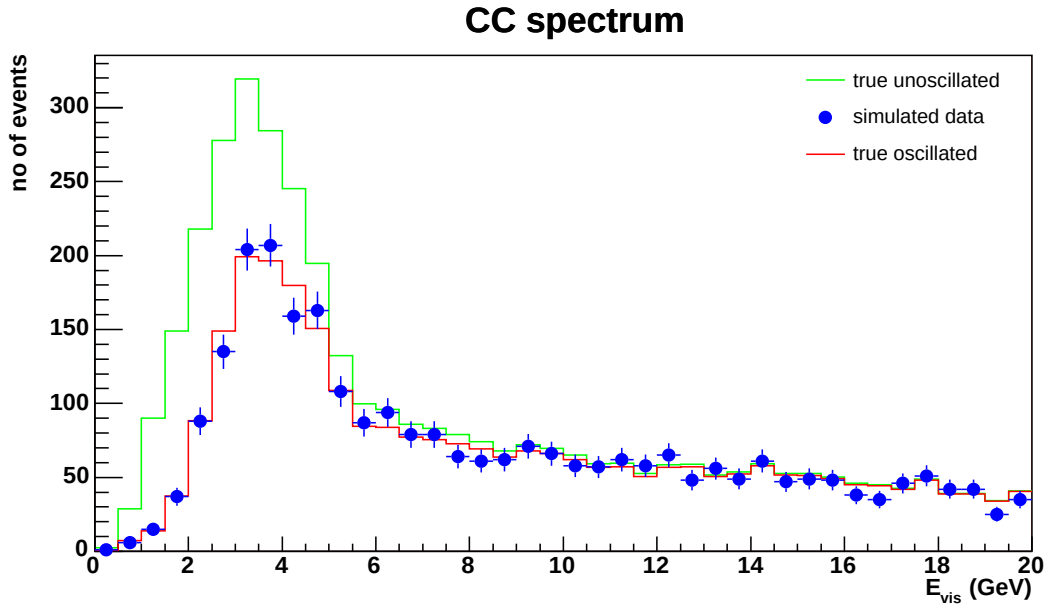

(b) Strip-to-strip calibration applied, reducing strip-to-strip variation to 2%.

Figure 7.3: Charged current spectra measured at the Far Detector with detector resolution included. The spectra shown are for a 5.4 kilotonne detector running for 4 years with 2×10^{20} protons on target per year. The green line is the true visible energy spectrum without oscillations. The red line is the true spectrum with oscillations assuming $\sin^2 2\theta = 1.00$, $\Delta m^2 = 2.4 \times 10^{-3}$ eV^2. The black dots represent the simulated oscillated spectrum filled randomly using Poisson statistics. All spectra have been smeared with the detector resolution.

randomly from the ideal oscillated spectrum. The data spectrum is shown as the blue points in Figure 7.3.

The oscillation parameters are extracted from the oscillated data using the method of maximum likelihood [9]. The likelihood function used fits the data to the shape of the CC spectrum, but does not use the normalization. The probability that an event will fall into the ith bin is

$$\mathrm{P}_i = \frac{N_i^{\mathrm{MC}}}{\sum_j N_j^{\mathrm{MC}}} \, , \tag{7.8}$$

where N_i^{MC} is the number of entries in the ith bin of the ideal oscillated spectrum, smeared with the detector resolution, and depends on the oscillation parameters:

$$\begin{aligned} N_i^{\mathrm{MC}} &= N_i^{\mathrm{unosc}} \, \mathrm{P}_i(\nu_\mu \to \nu_\mu) \\ &= N_i^{\mathrm{unosc}} \left[1 - \sin^2 2\theta \sin^2 \left(\frac{1.27 \Delta m^2 L}{E_i} \right) \right] \, , \end{aligned} \tag{7.9}$$

where N_i^{unosc} is the number of entries in the ith bin of the unoscillated spectrum. The likelihood function for the data spectrum then becomes

$$\mathcal{L} = \prod_i \left(\mathrm{P}_i \right)^{N_i^{\mathrm{data}}} \, , \tag{7.10}$$

where N_i^{data} is the number of entries in the ith bin of the data spectrum. The function to be minimized is then

$$-2 \log \mathcal{L} = -2 \sum_i N_i^{\mathrm{data}} \log \mathrm{P}_i \tag{7.11}$$

by solving the likelihood equations:

$$\frac{\partial(-2 \log \mathcal{L})}{\partial \Delta m^2} = 0 \, , \qquad \frac{\partial(-2 \log \mathcal{L})}{\partial \sin^2 2\theta} = 0 \, . \tag{7.12}$$

Given the minimum value $-2 \log \mathcal{L}_{\mathrm{max}}$, the $n\sigma$ allowed region is bounded by the contour

$$-2 \log \mathcal{L} = -2 \log \mathcal{L}_{\mathrm{max}} + n^2 \, . \tag{7.13}$$

The minimization and contour-fitting is performed by the TMinuit package [114] of ROOT to determine the oscillation parameters.

Figure 7.4 illustrates the increase in sensitivity when the calibration is applied. The 90% confidence limits were determined for two sets of values of the oscillation parameters: the Super-Kamiokande values ($\Delta m^2 = 2.4 \times 10^{-3}$ eV^2, $\sin^2 2\theta = 1$), and the values at which MINOS has the greatest sensitivity ($\Delta m^2 = 5.0 \times 10^{-3}$ eV^2, $\sin^2 2\theta = 1$). These test points are marked by the stars. The blue areas, which include the red, represent the allowed regions before the strip-to-strip calibration has been applied to the data. The red areas demarcate the allowed regions after the calibration has been applied. The calibration has improved the lower limit of $\sin^2 2\theta$ from 0.90 to 0.92.

The accuracy of the Δm^2 fit was investigated. Several points in the oscillation parameter space were used with $\sin^2 2\theta$ fixed at 1 and Δm^2 varying from 1.5 to 5 $\times 10^{-3}$ eV^2. For each pair of parameter values, 100 data spectra were generated, each spectrum was fitted, and the fit results histogrammed. Figure 7.5(a) shows the discrepancy between the fit value and the true (MC) value of Δm^2. The plot indicates that the fit tends to overestimate Δm^2 at

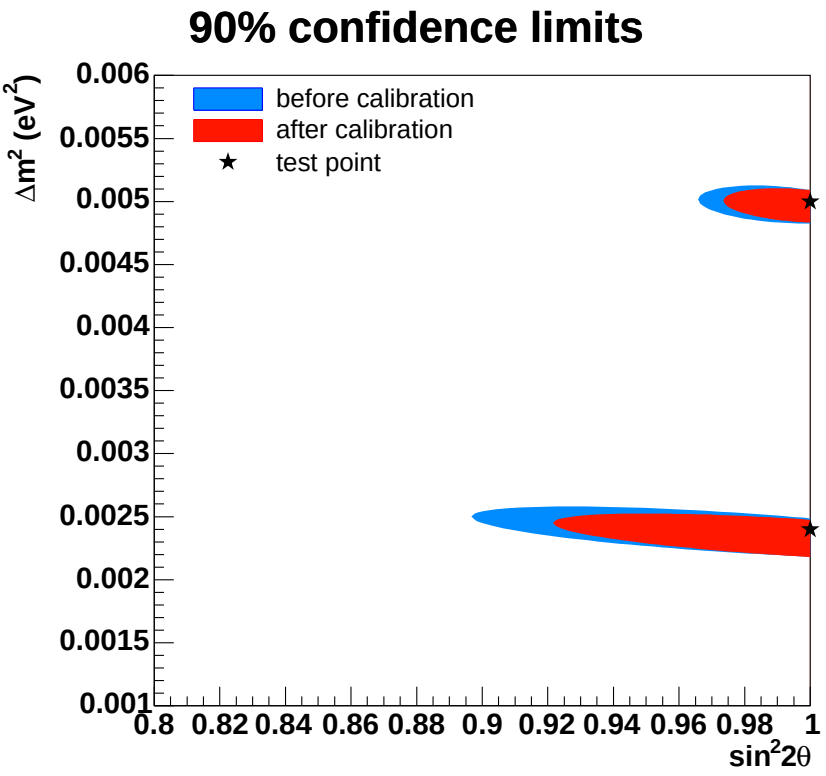

Figure 7.4: Sensitivity of MINOS to detector resolution. The 90% confidence limits are shown for test points, marked by stars, at the Super-Kamiokande values ($\Delta m^2 = 2.4 \times 10^{-3}$ eV^2, $\sin^2 2\theta = 1$) and the values at which MINOS is most sensitive ($\Delta m^2 = 5.0 \times 10^{-3}$ eV^2, $\sin^2 2\theta = 1$). The blue areas, which encompass the red, includes the full strip-to-strip variations. The red areas have had the strip-to-strip calibration applied. The running time and conditions are as in Figure 7.3.

lower values of Δm^2. Figure 7.5(b) shows the error in the fit value. Applying the calibration does not appear to affect the discrepancy, but the error in the fit value in general improves by $\sim$10%.

Figure 7.6 demonstrates why smearing causes the fit to overestimate Δm^2 at lower values. Starting from the unsmeared CC spectrum without oscillations (green distribution in Figure 7.6(a)), the unsmeared oscillated spectrum (blue) is generated by applying Equation 7.7 with parameters $\Delta m^2 = 1.5 \times 10^{-3}$ eV^2, $\sin^2 2\theta = 1$ to the entries in the unoscillated spectrum. As can be seen from the ratio of the oscillated spectrum to the unoscillated (blue line in Figure 7.6(b)), the greatest deficit in events is from the lower half of the peak in the CC spectrum. Adding in the effects of the detector resolution with the full strip-to-strip variation (Equations 7.4 and 7.6) broadens the oscillated spectrum (red distribution in Figure 7.6(a)) and most relevantly causes events to "migrate" from the main part of the energy peak, where the event deficit is small originally, to areas where the deficit is initially greater. This migration results in the ratio (red line in Figure 7.6(b)) becoming shallower and shifted to higher energies. Fitting Equation 7.7 to the dip yields $\Delta m^2 = 2.0 \times 10^{-3}$ eV^2, $\sin^2 2\theta = 0.41$, which has Δm^2 higher than the original value of 1.5×10^{-3} eV^2. Note that the best-fit curve (black line in Figure 7.6(b)) is for illustrative purposes only; the standard method of maximum likelihood would use a fit to the CC spectrum (red distribution in Figure 7.6(a)). This indicates that a more sophisticated fit is required when determining the value of Δm^2.

The importance of modelling the smearing correctly was also investigated by taking N_i^{MC}

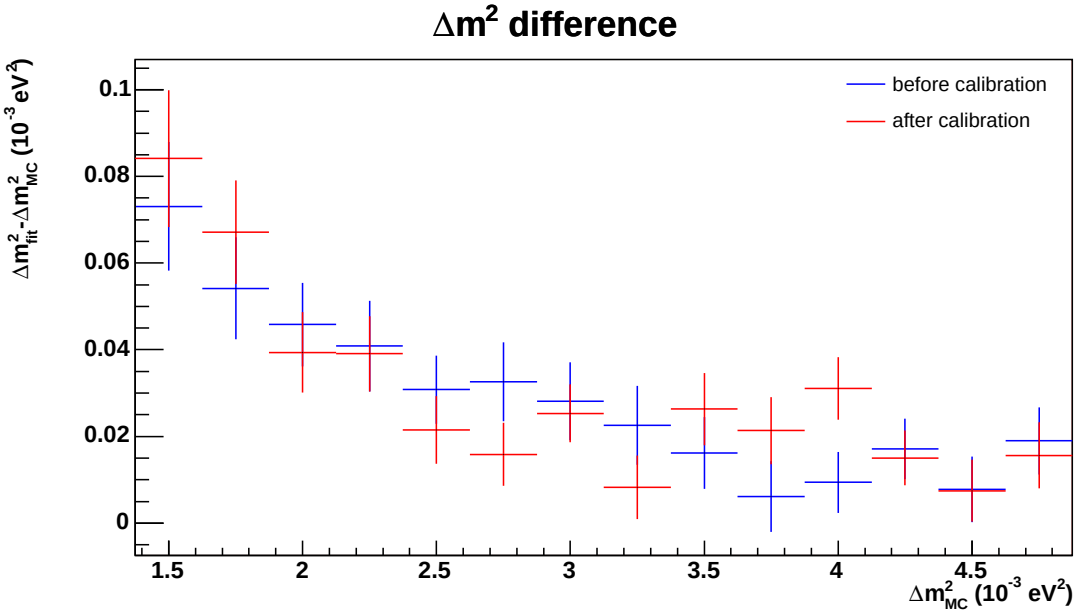

(a) Difference between the best-fit Δm^2 value and the true value.

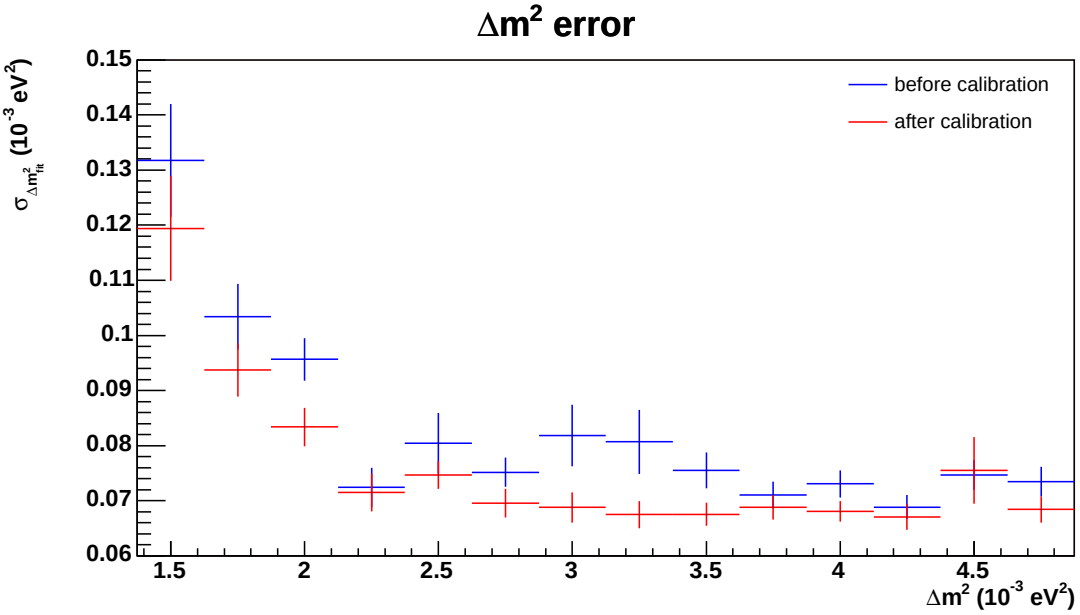

(b) Error in the Δm^2 fit value.

Figure 7.5: Accuracy and precision of Δm^2 measurement by MINOS at $\sin^2 2\theta = 1$. The blue plot shows results including the full strip-to-strip variation. The red plot shows results after applying the strip-to-strip calibration. 100 data spectra were generated for each point in the graph.

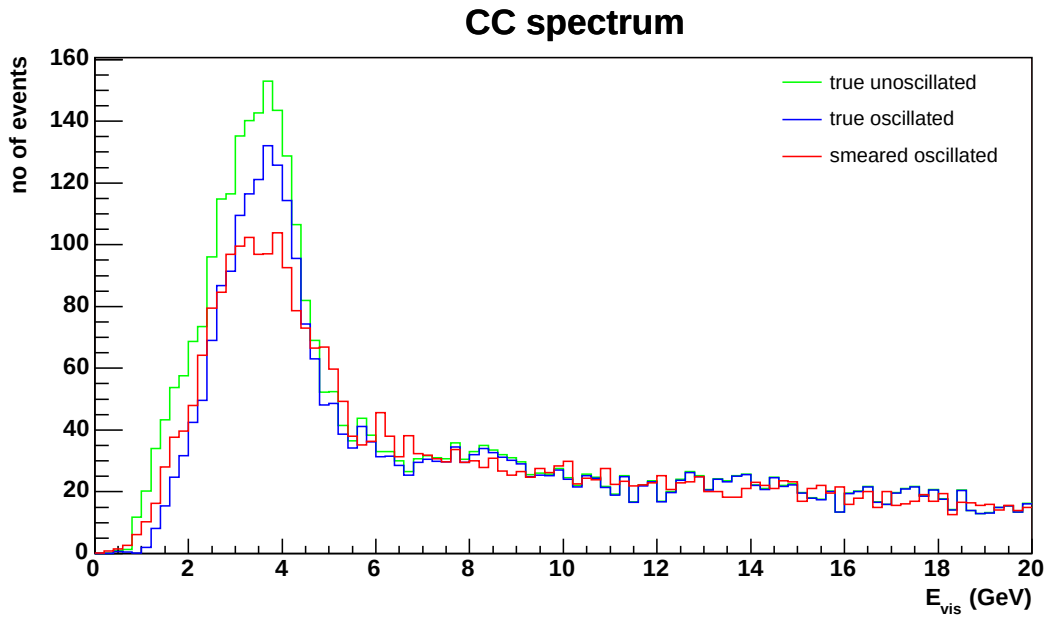

(a) Charged current spectra measured at the Far Detector. The green distribution shows the ideal unoscillated spectrum. The blue shows the ideal oscillated spectrum. The red shows the oscillated spectrum including detector resolution effects. The deficit in events is largely on the lower side of the spectrum peak.

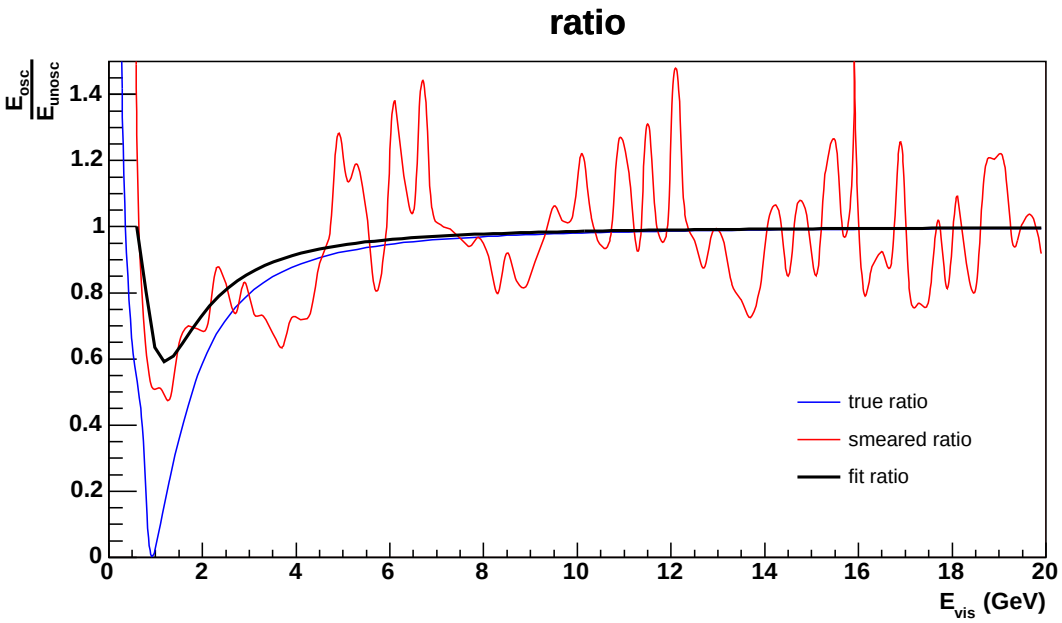

(b) Ratio of oscillated spectrum to the unoscillated spectrum. The blue line shows the ideal ratio. The red line shows the ratio using the smeared spectrum. The black line, for the best fit curve with $\Delta m^2 = 2.0 \times 10^{-3}$ eV^2, $\sin^2 2\theta = 0.41$, is for illustrative purposes only.

Figure 7.6: Demonstration of smearing causing Δm^2 to be overestimated at lower values of Δm^2. The oscillated spectra are for $\Delta m^2 = 1.5 \times 10^{-3}$ eV^2, $\sin^2 2\theta = 1$.

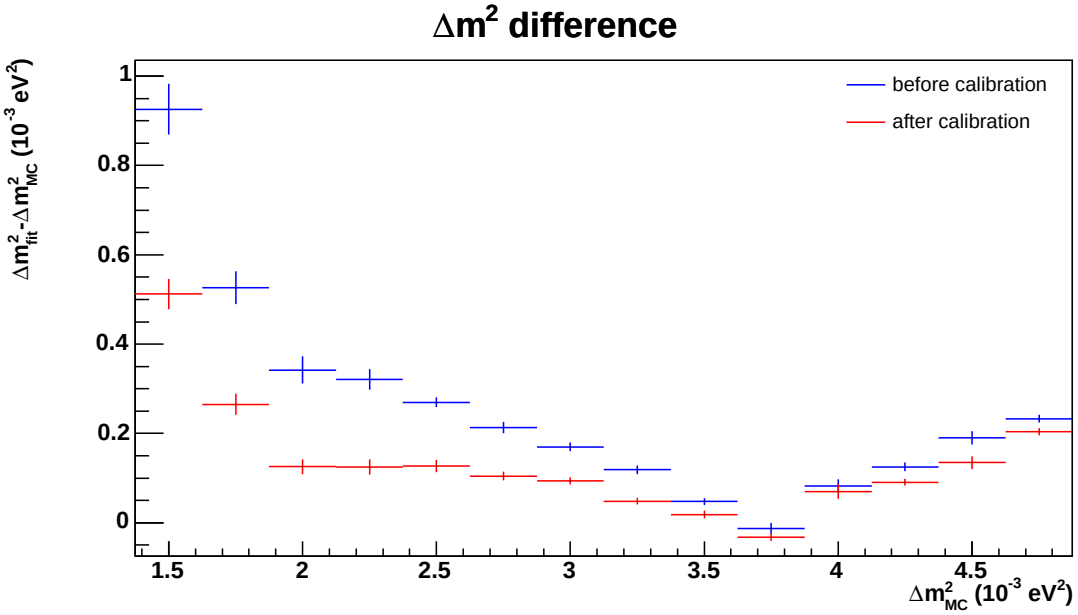

Figure 7.7: Accuracy of Δm^2 measurement at $\sin^2 2\theta = 1$ using an unsmeared CC spectrum in the fit. The blue plot shows results including the full strip-to-strip variation. The red plot shows results after applying the strip-to-strip calibration. 100 data spectra were generated for each point in the graph.

in Equation 7.8 from an unsmeared Monte Carlo spectrum rather than a smeared one. Figure 7.7 demonstrates that the results from fitting an unsmeared Monte Carlo spectrum to a smeared data spectrum are significantly worse.

The $\sin^2 2\theta$ fit was investigated in a similar manner, but with Δm^2 fixed at 2.4×10^{-3} eV^2 and $\sin^2 2\theta$ varying from 0.8 to 1. The results for the fit to a smeared CC spectrum are shown in Figure 7.8. The discrepancy is negligible for lower values of $\sin^2 2\theta$, but near 1 the discrepancy becomes negative. This is expected since $\sin^2 2\theta$ cannot exceed 1, so the discrepancy can be only negative. Applying the calibration reduces the error in the fit value in general by $\sim$10%. Figure 7.9 shows that results from fitting to an unsmeared spectrum are again significantly worse.

In summary, the strip-to-strip calibration is capable of improving the statistical error of the measured oscillation parameters by $\sim$10%. This corresponds to a 20% increase in the number of protons on target, allowing MINOS to reach its desired sensitivity in a shorter time. Modelling the smearing in the CC spectrum used for fitting is important for improving the measurement. However, there remains an inherent bias caused by the data smearing in the measured Δm^2 at lower values of Δm^2.

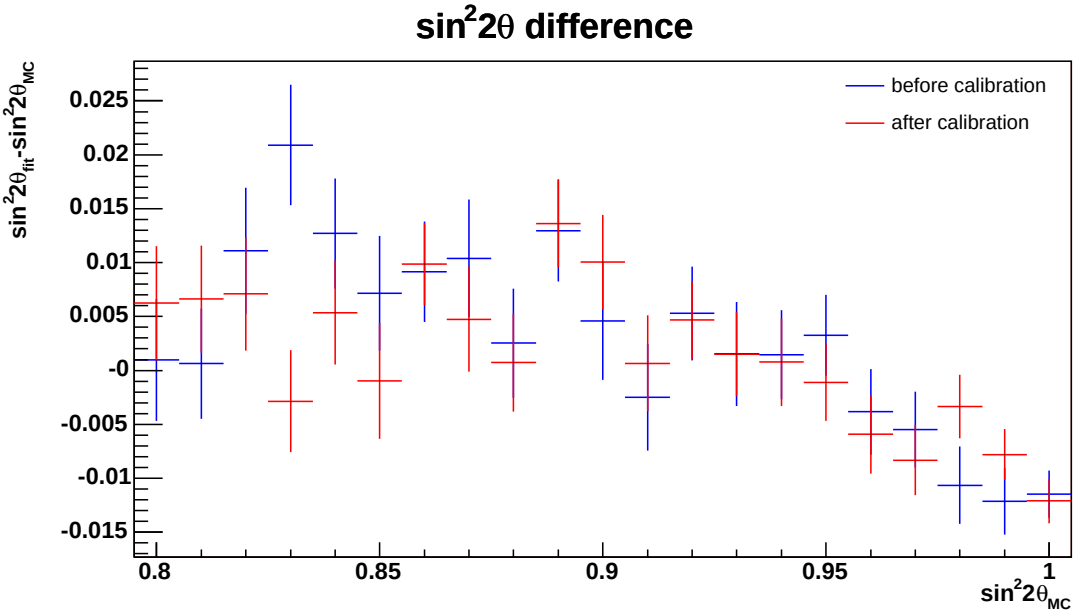

(a) Difference between the best-fit $\sin^2 2\theta$ value and the true value.

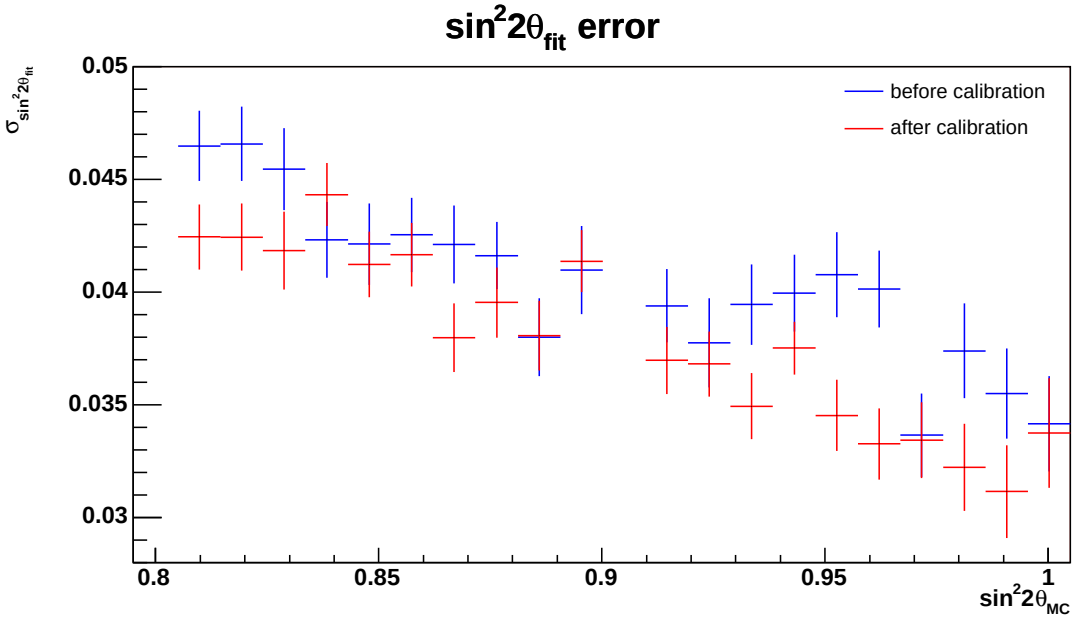

(b) Error in the $\sin^2 2\theta$ fit value.

Figure 7.8: Accuracy and precision of $\sin^2 2\theta$ measurement by MINOS at $\Delta m^2 = 2.4 \times 10^{-3}$ eV^2. The blue plot shows results including the full strip-to-strip variation. The red plot shows results after applying the strip-to-strip calibration. 100 data spectra were generated for each point in the graph.

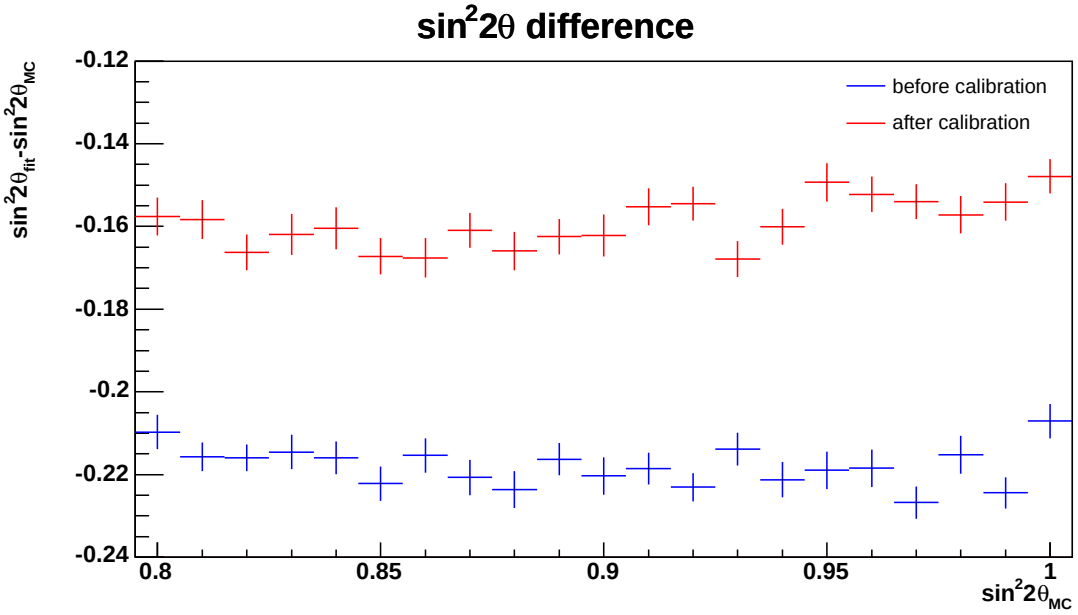

Figure 7.9: Accuracy of $\sin^2 2\theta$ measurement at $\Delta m^2 = 2.4 \times 10^{-3}$ eV^2 using an unsmeared CC spectrum in the fit. The blue plot shows results including the full strip-to-strip variation. The red plot shows results after applying the strip-to-strip calibration. 100 data spectra were generated for each point in the graph.

— CHAPTER EIGHT —

Conclusions

8.1 Strip-to-Strip Calibration

This thesis has detailed a procedure for producing a strip-to-strip calibration of the MINOS detectors using cosmic muons. The procedure has been tested on the Calibration Detector. Applying the calibration reduced the strip-to-strip variations in response from 23% to 1.8%. The systematic error was estimated to be 1.8%.

The procedure is ready to be applied to the Near and Far Detectors, although the track reconstruction will need to be updated to suit each particular detector. Some complications that were inherent in the Calibration Detector are not present in the Near and Far Detectors. One prime example is the fact that the Calibration Detector was read out with clear fibre on one side and green on the other, whereas the two main detectors are read out with clear fibre only; this leads to different light levels on the two sides in the Calibration Detector. Another difference is that the Calibration Detector has horizontal and vertical strips, whereas the other two detectors have strips rotated 45°; this results in different responses from the two views in the Calibration Detector. Nevertheless, the strip-to-strip calibration was demonstrated to correct for these effects.

One difference between all three detectors which will remain an issue is that all three detectors have different overburdens, i.e., they are at different depths in the ground. This means that each detector will see a different angular distribution (greater depth favours steeper tracks), and the average energy of the cosmic muons will also differ ($\sim$200 GeV at the Far Detector, $\sim$10 GeV at the Near, $\sim$3 GeV at the Calibration). This will lead to one SigCorr corresponding to a different energy at each detector (according to the Bethe-Bloch formula, 1 SigCorr $\sim$ 2 MeV/cm at the Near and Calibration Detectors, and $\sim$ 4 MeV/cm at the Far). The stopping muon calibration (see Section 3.5.3) will normalize the response of all three detectors in terms of minimum-ionizing particles (MIPs).

8.2 Impact on Oscillation Parameter Measurement

The potential impact of the calibration on the measurement of the oscillation parameters by MINOS has also been studied. The oscillation parameters were determined by fitting to the shape of the ν_μ charged-current spectrum using the method of maximum likelihood. Applying the calibration reduced the discrepancy in the reconstructed energy by 26%. This

consequently reduced the errors in the measured parameters by roughly 10%, which is equivalent to increasing the number of events by 20%. This shows that the strip-to-strip calibration can play an important role in the MINOS oscillation parameter measurement.

— APPENDIX A —

Translation of Pauli's Letter

4 Dec. 1930

Dear Radioactive Ladies and Gentlemen,

As the bearer of these lines, to whom I graciously ask you to listen, will explain to you in more detail, how because of the "wrong" statistics of the N- and Li-6 nuclei and the continuous beta spectrum, I have hit upon a desperate remedy to save the "exchange theorem" of statistics and the law of conservation of energy. Namely, the possibility that there could exist in the nuclei electrically neutral particles, that I wish to call neutrons, which have spin 1/2 and obey the exclusion principle and which further differ from light quanta in that they do not travel with the velocity of light. The mass of the neutrons should be of the same order of magnitude as the electron mass and in any event not larger than 0.01 proton masses. The continuous beta spectrum would then become understandable by the assumption that in beta decay a neutron is emitted in addition to the electron such that the sum of the energies of the neutron and the electron is constant. . . .

I agree that my remedy could seem incredible because one should have seen those neutrons very earlier if they really exist. But only the one who dares can win and the difficult situation, due to the continuous structure of the beta spectrum, is lighted by a remark of my honoured predecessor, Mr. Debye, who told me recently in Bruxelles: "Oh, it's well better not to think to this at all, like new taxes". From now on, every solution to the issue must be discussed. Thus, dear radioactive people, look and judge. Unfortunately, I cannot appear in Tübingen personally since I am indispensable here in Zurich because of a ball on the night of 6/7 December. With my best regards to you, and also to Mr. Back.

Your humble servant

W. Pauli

— APPENDIX B —

Cluster Merging Algorithm

The clustering algorithm described here was originally developed for cosmic muons in the Far Detector. The idea is to merge clusters that are close to each other until, at the end, each strip in a cluster is within a (2-dimensional) distance parameter of another strip in the same cluster, and every strip in a cluster is separated from every strip outside that cluster by at least that same distance. Figure B.1 shows an example outcome of this algorithm.

Figure B.2 contains a pseudocode representation of the clustering algorithm, and Figures B.3 and B.4 illustrate in detail the algorithm in action, producing the result in Figure B.1. Initially, each strip is treated as being within its own cluster, and these clusters form a list of "old" clusters. The first cluster is then removed from the old list and added to a list of "new" clusters. A loop is then performed over the remaining old clusters. As each cluster is removed from the old list, it is compared to each cluster already in the new list to search for "overlap". Two clusters are considered to overlap if any strip in the old cluster lies within the distance parameter (22.5 cm in the Calibration Detector) of any strip in the new cluster, i.e., the closest strips between the clusters are separated by less than the distance parameter. If the old cluster overlaps with a new cluster, the old cluster is merged into the new one; otherwise, the old cluster is added as a separate cluster to the new list. Once the loop over the old clusters completes, it is started again unless no clusters were merged, at which point the clustering is complete.

The main difficulty with using the cluster merging algorithm arises because of the small size of the Calibration Detector. Digits caused by cross-talk can be close enough to track digits in adjacent planes that the cross-talk digits are clustered with those track digits in adjacent planes, but not with the track digits in the same plane. This effect is particularly prevalent in steep tracks.

Figure B.5 shows a comparison of the cluster merging algorithm with the band clustering algorithm from Section 5.2.2 for a steep cosmic muon. The cluster merging algorithm has failed to identify the muon track. Moreover, the cross-talk digits have been associated with track digits in a manner that could give a misleading impression of the track. In contrast, the band clustering algorithm successfully identifies the muon track.

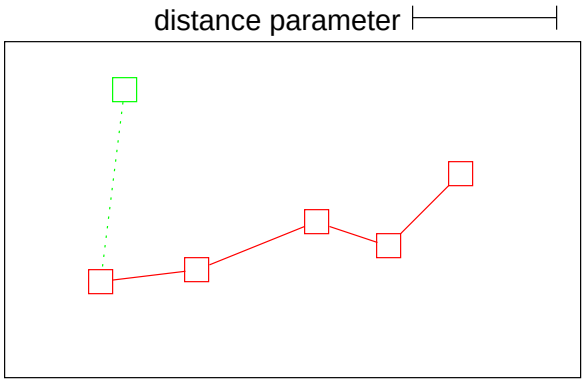

Figure B.1: Example outcome from cluster merging. The boxes represent strips, and the different colours represent different clusters. Strips in the same cluster are separated by a distance less than the distance parameter. The solid lines between strips indicate the connections used to form the cluster. The dotted line indicates a failed connection due to the strips being too far away from each other.

```
Form cluster for each strip
Add all clusters to old list

LOOP {
    Remove first cluster from old list
    Add first cluster to new list

    LOOP over remaining clusters in old list {
        Remove cluster from old list

        LOOP over clusters in new list {
            IF old-list cluster overlaps new-list cluster {
                Merge old-list cluster into new-list cluster
                BREAK from new list loop
            }  //End IF
        }  // End LOOP over new list

        IF old-list cluster not merged
        THEN add old-list cluster to new list
    }  // End LOOP over old list

    Rename new list as old list
} until no clusters merged

Old list is the final list of clusters
```

Figure B.2: Pseudocode for the cluster merging algorithm.

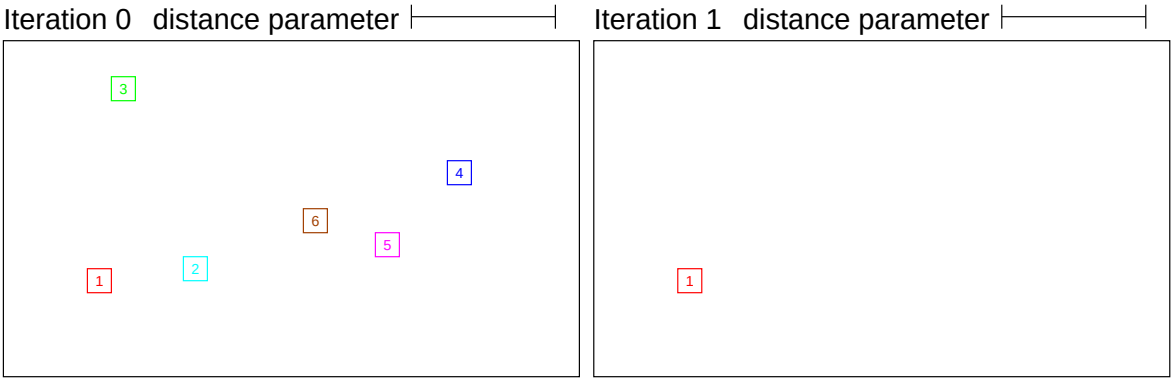

(a) Initial state: each strip is in its own cluster.

(b) 1st iteration: red cluster is added. There are no other clusters with which to find overlap.

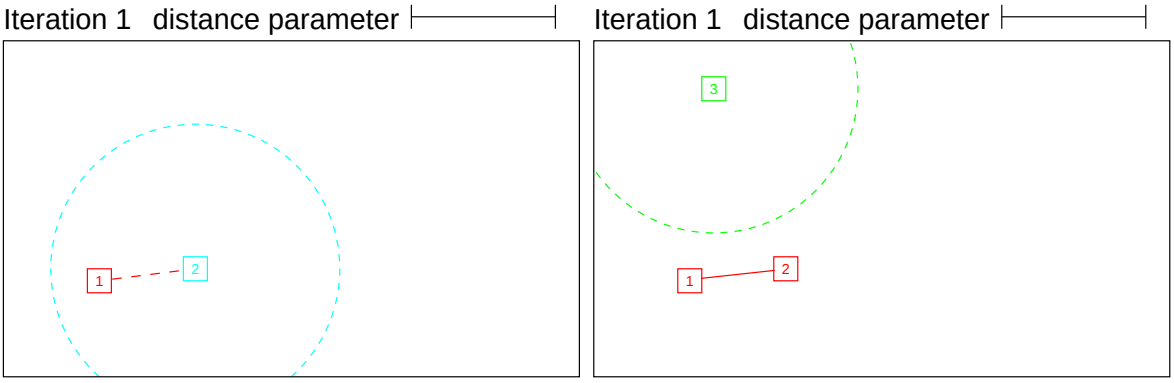

(c) 1st iteration: cyan cluster is added. Strips 1 and 2 overlap, so the cyan cluster merges with the red.

(d) 1st iteration: green cluster is added. No overlap is found, so the green cluster remains separate.

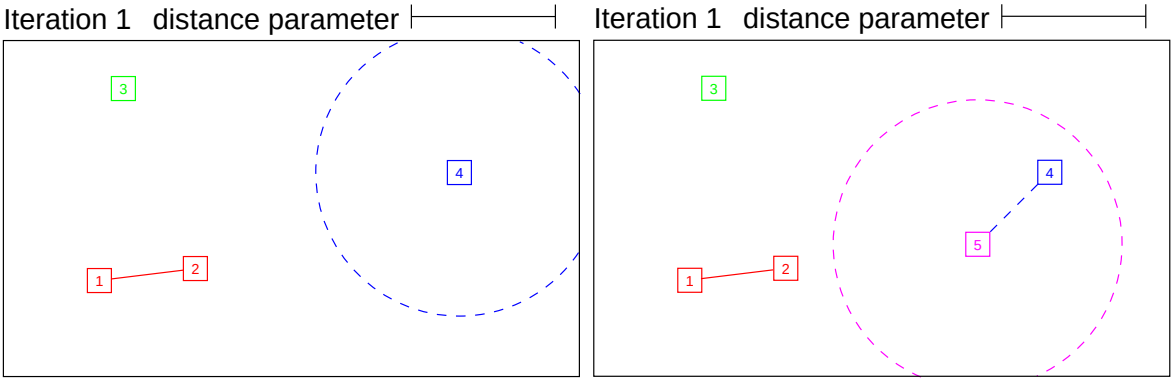

(e) 1st iteration: blue cluster is added. No overlap is found, so the blue cluster remains separate.

(f) 1st iteration: magenta cluster is added. Strips 4 and 5 overlap, so the magenta cluster merges with the blue.

Figure B.3: Detailed example of cluster merging. The boxes indicate strips, and the numbers indicate the order in which the strips are processed. The different colours represent different clusters. The dashed circles indicate the area used to search for overlap. The solid lines indicate the existing connections, and the dashed lines indicate new overlaps found.

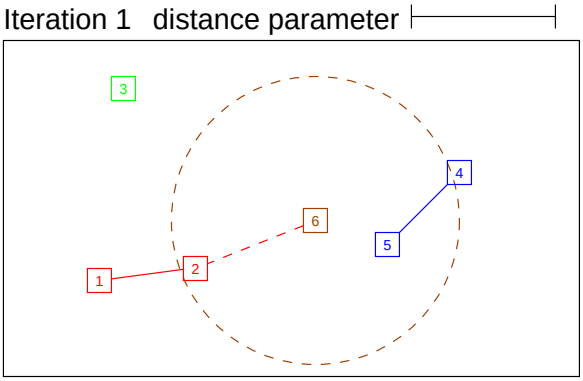

(a) 1st iteration: brown cluster is added. Strips 6 and 2 overlap, so brown merges with red. This completes the first iteration. Several clusters merged, so another iteration is needed.

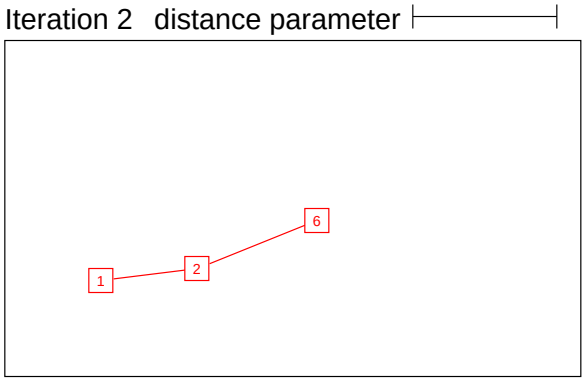

(b) 2nd iteration: red cluster is added. There are no other clusters with which to find overlap.

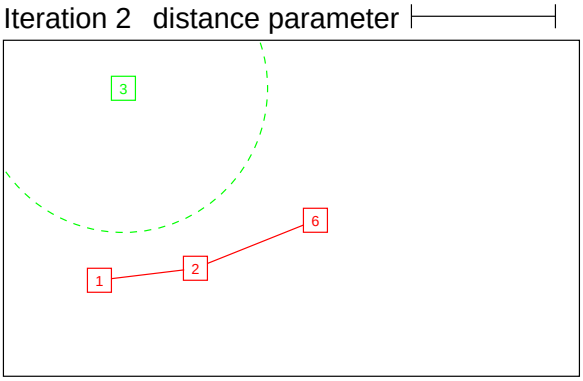

(c) 2nd iteration: green cluster is added. No overlap, so green remains separate.

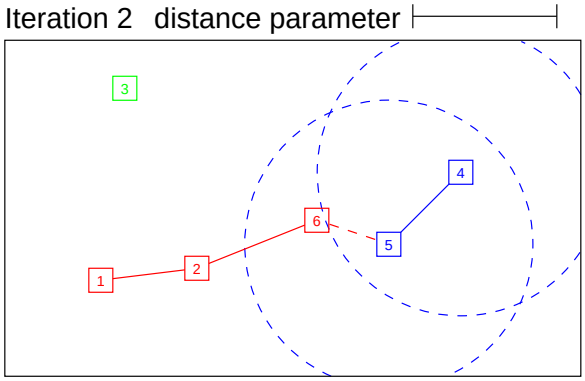

(d) 2nd iteration: blue cluster is added. Strips 5 and 6 overlap, so blue merges with red. This completes the second iteration. Two clusters merged, so another iteration is needed.

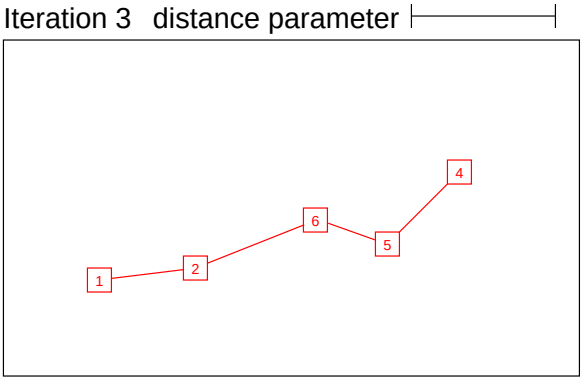

(e) 3rd iteration: red cluster is added. There are no other clusters with which to find overlap.

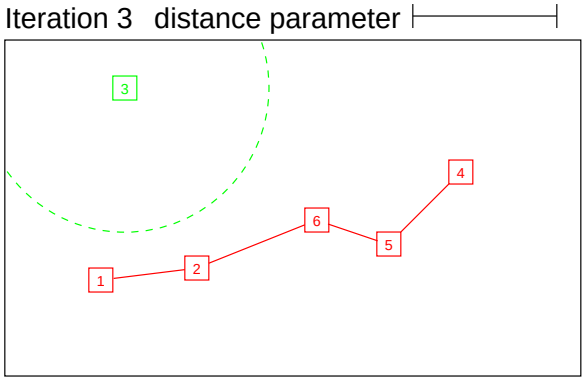

(f) 3rd iteration: green cluster is added. No overlap, so green remains separate. This completes the third iteration. No clusters merged, so the algorithm is complete.

Figure B.4: Detailed example of cluster merging (continued from Figure B.3).

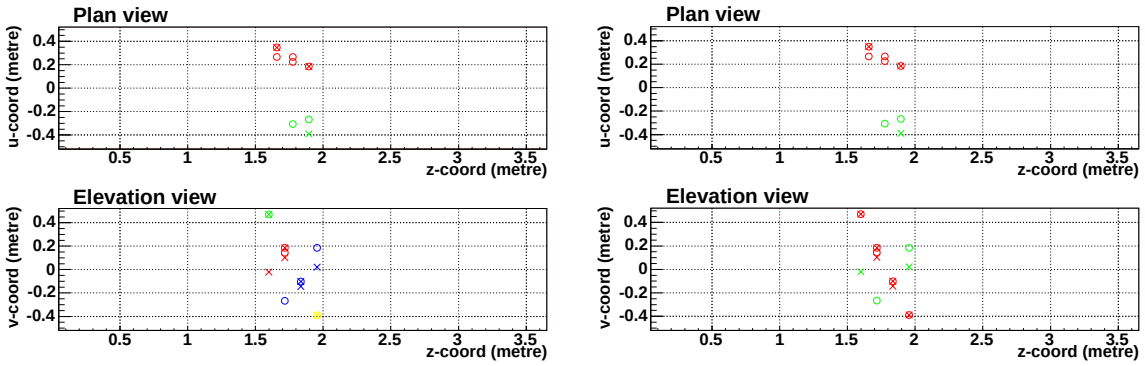

(a) Cluster merging algorithm. Each cluster is shown by a different colour. This algorithm has failed to group the digits in the main track in a single cluster. Moreover, some cross-talk digits have been associated with track digits in adjacent planes, giving a false impression of how the track may look.

(b) Band clustering algorithm. The digits of the main cluster are shown in red, with all remaining digits in green. This algorithm has identified the digits in the main track with a few extra digits.

Figure B.5: Examples of clustering a CalDet event using different algorithms. The event shown is a steep cosmic muon entering through the top of the detector and exiting out the bottom. The layout of each diagram is as in Figure 5.3. The actual muon track is evident from the double-ended strips.

References

[1] F. Reines and C. L. Cowan, Jr., Detection of the free neutrino, Phys. Rev. **92**, 830 (1953); C. L. Cowan, Jr., F. Reines, F. B. Harrison, H. W. Kruse, and A. D. McGuire, Detection of the free neutrino: a confirmation, Science **124**, 103 (1956).

[2] S. L. Glashow, Partial symmetries of weak interactions, Nucl. Phys. **22**, 579 (1961); A. Salam, Weak and electromagnetic interactions, in *Elementary Particle Theory*, Proceedings Of The 8th Nobel Symposium, edited by N. Svartholm, pages 367–377, Stockholm, Sweden (1968); S. Weinberg, A model of leptons, Phys. Rev. Lett. **19**, 1264 (1967).

[3] B. Pontecorvo, Mesonium and antimesonium, Sov. Phys. JETP **6**, 429 (1957); B. Pontecorvo, Inverse beta processes and nonconservation of lepton charge, Sov. Phys. JETP **7**, 172 (1958).

[4] MINOS Collaboration, The MINOS Detectors Technical Design Report, NuMI-L-337 (1998).

[5] Super-Kamiokande Collaboration: Y. Ashie et al., Evidence for an oscillatory signature in atmospheric neutrino oscillation, Phys. Rev. Lett. **93**, 101801 (2004).

[6] G. Danby et al., Observation of high-energy neutrino reactions and the existence of two kinds of neutrinos, Phys. Rev. Lett. **9**, 36 (1962).

[7] M. L. Perl et al., Evidence for anomalous lepton production in e^+-e^- annihilation, Phys. Rev. Lett. **35**, 1489 (1975).

[8] DONUT Collaboration: K. Kodama et al., Observation of tau neutrino interactions, Phys. Lett. **B504**, 218 (2001).

[9] Particle Data Group Collaboration: S. Eidelman et al., Review of particle physics, Phys. Lett. **B592**, 1 (2004).

[10] M. Goldhaber, L. Grodzins, and A. W. Sunyar, Helicity of neutrinos, Phys. Rev. **109**, 1015 (1958).

[11] C. Kraus et al., Latest results from the Mainz Neutrino Mass Experiment, Nucl. Phys. **A721**, 533 (2003).

[12] K. Assamagan et al., Upper limit of the muon-neutrino mass and charged pion mass from momentum analysis of a surface muon beam, Phys. Rev. **D53**, 6065 (1996).

[13] J. M. Roney, Review of the tau neutrino mass, Nucl. Phys. Proc. Suppl. **91**, 287 (2001).

[14] R. N. Mohapatra and G. Senjanovic, Neutrino mass and spontaneous parity nonconservation, Phys. Rev. Lett. **44**, 912 (1980).

[15] N. Cabibbo, Unitary symmetry and leptonic decays, Phys. Rev. Lett. **10**, 531 (1963); M. Kobayashi and T. Maskawa, CP violation in the renormalizable theory of weak interaction, Prog. Theor. Phys. **49**, 652 (1973).

[16] H. Fritzsch and Z.-Z. Xing, On the parametrization of flavor mixing in the standard model, Phys. Rev. **D57**, 594 (1998); H. Fritzsch and Z.-Z. Xing, How to describe neutrino mixing and CP violation, Phys. Lett. **B517**, 363 (2001).

[17] L. Wolfenstein, Neutrino oscillations in matter, Phys. Rev. **D17**, 2369 (1978); S. P. Mikheev and A. Y. Smirnov, Resonance enhancement of oscillations in matter and solar neutrino spectroscopy, Sov. J. Nucl. Phys. **42**, 913 (1985).

[18] R. Davis, Jr., D. S. Harmer, and K. C. Hoffman, Search for neutrinos from the sun, Phys. Rev. Lett. **20**, 1205 (1968).

[19] Super-Kamiokande Collaboration: Y. Fukuda et al., Evidence for oscillation of atmospheric neutrinos, Phys. Rev. Lett. **81**, 1562 (1998).

[20] LSND Collaboration: A. Aguilar et al., Evidence for neutrino oscillations from the observation of $\overline{\nu}_e$ appearance in a $\overline{\nu}_\mu$ beam, Phys. Rev. **D64**, 112007 (2001).

[21] J. N. Bahcall, *Neutrino Astrophysics* (Cambridge University Press, Cambridge, 1989).

[22] J. N. Bahcall, M. H. Pinsonneault, and S. Basu, Solar models: Current epoch and time dependences, neutrinos, and helioseismological properties, Astrophys. J. **555**, 990 (2001).

[23] S. Basu et al., Solar internal sound speed as inferred from combined BiSON and LOWL oscillation frequencies, Mon. Not. R. Astron. Soc. **292**, 243 (1997).

[24] B. T. Cleveland et al., Measurement of the solar electron neutrino flux with the Homestake chlorine detector, Astrophys. J. **496**, 505 (1998).

[25] SAGE Collaboration: J. N. Abdurashitov et al., Measurement of the solar neutrino capture rate with gallium metal, Phys. Rev. **C60**, 055801 (1999).

[26] GALLEX Collaboration: P. Anselmann et al., Solar neutrinos observed by GALLEX at Gran Sasso., Phys. Lett. **B285**, 376 (1992).

[27] GNO Collaboration: M. Altmann et al., GNO solar neutrino observations: Results for GNO I, Phys. Lett. **B490**, 16 (2000).

[28] Kamiokande-II Collaboration: K. S. Hirata et al., Real time, directional measurement of B-8 solar neutrinos in the Kamiokande-II detector, Phys. Rev. **D44**, 2241 (1991).

[29] Y. Fukuda et al., The Super-Kamiokande detector, Nucl. Instrum. Meth. **A501**, 418 (2003).

[30] E. Bellotti, First results from GNO, Nucl. Phys. Proc. Suppl. **91**, 44 (2001).

[31] SAGE Collaboration: V. N. Gavrin, Solar neutrino results from SAGE, Nucl. Phys. Proc. Suppl. **91**, 36 (2001).

[32] Kamiokande Collaboration: Y. Fukuda et al., Solar neutrino data covering solar cycle 22, Phys. Rev. Lett. **77**, 1683 (1996).

[33] Y. Suzuki, Solar Neutrino Results from Super-Kamiokande, Nucl. Phys. Proc. Suppl. **91**, 29 (2001).

[34] N. Hata and P. Langacker, Solutions to the solar neutrino anomaly, Phys. Rev. **D56**, 6107 (1997).

[35] SNO Collaboration: J. Boger et al., The Sudbury Neutrino Observatory, Nucl. Instrum. Meth. **A449**, 172 (2000).

[36] SNO Collaboration: Q. R. Ahmad et al., Direct evidence for neutrino flavor transformation from neutral-current interactions in the Sudbury Neutrino Observatory, Phys. Rev. Lett. **89**, 011301 (2002).

[37] SNO Collaboration: S. N. Ahmed et al., Measurement of the total active ^{8}B solar neutrino flux at the Sudbury Neutrino Observatory with enhanced neutral current sensitivity, nucl-ex/0309004 (unpublished).

[38] J. N. Bahcall, M. C. Gonzalez-Garcia, and C. Pena-Garay, Before and after: How has the SNO neutral current measurement changed things?, JHEP **07**, 054 (2002).

[39] KamLAND Collaboration: A. Piepke, KamLAND: A reactor neutrino experiment testing the solar neutrino anomaly, Nucl. Phys. Proc. Suppl. **91**, 99 (2001).

[40] KamLAND Collaboration: T. Araki et al., Measurement of neutrino oscillation with KamLAND: Evidence of spectral distortion, hep-ex/0406035 (to appear).

[41] J. N. Bahcall, M. C. Gonzalez-Garcia, and C. Pena-Garay, Solar neutrinos before and after Neutrino 2004, JHEP **08**, 016 (2004).

[42] T. K. Gaisser and M. Honda, Flux of atmospheric neutrinos, Ann. Rev. Nucl. Part. Sci. **52**, 153 (2002).

[43] A. De Santo, An experimentalist's view of neutrino oscillations, Int. J. Mod. Phys. **A16**, 4085 (2001).

[44] T. J. Haines et al., Calculation of atmospheric neutrino induced backgrounds in a nucleon decay search, Phys. Rev. Lett. **57**, 1986 (1986).

[45] R. Becker-Szendy et al., Electron- and muon-neutrino content of the atmospheric flux, Phys. Rev. **D46**, 3720 (1992).

[46] Kamiokande-II Collaboration: K. S. Hirata et al., Experimental study of the atmospheric neutrino flux, Phys. Lett. **B205**, 416 (1988); Kamiokande-II Collaboration: K. S. Hirata et al., Observation of a small atmospheric ν_μ/ν_e ratio in Kamiokande, Phys. Lett. **B280**, 146 (1992).

[47] Kamiokande Collaboration: Y. Fukuda et al., Atmospheric ν_μ/ν_e ratio in the multi-GeV energy range, Phys. Lett. **B335**, 237 (1994).

[48] The NUSEX Collaboration: M. Aglietta et al., Experimental study of atmospheric neutrino flux in the NUSEX experiment, Europhys. Lett. **8**, 611 (1989).

[49] Fréjus Collaboration: C. Berger et al., Study of atmospheric neutrino interactions with the Fréjus detector, Phys. Lett. **B227**, 489 (1989).

[50] Fréjus Collaboration: C. Berger et al., A Study of atmospheric neutrino oscillations in the FREJUS experiment, Phys. Lett. **B245**, 305 (1990).

[51] Fréjus Collaboration: K. Daum, Determination of the atmospheric neutrino spectra with the Fréjus detector, Z. Phys. **C66**, 417 (1995).

[52] W. W. M. Allison et al., Measurement of the atmospheric neutrino flavour composition in Soudan-2, Phys. Lett. **B391**, 491 (1997); Soudan-2 Collaboration: W. W. M. Allison et al., The atmospheric neutrino flavor ratio from a 3.9 fiducial kiloton-year exposure of Soudan 2, Phys. Lett. **B449**, 137 (1999).

[53] Soudan 2 Collaboration: M. Sanchez et al., Measurement of the L/E distributions of atmospheric ν in Soudan 2, Phys. Rev. **D68**, 113004 (2003).

[54] Super-Kamiokande Collaboration: T. Toshito, Super-Kamiokande atmospheric neutrino results, in *XXXVIth Rencontres de Moriond on Electroweak Interactions and Unified Theories*, Les Arcs, Savoie, France (2001).

[55] W. A. Mann, Atmospheric neutrinos and the oscillations bonanza, Int. J. Mod. Phys. **A15S1**, 229 (2000).

[56] M. M. Boliev et al., Observation of upward through-going muons with the Baksan detector: An update, Nucl. Phys. Proc. Suppl. **70**, 371 (1999).

[57] MACRO Collaboration: M. Ambrosio et al., Atmospheric neutrino oscillations from upward throughgoing muon multiple scattering in MACRO, Phys. Lett. **B566**, 35 (2003).

[58] Super-Kamiokande Collaboration: Y. Hayato, Status of the Super-Kamiokande, the K2K experiment and the J-PARC ν project, Talk at the International Europhysics Conference on High Energy Physics at Aachen, Germany (2003).

[59] Super-Kamiokande Collaboration: C. Yanagisawa, Recent results from Super-Kamiokande, in *Frontiers in Contemporary Physics 2001*, Vanderbilt University, Nashville, Tennessee, USA (2001).

[60] Super-Kamiokande Collaboration: H. Sobel, Atmospheric neutrinos in Super-Kamiokande, Nucl. Phys. Proc. Suppl. **91**, 127 (2001).

[61] K2K Collaboration: T. Nakaya, New K2K results, Talk at the XXIst International Conference on Neutrino Physics and Astrophysics (Neutrino 2004) at Paris, France (2004).

[62] F. Dydak et al., A search for ν_μ oscillations in the Δm^2 range 0.3–90 eV^2, Phys. Lett. **B134**, 281 (1984).

[63] L. Borodovsky et al., Search for muon-neutrino oscillations $\nu_\mu \to \nu_e$ $(\overline{\nu}_\mu \to \overline{\nu}_e)$ in a wide band neutrino beam, Phys. Rev. Lett. **68**, 274 (1992).

[64] CHORUS Collaboration: E. Eskut et al., New results from a search for $\nu_\mu \to \nu_\tau$ and $\nu_e \to \nu_\tau$ oscillation, Phys. Lett. **B497**, 8 (2001).

[65] NOMAD Collaboration: P. Astier et al., Final NOMAD results on $\nu_\mu \to \nu_\tau$ and $\nu_e \to \nu_\tau$ oscillations including a new search for ν_τ appearance using hadronic τ decays, Nucl. Phys. **B611**, 3 (2001).

[66] KARMEN Collaboration: B. Armbruster et al., Upper limits for neutrino oscillations $\overline{\nu}_\mu \to \overline{\nu}_e$ from muon decay at rest, Phys. Rev. **D65**, 112001 (2002).

[67] Y. Declais et al., Search for neutrino oscillations at 15, 40 and 95 meters from a nuclear power reactor at Bugey, Nucl. Phys. **B434**, 503 (1995).

[68] MiniBooNE Collaboration: R. Tayloe, The MiniBooNE experiment: Status and plans, Nucl. Phys. Proc. Suppl. **118**, 157 (2003).

[69] H. Murayama, updated version of a figure contained in [9], available at http://hitoshi.berkeley.edu/neutrino/.

[70] M. Apollonio et al., Search for neutrino oscillations on a long base-line at the CHOOZ nuclear power station, Eur. Phys. J. **C27**, 331 (2003).

[71] M. C. Gonzalez-Garcia, M. Maltoni, C. Pena-Garay, and J. W. F. Valle, Global three-neutrino oscillation analysis of neutrino data, Phys. Rev. **D63**, 033005 (2001).

[72] J. Hylen et al., NuMI Technical Design Handbook, Internal NuMI report (2003).

[73] J. Hylen et al., Conceptual design for the technical components of the neutrino beam for the Main Injector (NuMI), NuMI-B-285 (1997).

[74] M. Messier et al., Neutrino fluxes, hadron production, and the hadronic hose, NuMI-B-700 (2000).

[75] B. C. Choudhary, Extruded polystyrene scintillator for MINOS, NuMI-L-676 (2000).

[76] B. Anderson, A. Anjomshoaa, P. Dervan, J. A. Lauber, and J. Thomas, Ultra bright LED light injection calibration system for MINOS, Nucl. Instrum. Meth. **A423**, 320 (1999).

[77] B. C. Choudhary and L. Mualem, Technical specifications for the procurement of wavelength shifting fibre for the MINOS detector, NuMI-L-589 (2000).

[78] P. Harris, Checkerboard MUXing: How to minimize PMT crosstalk problems, NuMI-L-535 (1999).

[79] G. Pearce, System Overview, talk given at the Third MINOS Data Acquisition and Timing Review, February 2001.

[80] N. Felt et al., MINOS Far Detector Electronics—User's Manual, Internal NuMI report (2001).

[81] G. Barr and N. Tagg, User's guide to the Far Detector timing system, Internal NuMI report (2003).

[82] MINOS Collaboration, The MINOS Detectors Design Parameter Book, Internal NuMI report (2001).

[83] G. Drake, J. Dawson, and C. Nelson, Overview of the front end electronics for the MINOS Near Detector, NuMI-L-628 (1999).

[84] D. A. Petyt, Physics potential of the three Ph2 beam designs, NuMI-L-612 (2000).

[85] J. H. Cobb, The algebra of the T-Test, NuMI-L-272 (1997).

[86] D. A. Petyt, Low Δm^2 sensitivity of the T-test, NuMI-S-481 (1999).

[87] P. Ballester, Hough transform for robust regression and automated detection, Astron. Astrophys. **286**, 1011 (1994).

[88] D. A. Petyt, *A study of parameter measurements in a long-baseline neutrino oscillation experiment*, DPhil thesis, University of Oxford, 1998.

[89] Super-Kamiokande Collaboration: M. Ishitsuka, Direct oscillatory evidence from L/E analysis in Super-Kamiokande, Talk at the 5th Workshop on "Neutrino Oscillations and their Origin" (NOON2004) at Tokyo, Japan (2004).

[90] D. A. Petyt, $\tau \to \pi + X$ analysis in MINOS, NuMI-L-258 (1997).

[91] M. Diwan, M. Messier, B. Viren, and L. Wai, A study of $\nu_\mu \to \nu_e$ sensitivity in MINOS, NuMI-L-714 (2001).

[92] CHOOZ Collaboration: M. Apollonio et al., Limits on neutrino oscillations from the CHOOZ experiment, Phys. Lett. **B466**, 415 (1999).

[93] P. Harris, MINOS calibration, Internal NuMI report (2003).

[94] P. Adamson et al., The MINOS light injection calibration system, Nucl. Instrum. Meth. **A492**, 325 (2002).

[95] R. Lee and S. Seun, Calibration of MINOS Detectors Using Cosmic Ray Muons, NuMI-L-694 (2000).

[96] MINOS Collaboration, Proposal for PS test beam time for the MINOS calibration module, NuMI-L-681 (2000).

[97] H. Gallagher, The NEUGEN neutrino event generator, Nucl. Phys. Proc. Suppl. **112**, 188 (2002).

[98] G. D. Barr, *The separation of signals and background in a nucleon decay experiment*, DPhil thesis, University of Oxford, 1987.

[99] M. A. Barker, *Hadronic response of the MINOS detectors*, DPhil thesis, University of Oxford, 2003.

[100] MINOS Collaboration: P. S. Miyagawa, Present status of the MINOS calibration detector, Prog. Part. Nucl. Phys. **48**, 111 (2002).

[101] K. Bätzner et al., Secondary beams for tests in the PS East experimental area, PS/PA/Note 93-21 (1993).

[102] R. Hatcher, A comparison of the `gminos` simulation to prototype module data, NuMI-L-478 (1999).

[103] The MINOS Off-line Software User's Manual Release R1.9 (2004), see also http://www-numi.fnal.gov/offline_software/srt_public_context/WebDocs/WebDocs.html.

[104] R. Brun, F. Rademakers, S. Panacek, I. Antcheva, and D. Buskulic, The ROOT Users Guide, v4.08 (2004), see also http://root.cern.ch.

[105] B. J. Rebel and S. L. Mufson, A demultiplexing algorithm for the MINOS Far Detector, NuMI-L-725 (2001).

[106] B. J. Rebel and S. L. Mufson, A demultiplexing algorithm for cosmic rays in the MINOS Far Detector, NuMI-L-834 (2002).

[107] R. Hatcher, private communication.

[108] P. Border et al., A large liquid scintillator detector for a long baseline neutrino oscillation experiment, Nucl. Instrum. Meth. **A463**, 194 (2001).

[109] K. Ruddick, private communication.

[110] Kuraray Co. Ltd., Tokyo, Japan.

[111] K. Lang, Technical specifications for R5900-00-M16 PMTs for the MINOS detectors, NuMI-L-664 (2000).

[112] D. A. Petyt, private communication.

[113] A. J. G. Weber, private communication.

[114] R. Brun, F. Rademakers, S. Panacek, I. Antcheva, and D. Buskulic, The ROOT Users Guide, v4.08 (2004), see also http://root.cern.ch/root/html/TMinuit.html; F. James, MINUIT—Function Minimization and Error Analysis, version 94.1, CERN Program Library entry D506 (1998).